

Synthesis of Metal Oxide Inverse Opals and their Applications in Optical Sensing

Dissertation

zur Erlangung des Grades
Doktor der Naturwissenschaften

(Dr. rer. nat.)

der Fakultät für Naturwissenschaften der Universität Paderborn

vorgelegt von
Xuyang Zhang

Paderborn, Oktober 2019

Die vorliegende Arbeit wurde in der Zeit von Dezember 2015 bis September 2019 am Institut für Anorganische und Analytische Chemie der Universität Paderborn in der Arbeitsgruppe von Dr. Thorsten Wagner angefertigt.

Gutachter: Dr. Thorsten Wagner

Prof. Dr. Michael Tiemann

Tag der Disputation: 14.11.2019

VERSICHERUNG

Hiermit versichere ich, die vorliegende Arbeit eigenständig und ausschließlich unter Verwendung der angegebenen Hilfsmittel und Quellen durchgeführt zu haben. Die Arbeit ist zuvor keiner Prüfungsbehörde in gleicher oder ähnlicher Form vorgelegt worden.

Paderborn, den 10.10.2019

“Ever tried. Ever failed. No matter. Try again. Fail again. Fail better.”

Samuel Beckett

Content

1. Motivation.....	1
2. Introduction.....	3
2.1 Photonic crystals.....	3
2.2 Synthesis of photonic crystals	6
2.2.1 Synthesis of polymer opal structures	6
2.2.2 Synthesis of metal oxide inverse opal structures	9
2.3 Optical sensing based on metal oxide inverse opals.....	11
2.3.1 Fluids sensing mechanism.....	11
2.3.2 Water temperature sensing mechanism.....	12
2.3.3 H ₂ sensing mechanism	13
3. Experiment.....	17
3.1 Synthesis of polymer opal structures.....	17
3.1.1 Synthesis of PMMA particles	17
3.1.2 Synthesis of PMMA opals.....	18
3.2 Synthesis of metal oxide inverse opal structures.....	18
3.2.1 Pure metal nitrates as precursors	18
3.2.2 Modified metal nitrate as precursors	19
3.2.2.1 Organic chelating with citric acid.....	19
3.2.2.2 Sol-gel polymerization of TEOS	19
3.2.2.3 Polyacrylamide gelation	20
3.2.3 Synthesis of SnO ₂ inverse opals.....	20
3.2.4 Synthesis of TiO ₂ inverse opals	20
3.2.5 Synthesis of WO ₃ inverse opals	21
3.3 Characterization Methods.....	21
3.3.1 Dynamic Light Scattering	21
3.3.2 Powder X-ray Diffraction.....	21

3.3.3	Fourier-Transform Infrared Spectroscopy.....	21
3.3.4	Scanning Electron Microscopy	22
3.3.5	Thermogravimetric Analysis.....	22
3.3.6	Differential Scanning Calorimetry	22
3.3.7	Fluids Sensing Measurements	23
3.3.8	Water Temperature Sensing Measurements.....	23
3.3.9	H ₂ Sensing Measurements.....	23
4.	Results and Discussion	25
4.1	Polymer opal structures	25
4.1.1	PMMA particles	25
4.1.2	PMMA opals on glass substrates	27
4.1.3	PMMA opals on nitrocellulose substrates.....	30
4.2	Metal oxide inverse opals	32
4.2.1	Pure metal nitrate as precursors.....	32
4.2.1.1	Ga ₂ O ₃	32
4.2.1.2	Cr ₂ O ₃	37
4.2.1.3	Fe ₂ O ₃	37
4.2.1.4	In ₂ O ₃	38
4.2.1.5	CeO ₂ , CuO and ZnO	39
4.2.1.6	Thermal behavior of PMMA particles and respective metal nitrates	39
4.2.2	Modified metal nitrate as precursors	46
4.2.2.1	Organic chelating method.....	46
4.2.2.2	Polymerization of TEOS	50
4.2.2.3	Polyacrylamide gelation method	51
4.2.3	Metal oxide nanoparticles as precursors	52
4.2.3.1	SnO ₂	52
4.2.3.2	TiO ₂	53
4.3	WO ₃ inverse opals and their optical sensing properties	55

4.3.1	Optical properties of WO ₃ inverse opals.....	55
4.3.2	Crystallite structure of WO ₃ inverse opals.....	58
4.3.3	Fluids sensing based on WO ₃ inverse opals.....	58
4.3.4	Water temperature sensing based on WO ₃ inverse opals.....	62
4.3.5	H ₂ sensing based on WO ₃ inverse opals.....	66
5.	Summary.....	76
6.	Zusammenfassung.....	79
7.	Reference.....	82
8.	Appendix.....	90

1. Motivation

Metal oxide inverse opals that exhibit three-dimensionally ordered macroporous structures are promising for applications in catalysis, sensor technology, energy storage, etc. The conventional synthesis route of inverse opals is based on structure replication following a colloidal crystal templating process. The resulting structures are solids with periodically ordered spherical void spaces which can be considered as photonic crystals. Due to Bragg diffraction, light within certain wavelength ranges can pass through photonic crystals, while the light in other ranges is reflected (photonic band gaps), thus making inverse opals colored and opalescent.

In this present work, the successful utilization of colloidal crystal templating method to fabricate various metal oxide inverse opals (cerium(IV) oxide (CeO_2), chromium(III) oxide (Cr_2O_3), copper(II) oxide (CuO), iron(III) oxide (Fe_2O_3), gallium(III) oxide (Ga_2O_3), indium(III) oxide (In_2O_3), tin(IV) oxide (SnO_2), titanium dioxide (TiO_2), tungsten trioxide (WO_3), zinc oxide (ZnO)) is reported. To fabricate inverse opals of CeO_2 , CuO , Cr_2O_3 , Fe_2O_3 , Ga_2O_3 , In_2O_3 , and ZnO , respective metal nitrates were adopted as precursors to compare the effects of different precursor/template interactions on the degree of the structural order of inverse opals. The thermal behaviors of the precursor and template materials, the effects of organic chelating, as well as the role of fixing agent (e.g., tetraethyl orthosilicate (TEOS) and polyacrylamide) in precursor solidification process are studied in detail. In the synthesis of SnO_2 , TiO_2 and WO_3 inverse opals, different solidification strategies (precursor composition) were employed to reduce structural shrinkage and produce highly ordered macroporous structures.

Besides the fabrication and the characterization of metal oxides inverse opals, another part of this work focus on the optical sensing based on WO_3 inverse opals:

- (i) WO_3 inverse opals were employed to detect fluids with different refractive indices. The sensitivities of WO_3 inverse opals with different pore sizes were quantified.
- (ii) A temperature responsive and adsorbable block copolymer was infiltrated into WO_3 inverse opals. By washing with different temperature water and measuring the corresponding change in reflection spectra, the possibility of optical detection of water temperature was investigated.

(iii) A series of WO_3 inverse opals exhibiting different photonic band gap positions were used as optical hydrogen (H_2) sensor. The optical responses (H_2 induced reflection peak shift) of different WO_3 inverse opals were examined to reconstruct the strong refractive index dispersion of WO_3 after H_2 exposure. This study aimed to find the physical origin of the refractive index change during gas sensing. Then, by gaining the insights into the physical sensing mechanisms, the general rules of the design of optical gas sensor based on metal oxide photonic crystals were concluded.

2. Introduction

2.1 Photonic crystals

Photonic crystals [1, 2] are a class of optical materials in which materials with different refractive indices are arranged in a periodic lattice. Because of the periodicity, photonic crystals are often considered to be the optical analogue of semiconductors. In semiconductor crystals, electrons are scattered at the periodic electrical potential and the backscattered electron waves interfere destructively for certain energies, give rise to the electronic band gaps, which are forbidden energy bands for electrons. Photonic crystals, on the other hand, are dielectric materials with a periodic modulation of the refractive index (i.e. dielectric constant). Within the photonic crystal photons are scattered at the periodic interfaces several times coherently, which leads to a photonic band gap structure. The periodic variation of the refractive index is possible in one, two or three dimensions (Figure 2.1 [3]).

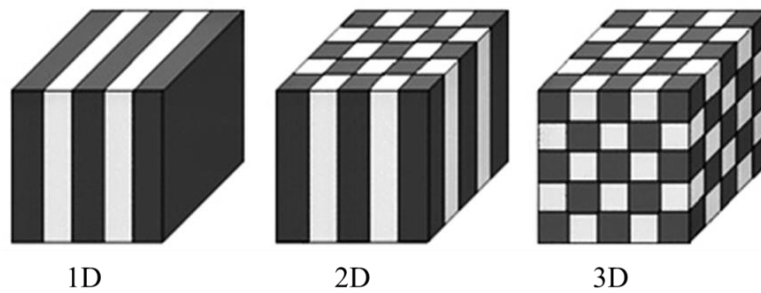


Figure 2.1: Schema of one-dimensional (1D), two-dimensional (2D) and three-dimensional (3D) photonic crystals. The black and white colors represent materials with different refractive indices.

Modified from reference [3]

One-dimensional photonic crystals, which have an alternating stack of two different dielectric materials, have been widely used as optical filters and dielectric mirrors [3]. These photonic crystals can reflect light at each boundary of the dielectric layers and localize photons in the structural defects [4]. Two-dimensional photonic crystals are formed by fabricating a structure that has periodicity in two directions. These crystals typically consist of air-filled cylindrical cavities and a highly refractive material for the interstices. Most interesting are the three-dimensional photonic crystals. Their structure is periodically organized along three different directions. The propagation of light within the photonic structure is therefore influenced in all three spatial directions.

In nature there are various photonic structures with iridescent colors. One example is the butterfly (Figure 2.2 left), whose wings consist of a structured scale layer with grooves forming photonic crystal structures. The gem stone opal (Figure 2.2 right), which consists of a regular arrangement of colloidal silica particles, is another example of three-dimensional photonic crystal. Its strong opalescence is the result of photonic band gap effect.



Figure 2.2: iridescent blue color of a butterfly (left, image from animalshine.com) and strong opalescence of a gem stone opal (right, image from minerals.net)

Inspired by the natural opals, artificial opals were fabricated using different colloidal particles (e.g. silica [5-7] or polymer particles [8-11]). The assembly of these particles leads to the formation of a crystal lattice with two repetitive zones with different refractive indexes: the space filled by the colloidal particles and the void filled by air.

One of the simplest ways to probe the structural and optical quality of colloidal photonic crystals is by observation of their optical reflectance spectra (i.e. structural color). As depicted in Figure 2.3, the colloidal opal crystal is modelled as multilayer of two media with different refractive indices. The opal is formed with the $\{111\}$ lattice planes parallel to the substrate surface. The combination of Bragg diffraction law and refraction Snell law can be derived to describe its optical reflectance (photonic band gap).

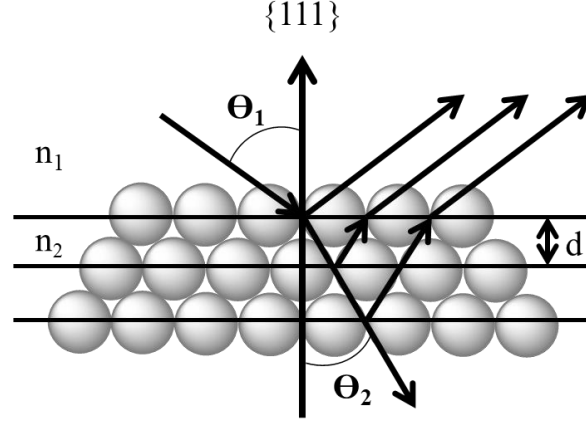


Figure 2.3: The diffraction of light from closed-packed {111} crystal planes in a colloidal photonic crystal

When the light enters the colloidal crystal, it is partially reflected at each boundary of the dielectric layers. The constructive interference can be described by Bragg diffraction law

$$\lambda = 2n_{eff}d\cos\theta_1 \quad (2.1)$$

Where λ is the Bragg peak position of the colloidal crystal, d is the interplanar spacing between two sphere centers (It has a value of $d = \sqrt{\frac{2}{3}} \times D$ and D is the sphere diameter) and n_{eff} is the effective refractive index.

The corresponding refraction Snell law is defined as

$$n_1\sin\theta_1 = n_2\sin\theta_2 \quad (2.2)$$

And the master equation to describe the optical reflectance (photonic band gap) can be written as

$$\lambda = \sqrt{\frac{8}{3}} \cdot D \cdot \sqrt{n_{eff}^2 - \sin^2\theta_1} \quad (2.3)$$

According to equation 2.3, optical reflectance responds to changes in sphere diameter, effective refractive index of the photonic crystal and light incident angle. If one or more of these parameters change, the corresponding photonic band gap shifts.

Photonic band gap is also influenced by the refractive index contrast, the bigger the refractive index contrast, the wider this photonic band gap becomes. To get a higher refractive index contrast, colloidal opal structure can be inverted: the void space can be filled by a material

with a high refractive index (e.g. metal oxide) and the template spheres could be removed, creating the negative replica of the opal structure, a so called inverse opal structure (see Figure 2.4 right).

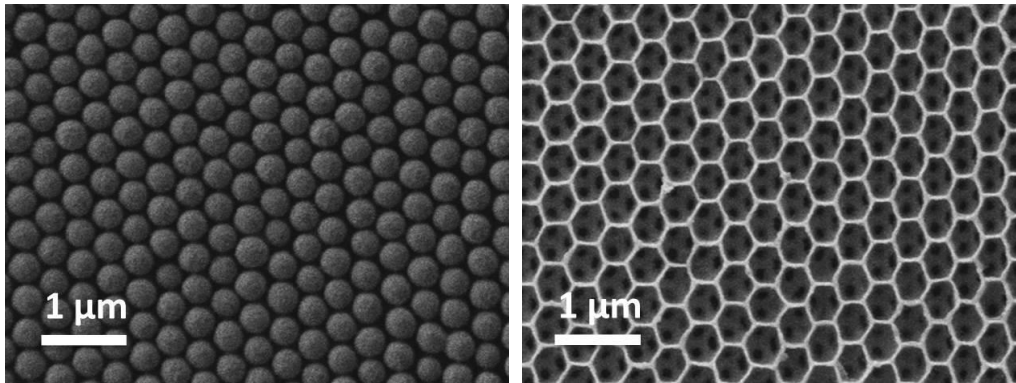


Figure 2.4: SEM images of a PMMA opal structure (left) and a ZnO inverse opal structure (right)

As shown in Figure 2.4, inverse opals consist of a regular arrangement of void spaces surrounded by solid walls. These ordered macroporous structures provide large and accessible specific surface area for diffusion and infiltration of gas or liquid, which made them attractive materials for applications in the fields of catalysis [12, 13], chemical sensing [14-24], optical switching [25], energy storage [26-28], etc. In the present work, inverse opals of tungsten oxide (WO_3) were used as optical sensors to detect gas, fluids and water temperature; these are discussed in more detail in section 2.3.

2.2 Synthesis of photonic crystals

2.2.1 Synthesis of polymer opal structures

The first step for building colloidal opals is the synthesis of spherical particles with uniform size distribution. Silica or polymer spheres like polystyrene (PS) or poly methyl-methacrylate (PMMA) are two main types of particles used for opal formation. Monodisperse silica particles are usually prepared with Stöber method [29], where dilute solution of tetraethylorthosilicate (TEOS) is hydrolyzed in ethanol at high pH and uniform SiO_2 spheres with diameters ranging from 50 nm to 2000 nm could be produced. Uniform PS and PMMA particles are mainly prepared with emulsion polymerization [30-33].

In classical emulsion polymerization the major components of this process include a monomer with low water solubility, an aqueous dispersion medium, a surfactant, and a water-soluble initiator. The monomer is dispersed into the aqueous phase with the help of the surfactant. The surfactant molecules are present as micelles and the majority of these micelles are swollen by the monomer. The formation of polymer particles begins with the decomposition of the water-soluble initiator, during which free radicals are produced. These radicals diffuse into the surfactant micelles and polymerize the dispersed monomer to form oligomers. These oligomers are further polymerized in the monomer swollen micelles and grow into spherical particles. The growth of spherical particles stops when all the monomer droplets are consumed. Preformed spherical particles can also be added prior to polymerization to form monomer-swollen particles, in which case seeded polymerization is obtained [34].

Surfactant-free emulsion polymerization (SFEP [33]) is the most used method for the fabrication of “clean” polymer spheres. SFEP is carried out in same way as in classical emulsion polymerization, except that no surfactant is used. In order to stabilize the particle, an initiator with charged end groups has to be applied. During the start of SFEP, the decomposition of the water-soluble initiator leads to the generation of free radical seeds, which then react to form oligomer. The surface-active oligomers can act as surfactant and self-assemble into micelles. The advantage of this method is that the micelle concentration is low and all the micelles grow at same rate, which result in more monodisperse polymer particles [35-36].

In the current study, monodisperse PMMA particles were fabricated with SFEP. Potassium peroxydisulfate ($K_2S_2O_8$) was selected as water-soluble initiator. The surface of PMMA particles is negatively charged with sulfate group (Figure 2.5, formed by the decomposition of $K_2S_2O_8$), as a result, the particles are ionically stabilized.

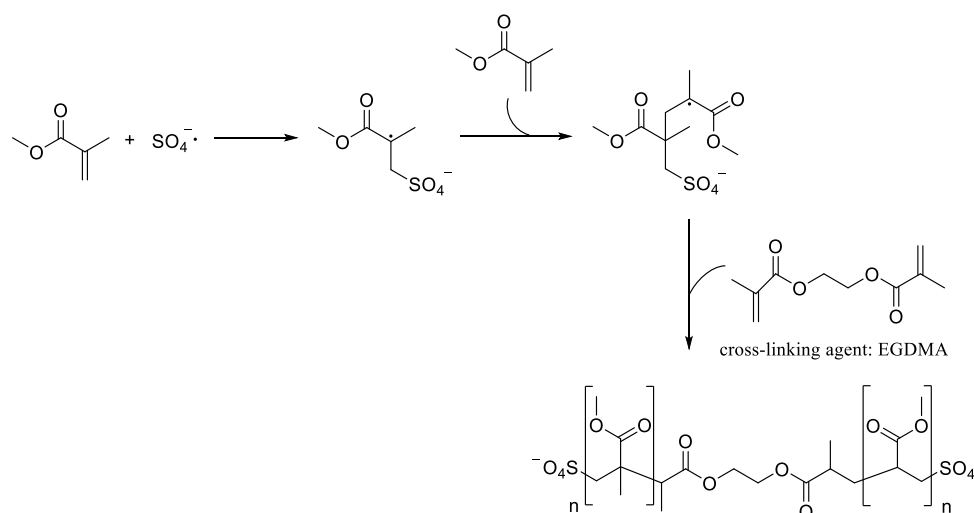


Figure 2.5: Reaction mechanisms of surfactant free emulsion polymerization

The glass transition temperature (T_g) is an important property for the synthesized polymer particles. T_g is defined as the temperature where an amorphous material transitions from a hard, glassy material to a soft, flexible material [37]. When the temperature of a polymer is below the T_g , polymer chains are rigid and therefore their mobility is restricted, causing the material to be hard or brittle. As the temperature rises above T_g , the polymer chains gain a higher degree of mobility, therefore the material becoming soft and flexible. It is necessary to investigate these different thermal behaviors of the synthesized polymer particles before using them as template materials for inverse opal structures. More details are discussed in the section 2.2.2.

Once the polymer spheres have been synthesized, the next step is to deposit the spheres onto a substrate. Various methods, including sedimentation [38, 39], vertical deposition [40-42] spin-coating [43-45], dip-coating [46-50], drop-casting [51-54], etc, have been developed for the assembly of the monodisperse particles into highly ordered structure.

In this work drop-casting was used to produce thick, ordered PMMA opal films. The advantages of this method are the easy handling of the process and the relatively easy control of the drying conditions. Figure 2.6 shows the corresponding mechanism of the crystallization process.

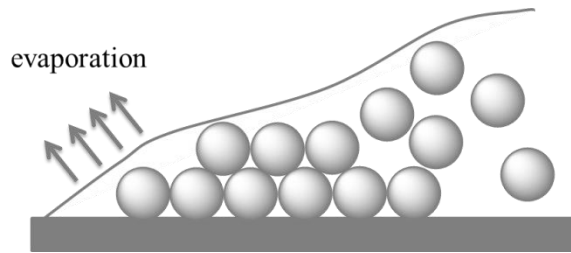


Figure 2.6: Schematic view of the crystallization process by drop-casting

Water droplets containing PMMA particles are deposited on glass substrates to fabricate ordered opal films. Here, the crystallization is initially driven by strong capillary attraction caused by the evaporation of water; other effects like Brownian motion or electrostatic repulsion also play an important role [55]. This process inevitably leads to uneven film surface (coffee ring effect), which is a consequence of the competition between the assembly rate and deposition rate of the colloidal particles [51]. Therefore, it is necessary to finely adjust the factors that influence the evaporation process (e.g. evaporation temperature, concentration of the colloidal dispersion, type of substrate, etc) to produce ordered opal structures.

2.2.2 Synthesis of metal oxide inverse opal structures

Colloidal crystal templating approach is the most common synthetic method to produce metal oxide inverse opals [30, 56-68]. This method is based on templated precipitation of inorganic precursors within a colloidal crystal of polymer spheres and subsequent chemical conversion. The process of this technique mainly involved four steps (see Figure 2.7): (1) a colloidal opal template is fabricated using monodisperse polymer particles, (2) the voids of the polymer template are filled with liquid metal oxide precursors, (3) the fluid precursor are then solidified in the template pores, and (4) an ordered metal oxide inverse opal is produced after removing the polymer template by calcination.

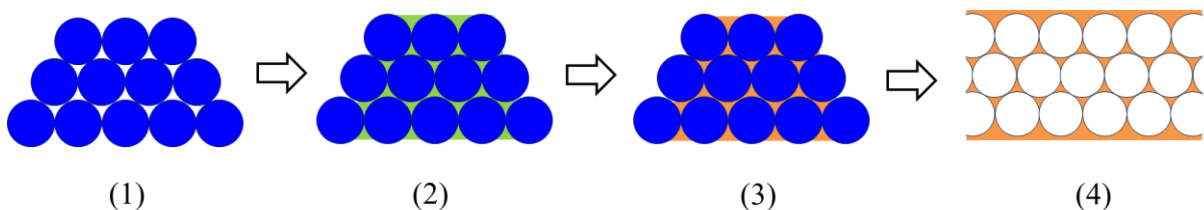


Figure 2.7: Schematic procedure used to fabricate metal oxide inverse opals

The prerequisite for successful replication of the polymer template is that the precursor material in the template voids must be as completely networked as possible to avoid collapsing during the calcination process. For this purpose, the fluid precursors should wet the polymer spheres well so that they can fully penetrate into template pores. In addition, the precursor material should have a high solubility in the solvent to maximize the amount of precursor loading.

Another key point of this templating method is the design of the precursor solidification process. Solidification techniques can be classified into a few categories, such as precipitation, chemical reaction, sol-gel transformation [61, 64], photodecomposition [69], etc., in terms of precursor type. The formation of a stable precursor network is of great necessity to obtain a well-ordered inverse opal structure [63]. As mentioned in the last section, polymer templates will lose their structural integrity at their glass transition temperatures (Figure 2.8 route (a)) and, if not stabilized properly, disordered arrangement will present at higher temperatures (Figure 2.8 route (b)). In these cases, only low ordered or disordered inverse opal structures can be obtained.

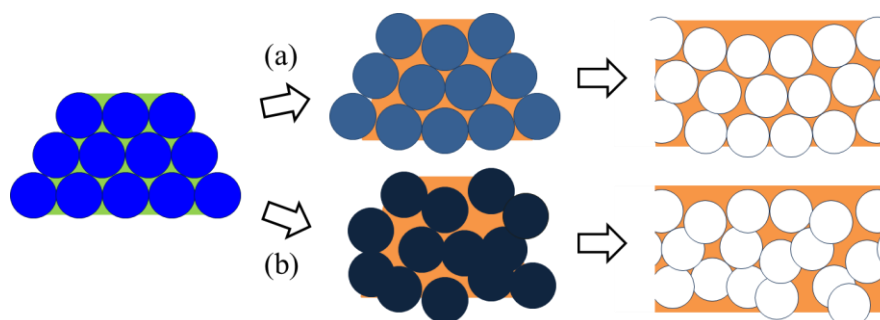


Figure 2.8: Solidification of precursors in low ordered template matrix (a) and in disordered template matrix (b)

As an alternative to solidification of precursor after infiltration, precursor solutions containing metal oxide nanoparticles can be directly infiltrated into the polymer opal template (Figure 2.9), and therefore, no further solidification procedures are needed during the calcination process [70-71]. The use of metal oxide nanoparticles enables dense packing within the interstitial volume of polymer template and thus reduces crack formation caused by the volume shrinkage of the inverse opal structure.

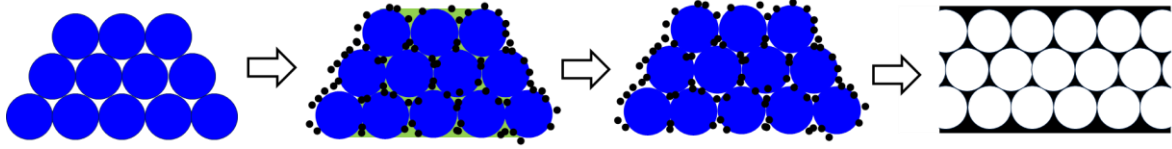


Figure 2.9: Schematic procedure of fabricating metal oxide inverse opals by nanoparticles infiltration (black points indicate metal oxide nanoparticles)

2.3 Optical sensing based on metal oxide inverse opals

Metal oxide inverse opals are a suitable transducer for many sensor applications. As mentioned in section 2.1, the change of effective refractive index of the metal oxide inverse opals will cause a shift of their corresponding reflection peak position (photonic band gap). This shift can be evaluated as an optical sensor signal. In this present work, three strategies were applied to change the effective refractive index of the inverse opals: (i) introducing chemical analytes in the pores of inverse opals (section 2.3.1); (ii) adsorption of a substance on the wall materials (section 2.3.2); (iii) gas reaction induced optical absorption (section 2.3.3).

2.3.1 Fluids sensing mechanism

The effective refractive index of inverse opals can be calculated according to the following equation [72, 73]

$$n_{eff}^2 = n_s^2 f_s + n_p^2 f_p \quad (2.4)$$

where n_s and $n_p (= 1)$ are the refractive index of the solid phase and the air phase in the pores of inverse opals, respectively, and f_s and $f_p (= 1 - f_s)$ are the volume fractions of these two respective phases.

According to Equation 2.4, when the air inside the void space of the inverse opals is replaced by a liquid-phase analyte with higher refractive index, such as acetone ($n_{acetone} = 1.359$ [74]), deionized water ($n_{water} = 1.333$ [75]), ethanol ($n_{ethanol} = 1.361$ [76]) or isopropyl alcohol ($n_{isopropy\ alcohol} = 1.379$ [77]), the effective refractive index of the inverse opals increases, which can be observed as peak shifts in the corresponding reflection spectra. Based

on this principle, metal oxide (WO_3) inverse opals were applied to detect the fluids mentioned above.

2.3.2 Water temperature sensing mechanism

Thermo-responsive block copolymer poly(diethyl-4-vinyl-benzyl-phosphonate-*b*-N-isopropylacrylamide) (P(DEVBP-*b*-NIPAAm)) is infiltrated into the pores of WO_3 inverse opals to test the optical sensing property for water temperature. P(DEVBP-*b*-NIPAAm) consists of two polymer blocks. The PDEVBP blocks are adsorbed on the inner surfaces of the inverse opals (through hydrogen bond with phosphonate anchor groups [78]) with PNIPAAm blocks forming the corona (Figure 2.10).

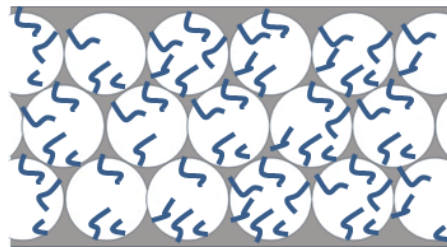


Figure 2.10: Temperature responsive block copolymer (blue) adsorbed on the inner surfaces of inverse opal pores

The critical solution temperature (T_c) of P(DEVBP-*b*-NIPAAm) is 30 °C [79], which indicates two different desorption behaviors after washing with different temperature water:

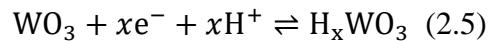
- (i) Water temperature < 30 °C: the block copolymer is hydrated and dispersed in water (desorbed from the oxide surface)
- (ii) Water temperature > 30 °C: the block copolymer is dehydrated and the interaction of the adsorbed polymers with the oxide surface becomes stronger due to intermolecular attractive forces (block copolymer remain adsorbed on the oxide surface)

In the case of water temperature lower than 30 °C, the desorption of the block copolymer induces a localized refractive index variation of the wall materials, which can be directly observed as color transition and enables a fast and easy method to detect water temperature limit.

2.3.3 H_2 sensing mechanism

Another strategy to modify the effective refractive index of the metal oxide inverse opals is based on gas reaction induced change of the optical absorption. For common semiconducting metal oxides, gas reactions usually lead to electrical property changes (e.g. conductance). Theoretically, since the microscopic electrical and macroscopic optical properties are closely related, the semiconducting metal oxides are also expected to exhibit gas-induced optical changes [80].

According to relevant studies, some metal oxides (e.g. Co_3O_4 [81], TiO_2 [82], SnO_2 [82], and WO_3 [83-86]) displayed optical responses to various gases, however, the optical responses were weak compared with their electrical responses. Among these examples, transmission [81, 82, 84, 85] or reflection [83, 87] are measured for materials of different structures, including unstructured thin films [81, 83], nanoparticles [82] and photonic crystals [85, 86]. In spite of the differences, the optical response of metal oxides was found to be always relying on the gasochromic effect, with a typical example being H_2 induced optical constant variation of WO_3 [83-90]. While several studies are conducted for this effect for amorphous WO_3 [91, 92], the mechanism of free carrier absorption is widely accepted for crystalline WO_3 which is also the subject material in the current study. The chemical process of this absorption effect can be explained by the double injection model [89, 92]



where the protons (H^+) dissociated from H_2 gas on metal catalysts and the accompanied free electrons (e^-) are injected into WO_3 to form a more absorbing material called hydrogen tungsten bronze (H_xWO_3). As sketched in Figure 2.10, H_2 serve as doping agent and cause the free electrons to move into the conduction band of the n-type WO_3 [80, 92]. The presence of free carrier electrons gives rise to new absorption mechanisms, which is the predominant origin of the effective refractive index change. The general principles are discussed below.

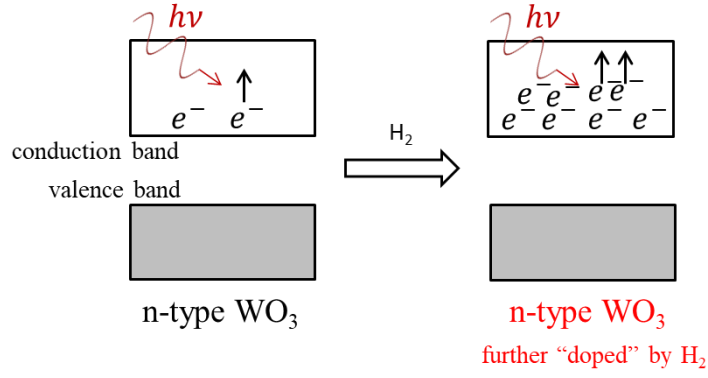


Figure 2.11: Sensing mechanism of WO_3/H_2 system

If light with a frequency ω scattered on the “doped” WO_3 , the dispersion and refraction of light can be described by the complex refractive index ($n_c(\omega)$) through

$$n_c(\omega) = n(\omega) + ik(\omega) \quad (2.6)$$

Where the real part $n(\omega)$ is the average refractive index of the material and imaginary part $k(\omega)$ is the extinction coefficient. $k(\omega)$ is directly related to the absorption coefficient (α) with following equation

$$\alpha = \frac{4\pi k(\omega)}{\lambda} \quad (2.7)$$

Where λ is the vacuum wavelength of the light.

The refractive index is related to its relative permittivity ϵ_r through

$$n = \sqrt{\epsilon_r} \quad (2.8)$$

This indicates that if n is complex, then ϵ_r must also be complex. Therefore the complex relative permittivity $\epsilon_c(\omega)$ can be written as

$$\epsilon_c(\omega) = \epsilon_1(\omega) + i\epsilon_2(\omega) \quad (2.9)$$

Where $\epsilon_1(\omega)$ and $\epsilon_2(\omega)$ representing the real and imaginary part of the complex relative permittivity.

Based on Equation 2.7, 2.8 and 2.9, the relationships between the real and imaginary parts of the complex refractive index and complex relative permittivity are

$$\epsilon_1(\omega) = n(\omega)^2 - k(\omega)^2 \quad (2.10)$$

$$\epsilon_2 = 2n(\omega)k(\omega) \quad (2.11)$$

and

$$n(\omega) = \frac{1}{\sqrt{2}}(\epsilon_1(\omega) + \sqrt{(\epsilon_1(\omega))^2 + \epsilon_2(\omega)^2})^{1/2} \quad (2.12)$$

$$k(\omega) = \frac{1}{\sqrt{2}}(-\epsilon_1(\omega) + \sqrt{(\epsilon_1(\omega))^2 + \epsilon_2(\omega)^2})^{1/2} \quad (2.13)$$

These analyses show that $n_c(\omega)$ and $\epsilon_c(\omega)$ are not independent variables. $n(\omega)$ and $k(\omega)$ can be calculated from $\epsilon_1(\omega)$ and $\epsilon_2(\omega)$, and vice versa.

Back to the discussion of the effect of free electrons, as mentioned before, for n-type WO_3 the gas induced free electrons moving into its conduction band, the corresponding optical properties can be explained by classical Drude model using following equation

$$\epsilon(\omega) = \epsilon_1(\omega) + i\epsilon_2(\omega) = \epsilon_\infty - \frac{\omega_p^2}{i\omega\gamma + \omega^2} \quad (2.14)$$

and $\epsilon_1(\omega)$ and $\epsilon_2(\omega)$ are defined as

$$\epsilon_1(\omega) = \epsilon_\infty - \frac{\omega_p^2}{\omega^2 + \gamma^2} \quad (2.15)$$

$$\epsilon_2(\omega) = \frac{\omega_p^2\gamma}{\omega^3 + \omega\gamma^2} \quad (2.16)$$

In the equations above, ϵ_∞ is the background permittivity at high frequency, γ is the damping coefficient and ω_p is the plasma frequency. ω_p is related to the free electron density N_{free} and the effective conduction-band mass m through

$$\omega_p = \sqrt{\frac{N_{free}e^2}{\epsilon_0 m}} \quad (2.17)$$

Where e is the electronic charge and $\epsilon_0 = 8.854 \times 10^{-12}$ As/Vm is the permittivity of free space.

According to Equation 2.17, 2.16, 2.11 and 2.7, the increase of the free electron density N_{free} eventually leads to the increase of absorption coefficient, which demonstrates the direct correlation between the electrical and optical properties of the ‘‘doped’’ WO_3 .

On the basis of the Drude model, Figure 2.12 illustrates the relationship between the refractive index and extinction coefficient (proportional to absorption coefficient) of WO_3/H_2 system. It is obvious that, the free carrier absorption lead to a strong dispersion of refractive index of WO_3 after reaction with H_2 and the effect becomes stronger when the hydrogen concentration increased. Based on this deeper understanding, a series of WO_3 inverse opals with different photonic band gap positions were examined to maximize the optical response (reflection peak shift) towards H_2 .

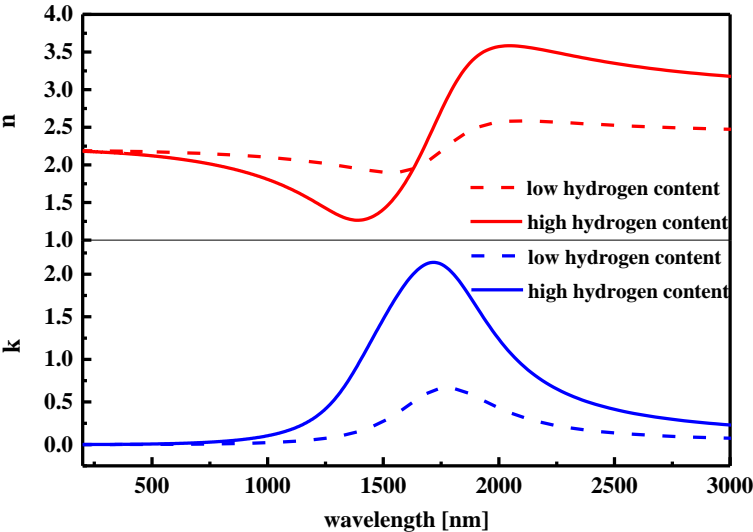


Figure 2.12: Relationship between refractive index n and extinction coefficient k of WO_3 after exposed to H_2 (Estimated based on Drude model)

3. Experiment

3.1 Synthesis of polymer opal structures

3.1.1 Synthesis of PMMA particles

Monodisperse PMMA particles were prepared by surfactant-free emulsion polymerization [33]. Following a standard synthesis procedure, a two-necked flask was placed in an oil bath at 100 °C, charged with 400 mL deionized water and sealed with a septum prior to being flushed with N₂ for 2 h. Subsequently, 21.3 mL methyl methacrylate (MMA, 0.5 mol·L⁻¹) and 0.57 mL ethylene glycol dimethacrylate (EGDMA, 1.5 mol% based on MMA) were slowly injected in water and stirred for 20 minutes. To start the polymerization, an aqueous solution of potassium persulfate (K₂S₂O₈, 27 mg dissolved in 1 mL water) was added to the mixture and stirred for another 2 h at 100 °C. Afterwards, the flask was opened to stop the polymerization and the remaining monomer was evaporated overnight. For purification the white solution was filtered using a standard paper filter to remove the large agglomerations.

In this work, the diameter of PMMA particles was varied by multiple additions of the monomer MMA and cross-linking agent EGDMA. The detailed reaction conditions are indicated in Table 3.1.

Table 3.1: Reaction conditions for variation of PMMA particle size

	Concentration of MMA (mol·L ⁻¹)	Volume of MMA (mL)	Volume of EGDMA (mL)	Mass of K ₂ S ₂ O ₈ (mg)	Reaction time (h)
PMMA-0.5M	0.5	21.3	0.57	27	2
PMMA-1.25M	1.25	21.3	0.57	27	2
		32	0.86	40	2
PMMA-2.5M	2.5	21.3	0.57	27	2
		42.6	1.14	54	2
		42.6	1.14	54	2
PMMA-3.5M	3.5	21.3	0.57	27	2
		42.6	1.14	54	2
		42.6	1.14	54	2
		42.6	1.14	54	2
PMMA-5M	5	21.3	0.57	27	2
		42.6	1.14	54	2
		42.6	1.14	54	2

42.6	1.14	54	2
64	1.70	81	2

3.1.2 Synthesis of PMMA opals

PMMA particles were then applied to crystallize into PMMA opals by using a simple drop deposition method. In order to prevent any potential interaction between particles, all the PMMA dispersion was first diluted to 5 wt%. Then a drop of 40 μL PMMA dispersion was deposited onto a cleaned glass substrate (with acetone and ethanol) and dried at 60 $^{\circ}\text{C}$ for 5 min. In addition, nitrocellulose membrane was also taken as substrate to generate thicker PMMA opals. The optical properties of the opals were investigated with reflectance spectroscopies.

3.2 Synthesis of metal oxide inverse opal structures

In this work metal oxide inverse opals of CeO_2 , CuO , Cr_2O_3 , Fe_2O_3 , Ga_2O_3 , In_2O_3 , SnO_2 , TiO_2 , WO_3 and ZnO were fabricated using the colloidal crystal templating method. Among them, CeO_2 , CuO , Cr_2O_3 , Fe_2O_3 , Ga_2O_3 , In_2O_3 and ZnO inverse opals were synthesized through infiltration of PMMA opals with an ethanol solution of respective metal nitrate. To prepare SnO_2 , TiO_2 , WO_3 inverse opals, tin(IV) chloride pentahydrate ($\text{SnCl}_4 \cdot 5\text{H}_2\text{O}$), titanium(IV) butoxide ($\text{Ti}(\text{OCH}_2\text{CH}_2\text{CH}_2\text{CH}_3)_4$) as well as ammonium metatungstate hydrate ($(\text{NH}_4)_6\text{H}_2\text{W}_{12}\text{O}_{40} \cdot x\text{H}_2\text{O}$) were used as metal oxide precursors respectively.

3.2.1 Pure metal nitrates as precursors

All of the metal nitrates were dried under vacuum previous to preparing the precursor solution. The concentrations of metal nitrates have been studied in the range of 30 - 50 wt%. In a standard synthesis procedure, respective metal nitrates (Table 3.2) were first dissolved in absolute ethanol to obtain 30 wt%, 40 wt%, 50 wt% precursor solution. Then, 2 μL of the precursors were carefully dropped on the surface of PMMA opals and dried at room temperature to remove the solvent. The drying conditions related to the hygroscopicity of the precursor. For high hygroscopic metal nitrate like copper nitrate, indium nitrate and zinc nitrate, a second drying process at 60 $^{\circ}\text{C}$ is necessary to further remove the residual solvent. The details about drying conditions are given in Table 3.2. After the solvent was dried out, the

resulting composite was calcined in an ashing furnace at 350 °C with a rising rate of 1 °C·min⁻¹. This temperature was maintained for 2 h to complete remove the PMMA template.

Table 3.2: Inverse opal synthesis conditions with pure metal nitrates as precursors

	precursor	drying condition
CeO ₂	Ce(NO ₃) ₂ ·6H ₂ O in ethanol	40 °C (24 h)
CuO	Cu(NO ₃) ₂ ·2.5H ₂ O in ethanol	room temperature (24 h), then 60 °C (72 h)
Cr ₂ O ₃	Cr(NO ₃) ₃ ·9H ₂ O in ethanol	room temperature (24 h)
Fe ₂ O ₃	Fe(NO ₃) ₃ ·6H ₂ O in ethanol	room temperature (24 h)
Ga ₂ O ₃	Ga(NO ₃) ₃ ·xH ₂ O in ethanol	40 °C (24 h)
In ₂ O ₃	In(NO ₃) ₃ ·xH ₂ O in ethanol	room temperature (24 h), then 60 °C (72 h)
ZnO	Zn(NO ₃) ₂ ·6H ₂ O in ethanol	room temperature (24 h), then 60 °C (72 h)

3.2.2 Modified metal nitrate as precursors

3.2.2.1 Organic chelating with citric acid

In the preparation of CeO₂, CuO and ZnO precursors, citric acid was added into their metal nitrate ethanol solution and stirred for 2 h at room temperature. The concentrations of the citric acid as well as respective metal nitrates are indicated in Table 3.3. Subsequently, 2 μL of the precursor were infiltrated into PMMA templates as mentioned before. The composite film was dried at room temperature overnight and then converted into desired metal oxide at 350 °C for 2 h with a heating rate of 1 °C·min⁻¹.

Table 3.3: Concentration of citric acid and metal nitrate for preparation of the modified metal nitrate precursors

	precursor
CeO ₂	Ce(NO ₃) ₂ ·6H ₂ O (0.43 g, 1 mmol) + citric acid (0.19 g, 1 mmol) in 1.27 mL ethanol
CuO	Cu(NO ₃) ₂ ·2.5H ₂ O (0.23 g, 1 mmol) + citric acid (0.19 g, 1 mmol) in 0.68 mL ethanol
ZnO	Zn(NO ₃) ₂ ·6H ₂ O (0.30 g, 1 mmol) + citric acid (0.19 g, 1 mmol) in 0.89 mL ethanol

3.2.2.2 Sol-gel polymerization of TEOS

To synthesize ZnO inverse opal, another precursor solution was derived from mixing Zn(NO₃)₂·6H₂O (0.30 g, 1 mmol) and citric acid (0.19 g, 1 mmol) into a mixture of 0.5 mL ethanol and 0.5 mL H₂O. Afterwards, a small quantity of TEOS was dropped into the mixture

and stirred for 2 h at room temperature. The amount of TEOS varied from 0.5 vol% to 10 vol%. Then the prepared precursor solution was used to infiltrate into the pores of PMMA templates. After completely drying (room temperature overnight), the samples were heated to 350 °C at a rate of 1 °C·min⁻¹ and kept for 3 h to remove the PMMA template.

3.2.2.3 *Polyacrylamide gelation*

Another strategy to produce ZnO inverse opal is the polyacrylamide gelation method. According to this method, Zn(NO₃)₂·6H₂O (0.30 g, 1 mmol) was first dissolved in 0.89 mL absolute ethanol. Then acrylamide (0.14 g, 2 mmol) and bisacrylamide (0.06 g, 0.4 mmol) were added into the precursor solution, followed by adjusting the pH value to 3 with aqueous ammonia. After stirring for 2 h, 2 μL of this mixture were infiltrated into PMMA templates. Then, in an ashing furnace the composite was heated to 80 °C for 2 h to initiate the polymerization [93] and dried at 120 °C for another 2 h. Finally, the calcination temperature was increased at a rate of 1 °C·min⁻¹ to 500 °C and maintained for 2 h to remove the obtained polyacrylamide xerogel and yield ZnO inverse opal structure.

3.2.3 *Synthesis of SnO₂ inverse opals*

In order to prepare SnO₂ precursor, SnCl₄·5H₂O (0.19 g, 0.54 mmol) was dissolved in a mixture of 0.3 mL H₂O and 0.03 mL absolute ethanol (V_{water}:V_{EtOH}=10:1). Then, the mixture was stirred for 30 min at room temperature. The prepared precursor solution was used to infiltrate into PMMA template at 60 °C. When the infiltration was complete, the sample was dried at room temperature for 24 h. Finally, the resulting composite was calcined in air at 500 °C for 4 h with a rising rate of 0.5 °C·min⁻¹.

3.2.4 *Synthesis of TiO₂ inverse opals*

TiO₂ inverse opals were synthesized from a mixture of 0.04 mL titanium(IV) butoxide, 0.12 mL ethanol and 0.04 mL concentrated hydrochloric acid (HCl). The mixture was stirred at room temperature for 30 min prior to infiltrate into PMMA opals. Subsequently, 2 μL of the precursor were dropped on the PMMA templates and left to dry in air at room temperature for 15 min, followed by drying at 50 °C overnight. Finally the samples were heated to 500 °C at 1 °C·min⁻¹ and held for 2 h.

3.2.5 *Synthesis of WO₃ inverse opals*

To fabricate WO₃ inverse opals, ammonium metatungstate hydrate (0.20 g, 0.07 mmol) was dissolved in 0.08 mL deionized water. Then, 0.02 mL of this solution were diluted in a mixture of 0.08 mL ethanol and 0.02 mL water. A droplet of this prepared solution (0.002 mL) was deposited on the surface of PMMA template and filled into spherical voids owing to capillary forces. After infiltration, the sample was dried at 60 °C for 3 h. Finally, the resulting composite was calcined in air at 400 °C with a rising rate of 0.5 °C·min⁻¹. This temperature was maintained for 5 h to remove the PMMA template completely.

The obtained WO₃ inverse opals were used to test the optical gas sensing property towards H₂ (section 3.3.9). In order to enhance the decomposition rate of H₂, the samples were loaded with platinum (Pt) before measurements. First, 0.05 g hexachloroplatinic acid (H₂PtCl₆) were dissolved in 0.10 mL deionized water. Then, 0.002 mL of this aqueous solution was carefully dropped on the surface of inverse opals and subsequent thermally converted in air (300 °C, 0.5 °C·min⁻¹, 2h).

3.3 Characterization Methods

3.3.1 *Dynamic Light Scattering*

The diameters of PMMA spheres were determined by dynamic light scattering (DLS) on a Zetasizer Nano S90 from Malvern. A drop of PMMA dispersion was diluted with deionized water to form a clear solution before measurements.

3.3.2 *Powder X-ray Diffraction*

Powder X-ray diffraction (P-XRD) was carried out on a Bruker D8 Advance diffractometer using a Cu K_α target with a wavelength of 1.54 Å. The measurements in the wide-angle region (20 ° - 80 °) were taken for the determination of the crystal structure of the synthesized inverse opals. For preparation, the sample (on the glass substrate) was carefully placed on a sample holder and fixed using scotch tape.

3.3.3 *Fourier-Transform Infrared Spectroscopy*

Fourier-transform infrared spectroscopy (FTIR) was conducted on a Bruker Vertex 70 spectrometer, installed with a Bruker Hyperion 1000 microscope system. The reflection of

samples was collected over the range 400 – 1000 nm (visible area) or 800 – 2000 nm (near-infrared (NIR) area). Xenon light source, Si-diode D510 detector and 4x magnification refraction objective were employed to perform measurement in the visible range, whereas tungsten light source, mercury cadmium telluride detector and 36x magnification refraction objective were utilized in the NIR range.

3.3.4 *Scanning Electron Microscopy*

Scanning electron micrographs (SEM) were recorded with Neon 40 from Zeiss. For sample preparations, all the inverse opals were adhered to the aluminum sample holder and sputtered with gold and palladium (4 nm in thickness) before measurement. The PMMA diameters, the pore size of inverse opals and the microstructure of all samples were then verified utilizing SEM images.

3.3.5 *Thermogravimetric Analysis*

The thermal decomposition behavior of PMMA particles and PMMA/metal nitrate composites were characterized with thermogravimetric analysis (TGA). The measurements were carried out under O₂/N₂ flow ($V_{O_2}:V_{N_2} = 20 : 80$) with TGA/SDTA851 from Mettler Toledo. The ion currents were measured by a connected Pfeiffer Vacuum OmniStar mass spectrometer. The heating program was from room temperature to 500 °C with a heating rate of 1 °C·min⁻¹. Onset temperatures were determined from the combined derivative thermogravimetry (DTG) curves and mass spectrometry (MS) signals. The powdery samples of PMMA/metal nitrate composites were collected from 40 synthesized films (prior calcination).

3.3.6 *Differential Scanning Calorimetry*

The glass transition temperature of synthesized PMMA particles was determined by differential scanning calorimetry (DSC). The measurement was taken under nitrogen (N₂) atmosphere with DSC 204 F1 Phoenix from Netzsch. The heating rate was 10 °C·min⁻¹. The glass transition temperature obtained from second heating run and determined as the temperature at the inflection point of the change in heat flow. Before measurement the PMMA powders were dried in vacuum overnight.

3.3.7 Fluids Sensing Measurements

The fluids sensing measurements were carried out in ambient air at room temperature. Different fluids including acetone, ethanol, isopropyl alcohol and water were successively applied by placing a drop on the top surface of WO_3 inverse opals. The reflection spectra of WO_3 inverse opals before and after introducing each fluid were measured with fourier-transform infrared spectroscopy (FTIR).

3.3.8 Water Temperature Sensing Measurements

Each 5 μL aqueous solution of poly(diethyl-4-vinyl-benzyl phosphonate-*b*-*N*-isopropylacrylamide) (P(DEVBP-*b*-NIPAAm), 32 $\text{mg}\cdot\text{mL}^{-1}$) was carefully dropped onto the surface of three WO_3 inverse opals and filled into the air-containing pores due to capillary forces. The infiltrate samples were dried at room temperature for 24 h and subsequently washed with 2 mL 20 °C, 40 °C and 60 °C water, respectively. The optical reflection of WO_3 inverse opals before adsorption, after adsorption and after washing with different temperature water were characterized with fourier-transform infrared spectroscopy (FTIR).

3.3.9 H_2 Sensing Measurements

The H_2 sensing measurements of the WO_3 inverse opals were performed in a custom-built mobile gas sensing setup (Figure 3.1).

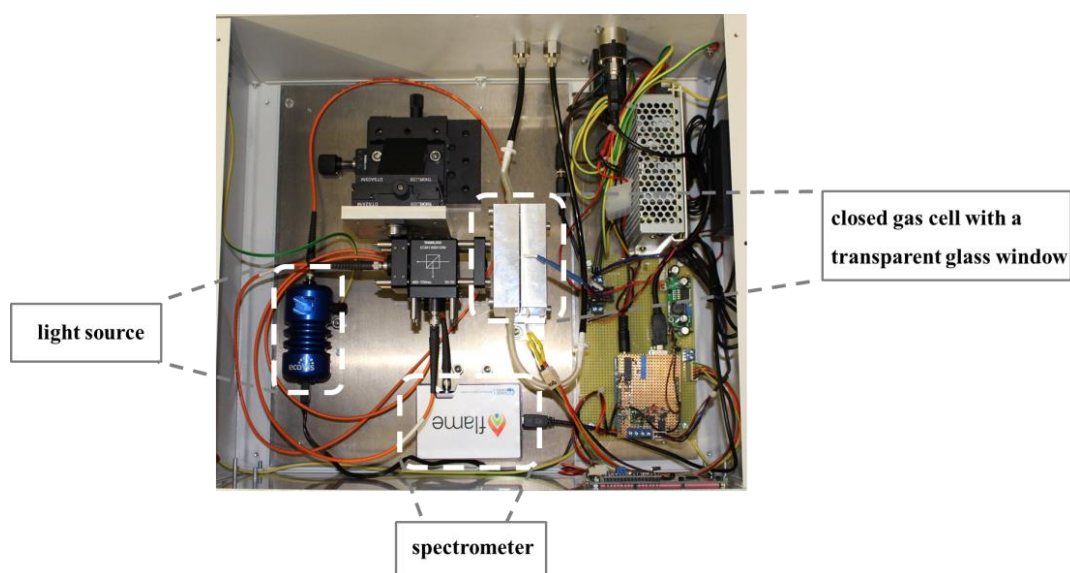


Figure 3.1: Photograph of the mobile gas sensing setup

To measure the reflection of samples krypton light source (ecoVis, Ocean Optics) was used. The light first passes through a beam splitter, with the focus placed on the surface of the

sample. The reflected light passes through the beam splitter as well before return to the spectrometer. Two different dispersive CCD spectrometers (from Ocean Optics) and AvaSpec-USB2 (from Avantes) were involved to record the in-situ reflection spectra in the visible and near IR areas, respectively. In the closed gas cell, the WO_3 inverse opal (on glass substrate) was placed on a ceramic heater to measure the sensing properties at 140 °C. The test gas is H_2 in N_2 , whose concentration ranging from 0.1 vol% to 1 vol%. After each H_2 -pulse, the gas cell was flushed with synthetic air to allow the regeneration and then with pure N_2 to prepare the next H_2 -pulse.

The H_2 sensing performance was also tested in an open system at 200 °C. In this measurement, H_2 in N_2 was used as test gas, the concentration of H_2 varied from 0.3 vol% to 10 vol%. After the exposure of test gas, pure N_2 was introduced to facilitate the regeneration of WO_3 .

4. Results and Discussion

4.1 Polymer opal structures

4.1.1 PMMA particles

The optical quality of the PMMA opals is highly influenced by the monodispersity of the PMMA spheres used to grow colloidal photonic crystals [94]. In this present work, monodisperse PMMA spheres were synthesized by surfactant free emulsion polymerization and the particle sizes were adjusted by the variation of the monomer (MMA) concentration.

Table 4.1: Effect of MMA concentration on the diameters and polydispersity of PMMA spheres

	PMMA- 0.5M	PMMA- 1.25M	PMMA- 2.5M	PMMA- 3.5M	PMMA- 5M
MMA concentration (mol·L ⁻¹)	0.5	1.25	2.5	3.5	5
diameters of PMMA (nm) ^a	315	432	536	583	655
diameters of PMMA (nm) ^b	298±5	425±7	502±9	572±8	644±6
polydispersity (PDI) ^a	0.004	0.025	0.015	0.040	0.088

^a Determined by dynamic light scattering (DLS); ^b Determined by scanning electron microscopy (SEM)

The diameters of the synthesized PMMA particles are listed in Table 4.1. The values were characterized by both DLS and SEM. With DLS, the diameters were measured using a diluted PMMA dispersion. With SEM, 100 PMMA particles were taken from each SEM image. The mean value and the standard deviation of the diameter were then calculated. As expected, the diameters measured by DLS are larger than the diameters from SEM. The differences reflect the fact that SEM only measures the diameters of the individual particles, while DLS measures the hydrodynamic diameter, which also involves a hydrate shell. Therefore, the values obtained by DLS are always greater than the actual diameters of PMMA particles. The monodispersity of the PMMA particles can be gauged from the polydispersity index (PDI) obtained by DLS. PDI is defined as the standard deviation (σ) of the particle diameter distribution divided by the mean particle diameter (D)

$$PDI = \frac{\sigma}{D} \quad (4.1)$$

Larger PDI values correspond to a larger size distribution of the particles. Samples with PDI value less than 0.1 [95] can be considered as monodisperse. From the PDI values given in Table 4.1, it is apparent that each synthesized PMMA sample is monodisperse and thus suitable for making high quality artificial opal structures.

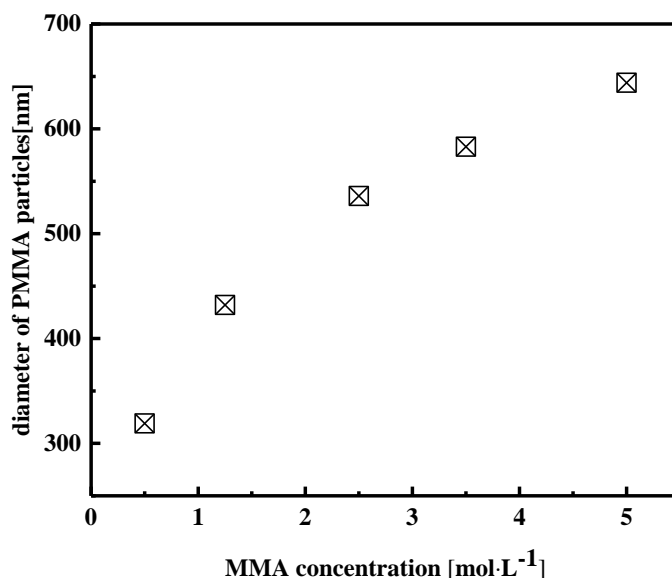


Figure 4.1 The relationship between the MMA concentration and the diameters of PMMA particles (from DLS)

The monomer concentration is obviously one of the variables that directly influence the particle size. From Figure 4.1, the diameter of PMMA particle increases with successively increasing MMA concentration. By changing the monomer concentration from 0.5 mol·L⁻¹ to 5 mol·L⁻¹, the diameters of PMMA particles can be adjusted from 315 nm to 655 nm. In the two-stage emulsion polymerization the initially formed PMMA particles act as seed particles and the latter added monomer continually grow polymeric chain on the particle surface. The growth of the polymer particles stops when all monomer droplets are consumed.

It can be seen that, if the MMA concentration is lower than 2.5 mol·L⁻¹, the resulting particle sizes increases almost linearly with the monomer concentration. This means that all the later added monomer reacts at the surface of the initial PMMA particle and contributed the increase in particle size as the polymerization proceeds. However, the growth of particle size slows down with further increasing the MMA concentration. In this case, in addition to continuing polymerize onto the initial PMMA particles, new particles were also created in the

water solution. This is confirmed by the results from SEM (see Figure 4.2 (d) and (e)), where small PMMA particles also exist.

Besides that, the addition of new initiator is also important for particle enlargement [96]. The initiator $\text{K}_2\text{S}_2\text{O}_8$ (or rather SO_4^-) acts as ionic stabilizer at the particle surface. During the polymerization, particles tend to aggregate with other particles if they don't have sufficient SO_4^- end groups to maintain stable. Since rapid aggregation may lead to particles with different sizes, additional initiator has to be applied to produce larger monodisperse PMMA particles.

In my previous work, PMMA particles larger than 700 nm can be obtained at MMA concentrations higher than $5 \text{ mol}\cdot\text{L}^{-1}$. But the ionic stabilization with SO_4^- is no longer possible. Aggregation takes place and results in a broader size distribution. These particles are therefore not suitable for colloidal crystal construction.

Beside monomer concentration, two alternative variables can also be applied to increase the PMMA particle size: either using lower reaction temperature [97] or adding other steric stabilizer (e.g. Poly(N-vinylpyrrolidone) [98]). At a lower reaction temperature, the MMA monomer needs more time to completely polymerize, allowing polymer chains to grow larger before forming spherical particles [97]. By adding other steric stabilizer, particles of larger sizes will be stabilized which favors the particle growth rather than aggregation or forming new spherical particles.

4.1.2 PMMA opals on glass substrates

The as synthesized PMMA particles were then used to crystalize into PMMA opals on cleaned glass substrates. The structural orders were analyzed by scanning electron microscopy. Figure 4.2 shows the SEM images of PMMA opals fabricated with different sizes of template particles. In all cases, regular arrangements of spherical particles are observed and in each PMMA opal the template spheres have highly uniform particle sizes.

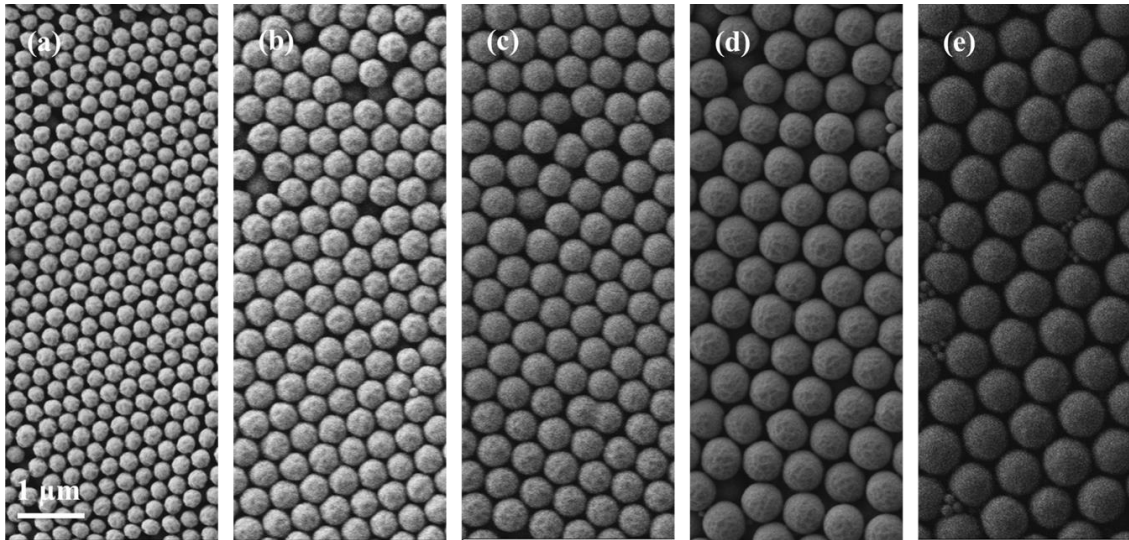


Figure 4.2: SEM images of PMMA opals with different pore sizes: (a) 298 nm, (b) 425 nm, (c) 502 nm, (d) 572 nm and (e) 644 nm; The diameters were obtained by measuring 100 particles in each sample

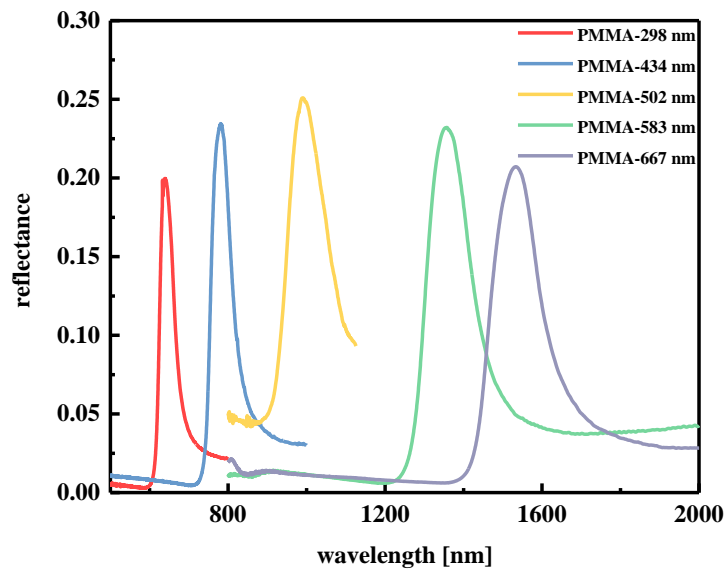


Figure 4.3: FTIR spectra of PMMA opals with different sizes of template particles

To analyze the optical property of these inverse opals, their reflection spectra were measured by fourier-transform infrared spectroscopy. The measured reflection spectra show well defined peaks with the maximum peak position varied from visible to near-IR range (see Figure 4.3). Table 4.2 summarizes the band gap positions and the diameters of corresponding template particles.

Table 4.2: Summary of the band gap position of PMMA opals and the diameters of corresponding PMMA particles

	PMMA- 0.5M	PMMA- 1.25M	PMMA- 2.5M	PMMA- 3.5M	PMMA- 5M
diameters of PMMA particles (nm) ^a	298±5	425±7	502±9	572±8	644±6
band gap position of PMMA opals (nm)	635	781	990	1353	1538

^a Determined by scanning electron microscopy (SEM)

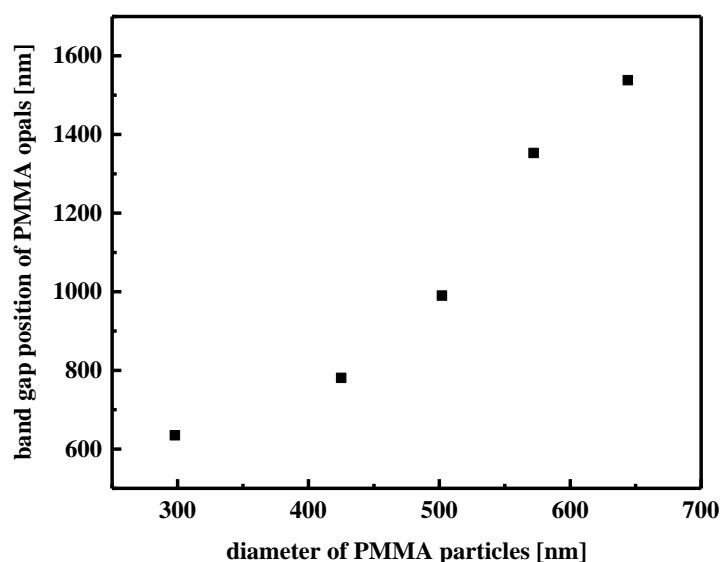


Figure 4.4: Relationship between the band gap position of PMMA opals and the diameters of corresponding PMMA particles

Based on the data from Table 4.2, the relationship between the band gap positions of PMMA opals and the diameters of corresponding PMMA particles are revealed. It is obvious that the maximal reflection peak positions of the PMMA opals shift to longer wavelengths when the diameters of template particles increase (Figure 4.4).

In summary, the monomer concentration can be adjusted to produce monodisperse PMMA spheres of average diameter from 298 nm to 644 nm (determined by SEM). Using the synthesized PMMA particles, the maximal reflection peak position of resulting PMMA opals

varied from 635 nm to 1538 nm. These PMMA opals were later used for fabricating metal oxide inverse opals with different photonic band gap positions.

4.1.3 PMMA opals on nitrocellulose substrates

Nitrocellulose substrates with hydrophobic surface were also used to produce high quality PMMA opals. As shown in Figure 4.5, a gently deposited PMMA drop has higher contact angle on hydrophobic surface (nitrocellulose substrate) than on less hydrophilic surface (glass substrate). Consequently, a thick PMMA opal film (*ca.* 1 mm) was obtained on a nitrocellulose substrate (see Figure 4.6 right).



Figure 4.5: Contact angle Θ of a drop of PMMA dispersion on a glass substrate (left), and on a nitrocellulose substrate (right)

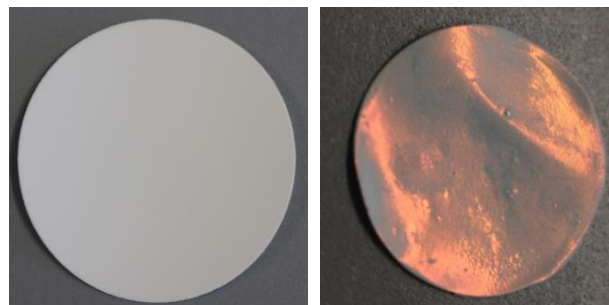


Figure 4.6: Photo of a nitrocellulose substrate (left) and a PMMA opal deposited on the nitrocellulose substrate (right, PMMA size: 315 nm)

Figure 4.7 shows the microscope pictures of the PMMA opal on nitrocellulose substrate as well as the sample on the glass substrate for comparison. Both PMMA opals display strong red opalescence, but the sample prepared on the nitrocellulose substrate exhibit larger domain (less cracks) compared to the sample prepared on glass substrate. This is consistent with the results from fourier-transform infrared spectroscopy (see Figure 4.8), where the PMMA opal on the nitrocellulose substrate has twice the reflectance of the sample on glass substrate.

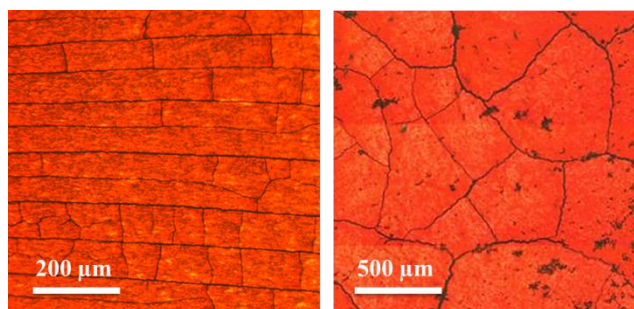


Figure 4.7: Microscope pictures of PMMA opal deposited on a glass substrate (left) and on a nitrocellulose substrate (right)

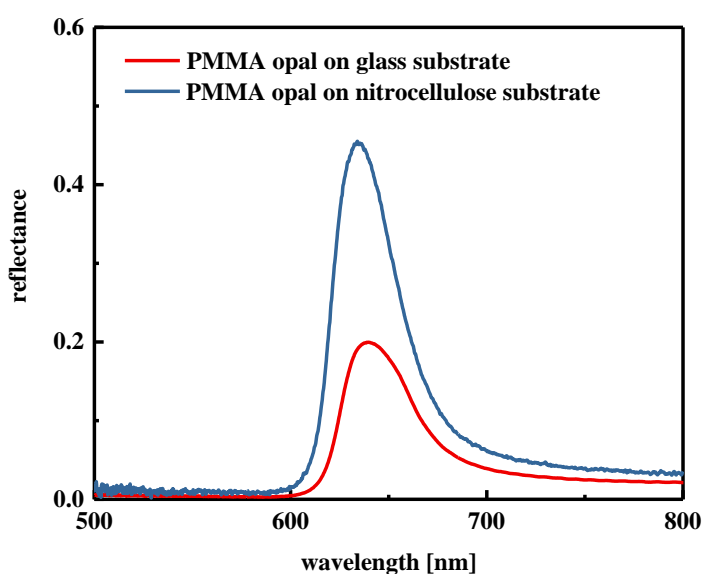


Figure 4.8: FTIR spectra of PMMA opal deposited on different substrates

The synthesized PMMA opals were then applied to fabricate metal oxide inverse opals using crystal templating method. Although the samples prepared on nitrocellulose substrate have higher reflectance (better opal qualities), the nitrocellulose itself is unstable at a temperature higher than 200 °C [99] and therefore not suitable for thermal conversion of precursor material. So the samples prepared on the glass substrates are used as opal templates.

4.2 Metal oxide inverse opals

As mentioned in the introduction, to obtain highly ordered inverse opals, several requirements should be satisfied by both the solvent and precursor (see 2.2.2). First, the liquid precursors should wet the PMMA spheres well so that they can fully penetrate into the void of templates through capillary force. In addition, the precursor material should have a high solubility in the solvent to increase the amount of precursor loading. In the synthesis of CeO_2 , CuO , Cr_2O_3 , Fe_2O_3 , Ga_2O_3 , In_2O_3 and ZnO inverse opals, respective metal nitrate ethanol solutions were chosen as starting materials because of their high solubility and good wettability. The infiltration and processing conditions differ from precursor to precursor and need to be optimized according to different solvent/precursor natures. In the next section, synthesis of Ga_2O_3 inverse opal was used as an example to explain how the precursor concentration, drying condition and thermal conversion temperature affect the optical property of the resulting inverse opals. Here PMMA opals with sphere size of 502 nm (from SEM) served as crystal templates.

4.2.1 Pure metal nitrate as precursors

4.2.1.1 Ga_2O_3

Precursor concentration

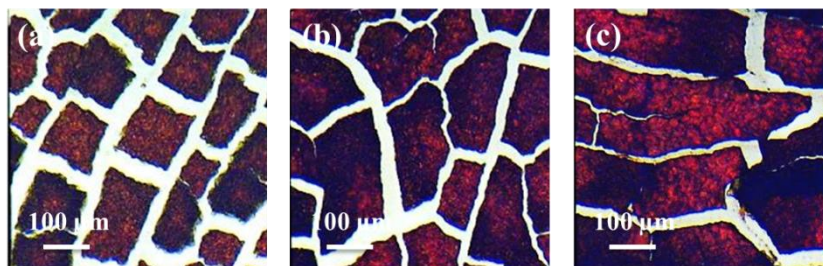


Figure 4.9: Microscope pictures of Ga_2O_3 inverse opal: precursor prepared with 30 wt% gallium nitrate (a), 40 wt% gallium nitrate (b) and 50 wt% gallium nitrate (c)

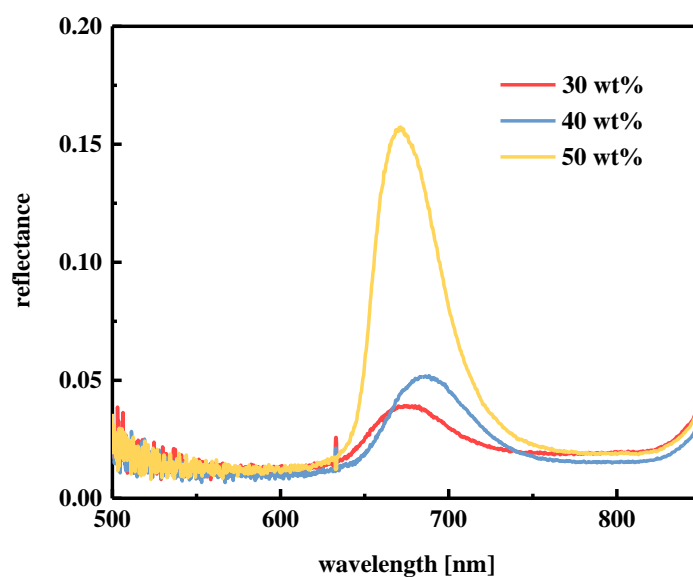


Figure 4.10: FTIR spectra of Ga_2O_3 inverse opal: precursor prepared with different gallium nitrate concentration

To study the impact of precursor concentration on the optical property of the resulting inverse opals, 30 wt%, 40 wt% and 50 wt% gallium nitrate ethanol solution were applied to form Ga_2O_3 inverse opals respectively. Figure 4.9 shows the microscope pictures of the resulting Ga_2O_3 inverse opals. All the samples display red opalescence and the opalescence becomes brighter as precursor concentration increases. It is also observed that the inverse opal prepared with 50 wt% precursor concentration exhibit the smallest crack area. The corresponding FTIR spectra (Figure 4.10) show the similar result, where the reflectance increases with increasing precursor concentration.

At lower concentration the precursor material did not fill the void space of PMMA template completely, resulting in numerous vacancies in precursor network and large crack area (owing to volume shrinkage) in the final inverse opal structure. In this work, 60 wt% gallium nitrates were also tested to fabricate Ga_2O_3 inverse opal. However, this higher precursor concentration made the precursor solution too viscous to penetrate the PMMA opal completely and the resulting inverse opals did not show strong opalescence.

drying condition

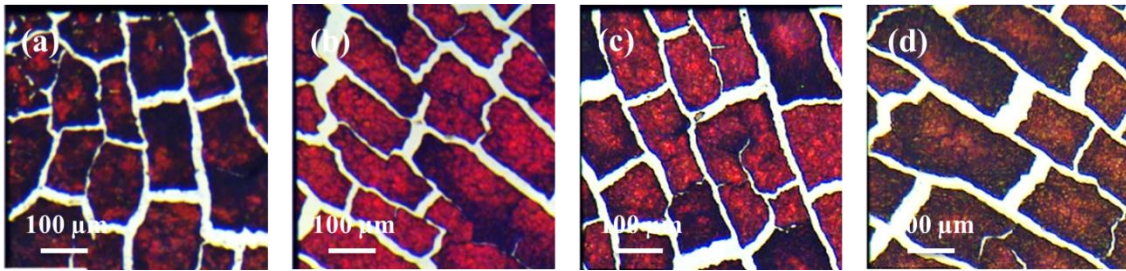


Figure 4.11: Microscope pictures of Ga₂O₃ inverse opal: after infiltration sample dried at room temperature (a), 40 °C (b), 60 °C (c) and 80 °C (d)

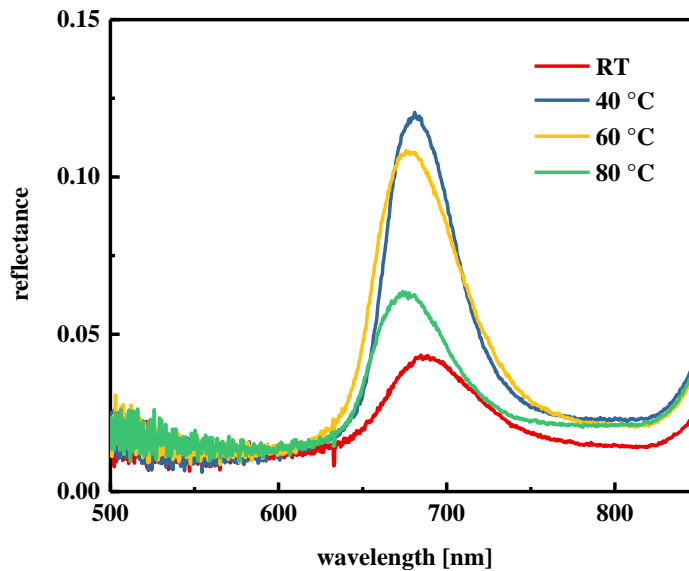


Figure 4.12: FTIR spectra of Ga₂O₃ inverse opal: precursor prepared with different drying temperature

The removal of precursor solvent from the void spaces of PMMA opal is also an important step for forming highly ordered macroporous structure [100]. To investigate this process, after infiltration with 50 wt% gallium nitrate precursor solution the composite sample was dried for 24 h at room temperature, 40 °C, 60 °C and 80 °C respectively. Figure 4.11 shows the microscope pictures of resulting inverse opals. It is obvious that the sample dried at 40 °C and 60 °C has stronger red opalescence than the samples dried at room temperature or 80 °C. The corresponding FTIR spectra (Figure 4.12) reveal that the peak position remains the same for all inverse opals. But the maximum reflectance of the sample dried at 40 °C and 60 °C are higher than the others.

The residual solvent can form gas bubbles during thermal conversion process which creates pressure in the opal pores and reduce the contact between precursor material and template spheres. Meanwhile, the evaporation processes should be carried out under mild condition to avoid premature damage of the regular arrangement of the PMMA spheres. In the synthesis of Ga_2O_3 inverse opal, it could be concluded that drying at $40\text{ }^\circ\text{C}$ to $60\text{ }^\circ\text{C}$ appeared to be most appropriate for completely removing ethanol solvent without destroying the order of PMMA spheres.

Thermal conversion temperature

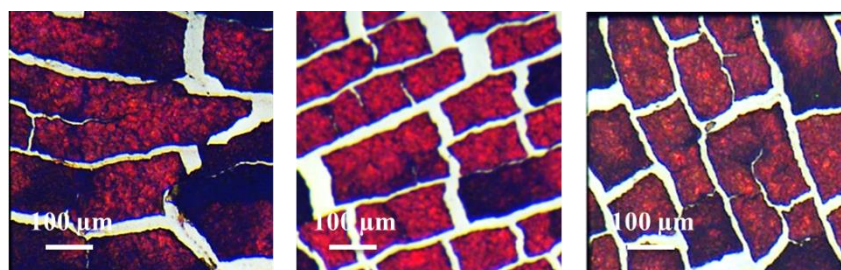


Figure 4.13: Microscope pictures of Ga_2O_3 inverse opal: calcined at $350\text{ }^\circ\text{C}$ (left), $450\text{ }^\circ\text{C}$ (middle) and $550\text{ }^\circ\text{C}$ (right)

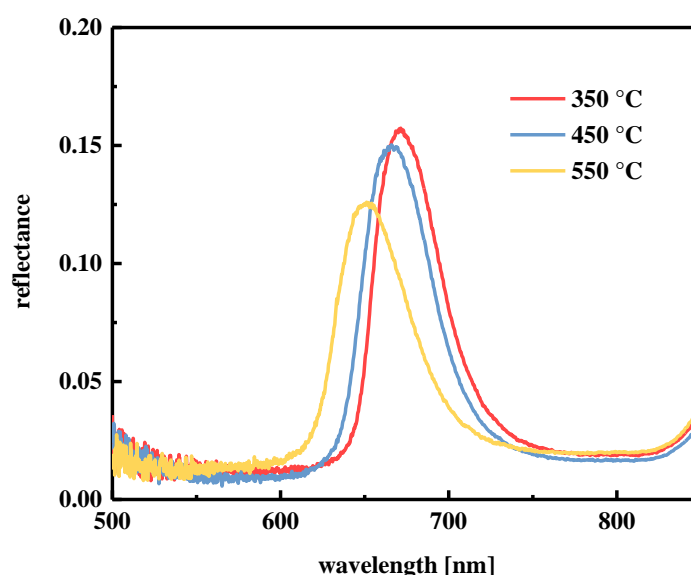


Figure 4.14: FTIR spectra of Ga_2O_3 inverse opal: calcined at different temperature

Thermal conversion process also play important role in the inverse opal synthesis. Figure 4.13 shows the microscope pictures of Ga_2O_3 inverse opal calcined at $350\text{ }^\circ\text{C}$, $450\text{ }^\circ\text{C}$ and $550\text{ }^\circ\text{C}$ respectively. All the inverse opal display strong red opalescence. In the corresponding

reflectance spectra, peak maximum slightly decrease and shift to lower wavelength with increasing calcination temperature. This can be explained by larger structure shrinkage (lead to smaller pore diameters) at higher calcination temperature.

Following criteria of final optical quality of the Ga_2O_3 inverse opals, 50 wt% gallium nitrate ethanol solution, drying at 40 °C for 24 h and calcination at 350 °C were selected as the most appropriate synthesis parameters. The optical data of the corresponding inverse opal are summarized in Figure 4.15. In the SEM image, well-ordered macroporous structure can be observed and the average center-to-center distance between two neighboring pores was determined to 406 ± 5 nm, which was 19 % smaller than the diameters of the original PMMA spheres. The measured reflection spectra exhibit well defined peak with the maximum reflectance located at 671 nm, which is consistent with the red color appearance in the corresponding photograph.

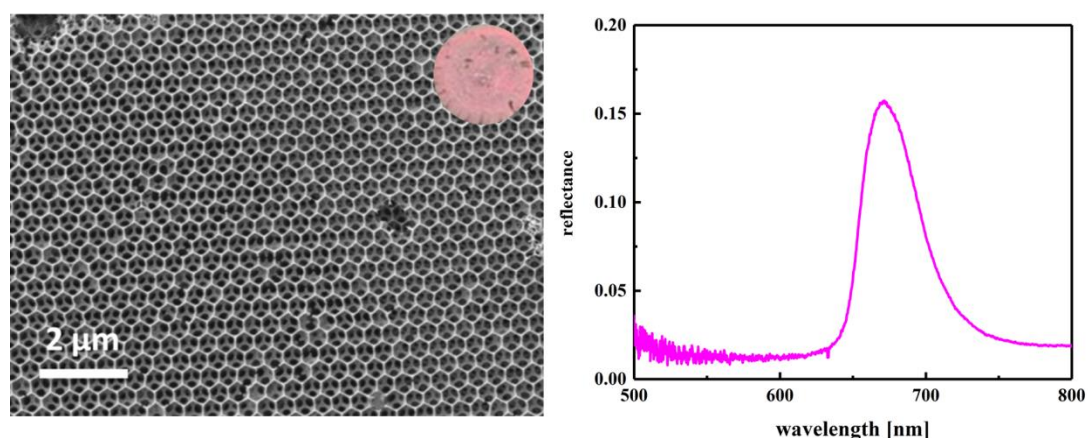


Figure 4.15: SEM image (left) and FTIR spectrum (right) of Ga_2O_3 inverse opal. Insets: photograph of corresponding Ga_2O_3 inverse opal

Similar to the synthesis of Ga_2O_3 inverse opal, the synthesis conditions for other metal oxide inverse opals were also optimized systemically. PMMA opals with template spheres of 502 nm were applied as structure template. The optical data of the inverse opals with the best quality (highest reflectance) will be presented.

4.2.1.2 Cr_2O_3

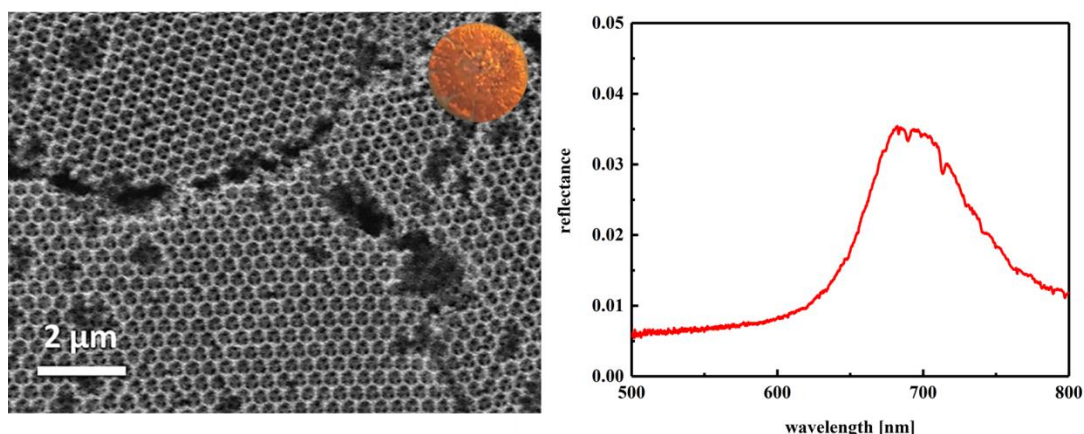


Figure 4.16: SEM image (left) and FTIR spectrum (right) of Cr_2O_3 inverse opal. Insets: photograph of corresponding Cr_2O_3 inverse opal

In the synthesis of Cr_2O_3 inverse opal, 40 wt% chromium nitrate ethanol solution, drying at room temperature for 24 h and calcination at 350 $^\circ\text{C}$ were chosen as the most suitable synthesis conditions. Figure 4.16 shows the corresponding optical data. It can be seen that, the resulting inverse opal exhibits highly ordered macroporous structure with pore diameter about 372 ± 7 nm. Due to volume shrinkage during calcination process, the final pore size is 26 % smaller compared to the 502 nm template spheres. The reflection maximum is located at 690 nm and the sample displays red color in its corresponding photograph.

4.2.1.3 Fe_2O_3

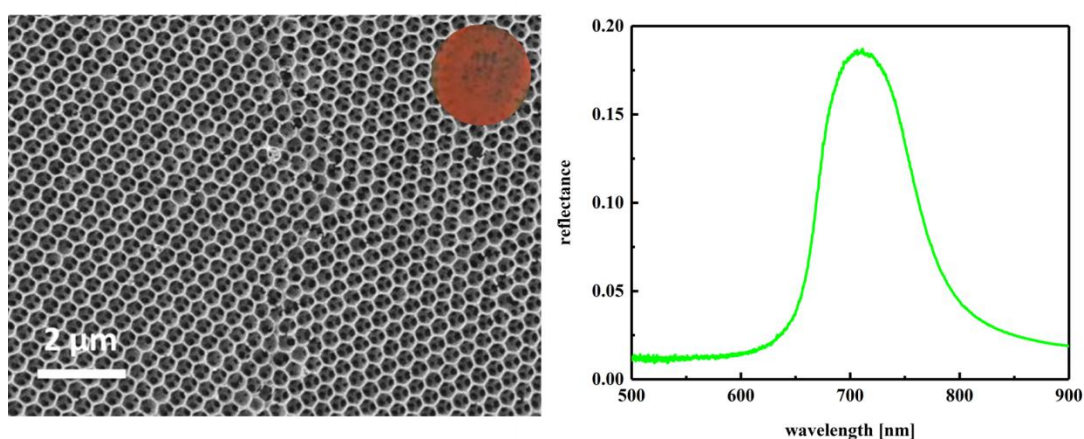


Figure 4.17: SEM image (left) and FTIR spectrum (right) of Fe_2O_3 inverse opal. Insets: photograph of corresponding Fe_2O_3 inverse opal

For fabricating Fe_2O_3 inverse opal, 50 wt% iron nitrate ethanol solution, drying at room temperature for 24 h and calcination at 350 °C were used as the optimized synthesis conditions. The corresponding SEM image (Figure 4.17 left) reveals a well-ordered porous structure with pore diameter about 385 ± 8 nm. In the FTIR spectrum (Figure 4.17 right), the band gap position (reflection maximum) is located around 690 nm, which is within the range of the reflected wavelength of red light.

4.2.1.4 In_2O_3

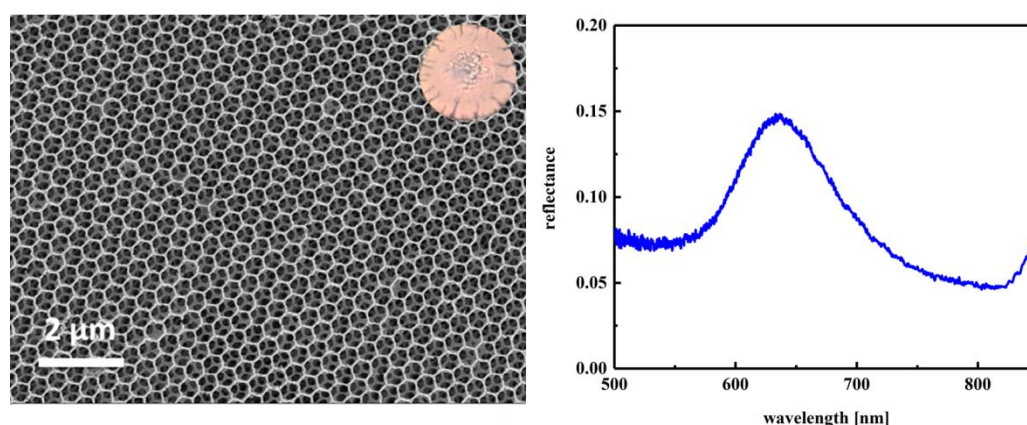


Figure 4.18: SEM image (left) and FTIR spectrum (right) of In_2O_3 inverse opal. Insets: photograph of corresponding In_2O_3 inverse opal

In the synthesis of In_2O_3 inverse opal, 30 wt% indium nitrate ethanol solution, drying at room temperature for 24 h followed by drying at 60 °C for 72 h and calcination at 350 °C were applied to fabricate In_2O_3 inverse opal with highest reflectance. The corresponding optical data are shown in Figure 4.18. It is observed that, the resulting inverse opal exhibit well-ordered macroporous structure. The pore diameter is determined to 400 ± 8 nm, which is 20 % smaller than the 502 nm PMMA spheres used for the template. The sample displays red opalescence in its photograph and the measured reflection peak has maximum reflectance at 636 nm.

4.2.1.5 *CeO₂, CuO and ZnO*

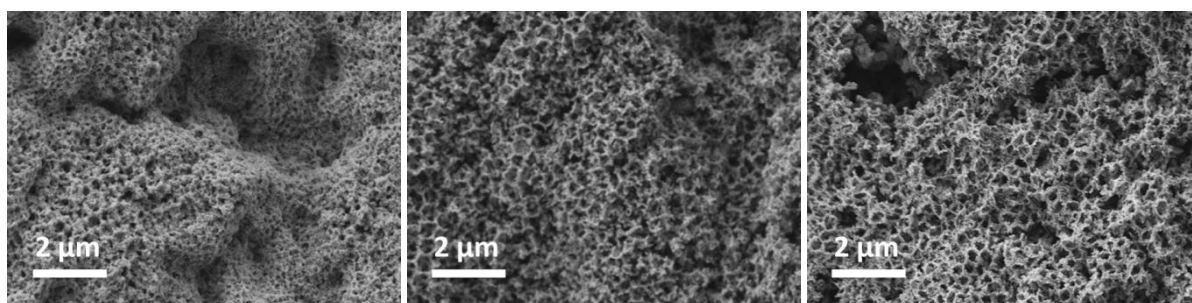


Figure 4.19: SEM images of CeO₂ (left), CuO (middle), and ZnO (right) films which are prepared with respective metal nitrate precursors

As shown in Figure 4.19, in regard to the synthesis of CeO₂, CuO and ZnO, only disordered macroporous films were formed employing the corresponding metal nitrates as precursors. Their structure order could not be improved by changing the precursor concentration, drying and calcination condition. The absence of ordered microstructure results into the loss of colors compared to the other above-mentioned metal oxides inverse opals. As the metal nitrate precursors are subjected to similar infiltration and drying procedure and no drastic changes of materials are expected in these two processes, the poor optical quality of CeO₂, CuO and ZnO is probably related to the interplay of mechanical stability of PMMA template and the nitrate precursors during thermal conversion process. One hypothesis for the formation of disordered macroporous metal oxides can be that, the onset temperature for the phase transformation from the soft metal nitrate melts into rigid metal oxide solids is higher than the temperature required for PMMA glass transition and decomposition, and consequently leading to the absence of rigid building blocks for the formation of ordered network of metal oxides.

4.2.1.6 *Thermal behavior of PMMA particles and respective metal nitrates*

In order to verify the hypothesis, differential scanning calorimetry (DSC) and coupled thermogravimetric analysis - mass spectroscopy (TGA-MS) were performed for both metal nitrate salts and PMMA template particles.

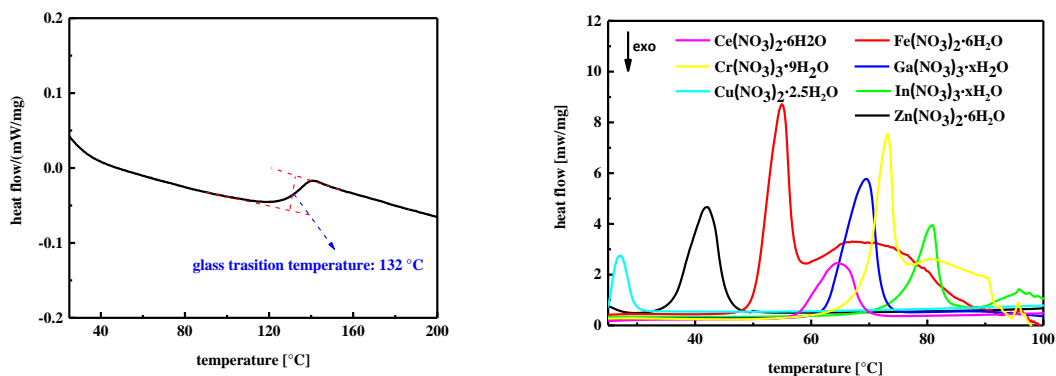


Figure 4.20: Differential scanning calorimetry (DSC) results of PMMA spheres (left) and pure metal nitrate salts (right)

Figure 4.20 shows DSC results of 502 nm PMMA spheres and pure metal nitrate salts. A single glass transition temperature (T_g) at 132 °C can be found in the left DSC thermogram. The glass transition temperature was determined as the temperature at the inflection point of the change in heat flow. In the right DSC thermogram, each metal nitrate salts exhibits an endotherm peak below 100 °C. This confirms that, melting and/or dehydration process occurs at a relative lower temperature for all the metal nitrate salts, making their precursor network unstable among adjacent PMMA voids.

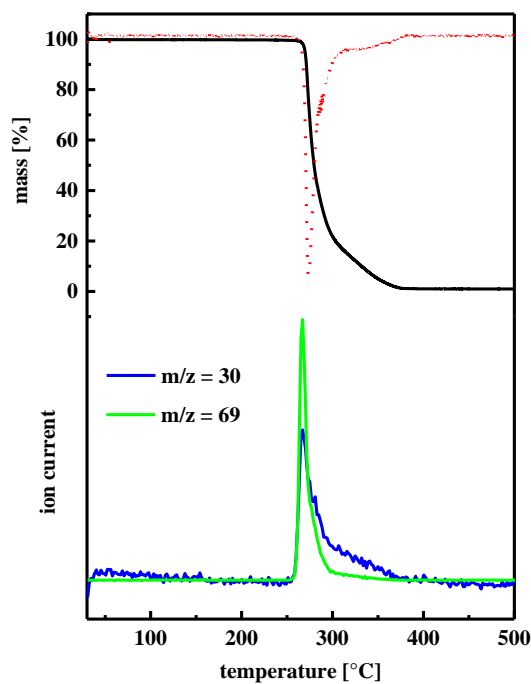


Figure 4.21: Thermogravimetric/derivative thermogravimetry (TG/DTG, top) and mass spectrometry (MS, bottom) results of PMMA templates

As shown in Figure 4.21, the thermal decomposition of PMMA particles used to form structure template occurs in the temperature range of *ca.* 260 °C to 350 °C, featured by the corresponding complete mass loss in TG curve (black line in Figure 4.21), which is more clearly depicted by the first derivative curve (DTG, red line in Figure 4.21). The mass loss is confirmed by coupled MS to be caused by PMMA decomposition, revealing fragments of $C_4H_5O^+$ cations ($m/z = 69$, green line in Figure 4.21) at 260 °C. In addition, fragment of $m/z = 30$ also presented in the MS profile at the same temperature range, implying CH_2O^+ cation or the existence of impurities in the synthesized PMMA particles.

Since $m/z = 30$ (NO^+) is a characterized signature for metal nitrate conversion, it is important to investigate the composition of the PMMA particles to prevent the influence of any impurities on the subsequent determination of nitrate conversion temperature. For this purpose, infrared spectroscopy and elementary analyses were performed on the synthesized PMMA particles.

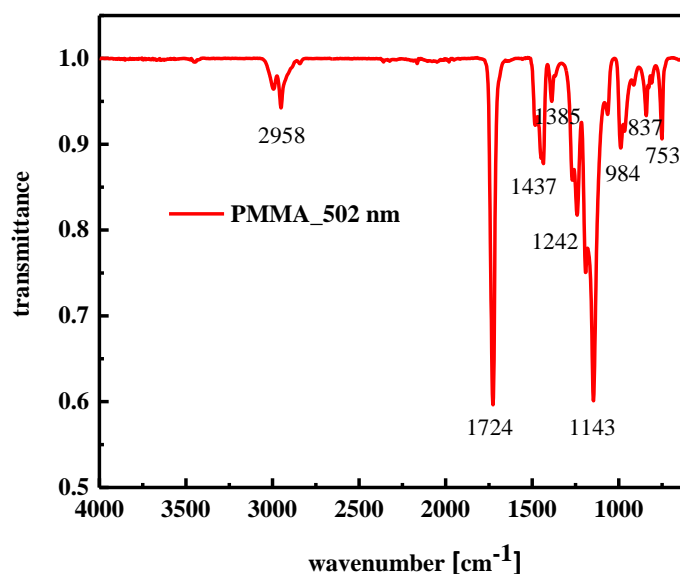


Figure 4.22: Transmittance spectrum of synthesized PMMA particles

Figure 4.22 shows the transmittance spectrum of the PMMA spheres used to grow colloidal crystals. The two bands at 837 cm^{-1} and 984 cm^{-1} are the characteristic absorption vibrations of PMMA [101]. There are two distinct absorption bands at 1143 cm^{-1} and 1242 cm^{-1} , which belong to the C–O–C stretching vibration. The bands at 753 cm^{-1} and 1385 cm^{-1} can be ascribed to the methyl group vibrations. The strong band appearing at 1724 cm^{-1} show the presence of carboxyl (C=O) group. The band at 1437 cm^{-1} can be assigned to the bending

vibration of the C–H bonds in CH₃ group and the band at 2958 cm⁻¹ is related to the stretching vibration of the C–H bonds in CH₂ group. No other distinct band is observed in the corresponding transmittance spectrum, which indicates that the prepared polymer particle was actually pure PMMA particles.

Furthermore, according to the result from elementary analyses no nitrogen compound can be detected in the synthesized PMMA particles. Therefore it can be concluded that the peak of $m/z = 30$ (blue line in Figure 4.21) is belong to the CH₂O⁺ cation rather than other fragments associated with nitrogen.

The nitrate conversion temperature for each PMMA-metal nitrate composite system was then analyzed by TGA-MS coupling. The results are shown in Figure 4.23 to Figure 4.26.

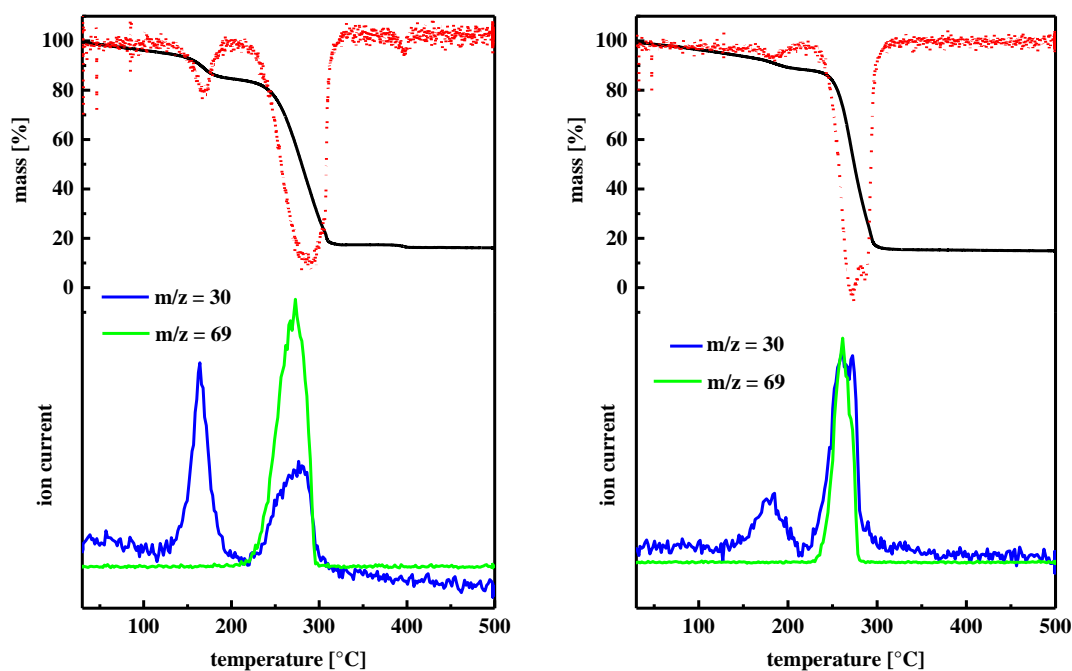


Figure 4.23: Thermogravimetric/derivative thermogravimetry (TG/DTG) and mass spectrometry (MS) results of PMMA-Cr(NO₃)₃·9H₂O-composite (left) and PMMA-Fe(NO₃)₃·6H₂O-composite (right)

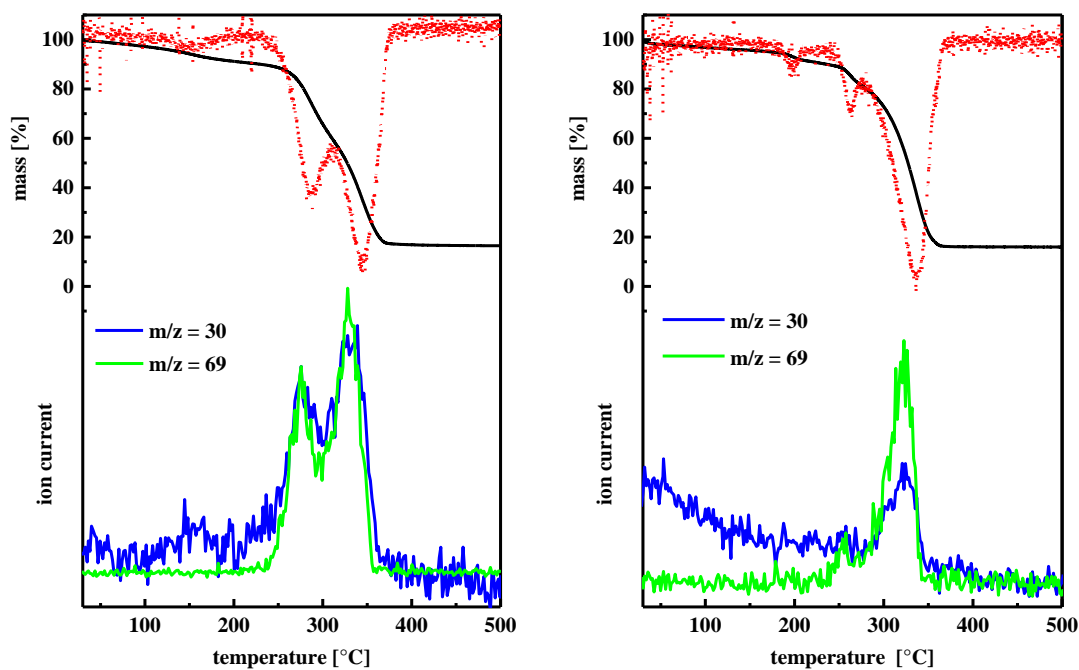


Figure 4.24: Thermogravimetric/derivative thermogravimetry (TG/DTG) and mass spectrometry (MS) results of PMMA-Ga(NO₃)₃·xH₂O-composite (left) and PMMA-In(NO₃)₃·xH₂O-composite (right)

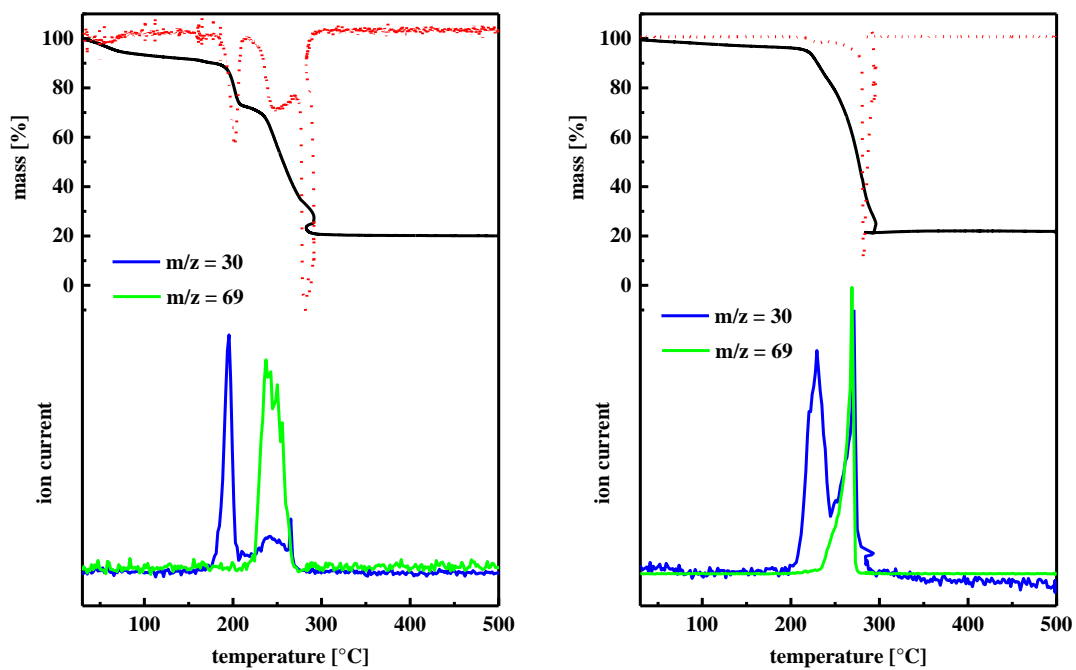


Figure 4.25: Thermogravimetric/derivative thermogravimetry (TG/DTG) and mass spectrometry (MS) results of PMMA-Ce(NO₃)₂·6H₂O-composite (left), PMMA-Cu(NO₃)₂·2.5H₂O-composite (right)

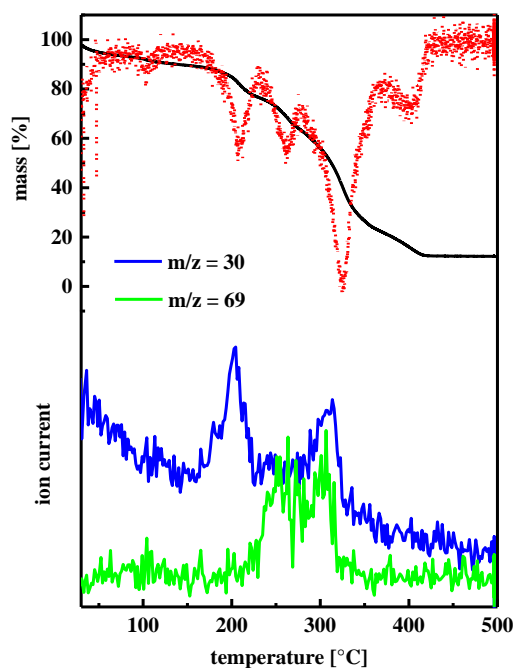


Figure 4.26: Thermogravimetric/derivative thermogravimetry (TG/DTG) and mass spectrometry (MS) results of PMMA-Zn(NO₃)₂·6H₂O-composite

To explain the nitrate conversion process in the composite material, the TGA-MS result of PMMA template after infiltration of Cr(NO₃)₃·9H₂O (Figure 4.23 left) is discussed in detail. Compared to the results of pure PMMA particles, an additional mass loss occurs at about 122 °C for PMMA-Cr(NO₃)₃·9H₂O-composite. Around the same temperature, the MS results show a signature of ¹⁴N¹⁶O⁺ cation (m/z = 30, blue line in Figure 4.23 left) indicating the conversion process from metal nitrate into metal oxides. Another signal of m/z = 30 is also observed at a higher temperature around 230 °C, accompanied by the detection of the C₄H₅O⁺ cation (m/z = 69, green line in Figure 4.23 left), which is attributable to the second mass loss for PMMA decomposition.

The other composite materials show similar decomposition behaviour. The onset temperatures for the decomposition of metal nitrates (i.e. formation of metal oxides) in the respective PMMA-metal nitrate composites are summarized in Table 4.3.

For PMMA-In(NO₃)₃·xH₂O composite, the nitrate conversion process cannot be observed from the corresponding mass spectroscopy. But according to the results of previous literature [100], in the same composite material the onset conversion temperature of indium nitrate should be around 190 °C. In addition, strong catalytic effects to the PMMA decomposition are observed for the oxides of redox-active metals (Cr, Fe, Ce, Cu). The PMMA spheres in the

corresponding composites were decomposed at a relatively lower temperature compared to the decomposition temperature in the pure states. Similar results were also found in other metal nitrate-impregnated materials [101, 102].

Table 4.3: Onset temperature of nitrate conversion and PMMA decomposition in the composite material

Composite	Onset temperature of nitrate conversion (°C)	Onset temperature of PMMA decomposition (°C)
PMMA-Cr(NO ₃) ₃ ·9H ₂ O	122	230
PMMA-Fe(NO ₃) ₃ ·6H ₂ O	132	227
PMMA-Ga(NO ₃) ₃ ·xH ₂ O	118	285
PMMA-In(NO ₃) ₃ ·xH ₂ O	190 ^[100]	278
PMMA-Ce(NO ₃) ₂ ·6H ₂ O	175	216
PMMA-Cu(NO ₃) ₂ ·2.5H ₂ O	205	232
PMMA-Zn(NO ₃) ₂ ·6H ₂ O	166	255

According to the experimental results, the conversion temperature was lower for all the metal nitrates in comparison to PMMA decomposition temperature (Table 4.3). Therefore, the observed structure quality difference for different metal oxides was not caused by the lower onset precursor conversion temperature than the PMMA decomposition.

Ruling out decomposition temperature, the onset temperature of metal oxide formation was then compared with the glass transition temperature of PMMA. During glass transition, the mechanical strength of PMMA templates evolve from rigid to soft along with the rising temperature. As suggested by experimental results, for nitrate precursors with lower or approximate conversion temperatures compared to PMMA glass transition, ordered metal oxide structures were formed (e.g. Cr₂O₃, Ga₂O₃, and Fe₂O₃), otherwise, disordered structures were obtained (e.g. CeO₂, CuO and ZnO). Therefore, the formation of disordered structures of CeO₂, CuO and ZnO films was due to the absence of a rigid PMMA template caused by the occurrence of PMMA glass transition before metal nitrate conversion. Further investigation into the formation of Cr₂O₃, Ga₂O₃ and Fe₂O₃ suggests that the corresponding nitrate precursors form hydroxynitrates (Me(OH)_x(NO₃)_{3-x}) initially during metal nitrate conversion

[103-105]. The ionic-covalent character of the Me-OH bond interacts with the carbonyl groups in PMMA, which can reduce the mobility of PMMA chains and prevent the separation between the template spheres and precursor networks.

Unlike other successfully synthesized metal oxide inverse opals, In_2O_3 displaying an ordered structure but with a higher nitrate conversion temperature (see Table 4.3). For indium nitrate conversion, instead of hydroxynitrate is $\text{In}(\text{OH})_3$ the initial state [106], and is likely to be formed already during the drying process of indium nitrate (see Table 3.2). This is consistent with the TGA-MS result of $\text{PMMA-In}(\text{NO}_3)_3 \cdot x\text{H}_2\text{O}$ (Figure 4.24 right), suggesting the absence of NO^+ fragment. The subsequent formation of In_2O_3 from $\text{In}(\text{OH})_3$ proceeds via solid-solid phase transformation [106], which ensures a rigid precursor network during calcination and lead to the formation of In_2O_3 with ordered structure.

Therefore, either a rigid intermediate from the precursor or a lower conversion temperature compared to that of PMMA glass transition is required to retain a rigid network for the fabrication of highly ordered metal oxide inverse opal structure. Based on this idea, improvement of the precursor network stability was attempted for CeO_2 , CuO and ZnO via three precursor modification strategies including organic chelating method, polymerization of TEOS and polyacrylamide gelation method.

4.2.2 Modified metal nitrate as precursors

4.2.2.1 Organic chelating method

Organic chelating has been reported previously for the synthesis of metal oxide inverse opals. [107-110]. With the potential of forming highly thermostable metal citrates via reactions with metal nitrates, citric acid was employed as a chelating agent for the fabrication of CeO_2 , CuO and ZnO inverse opals (Figure 4.27).

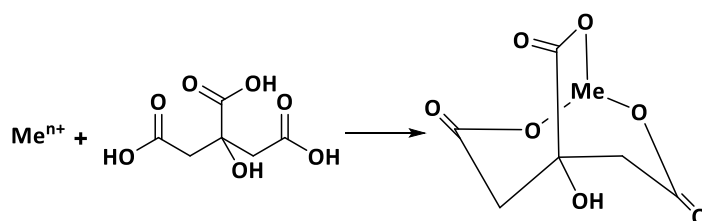


Figure 4.27: Reaction of metal cation with citric acid

Metal citrates are very soluble in ethanol, and the corresponding solution can be infiltrated directly into PMMA templates. After solvent evaporation, the solid metal citrates decompose into metal oxides without melting process [110]. Thanks to the rigid metal citrate networks, well-ordered porous structures were obtained for CeO_2 and CuO inverse opals (Figure 4.28 and 4.29), which were not possible to synthesize by using pure metal nitrate as precursors (Figure 4.19).

CeO_2

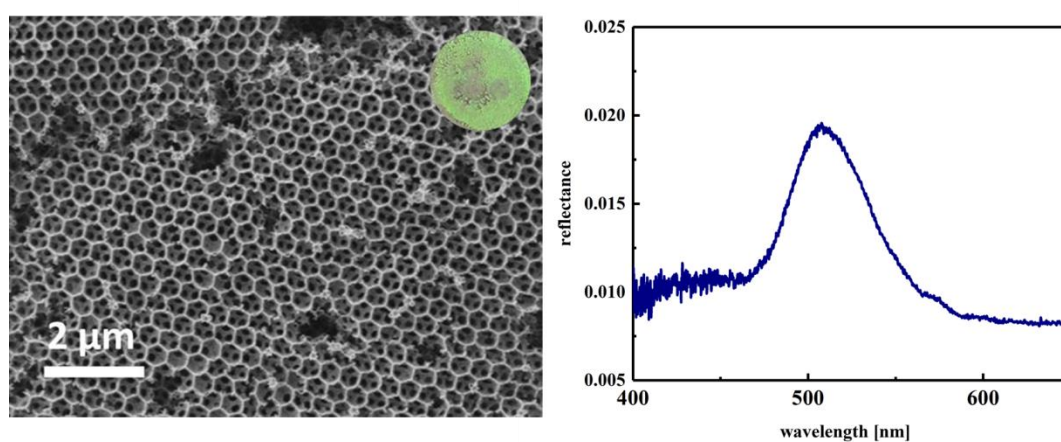


Figure 4.28: SEM image (left) and FTIR spectrum (right) of CeO_2 inverse opal. Insets: photograph of corresponding CeO_2 inverse opal

Figure 4.28 shows the optical data of CeO_2 inverse opal which was synthesized based on organic chelating with citric acid. The resulting inverse opal exhibits highly ordered macroporous structure with pore diameter about 372 ± 9 nm. The corresponding shrinkage in diameter is 26 %. The measured reflection maximum located at 515 nm, which is consistent with the green color appearance in the inset photograph.

CuO

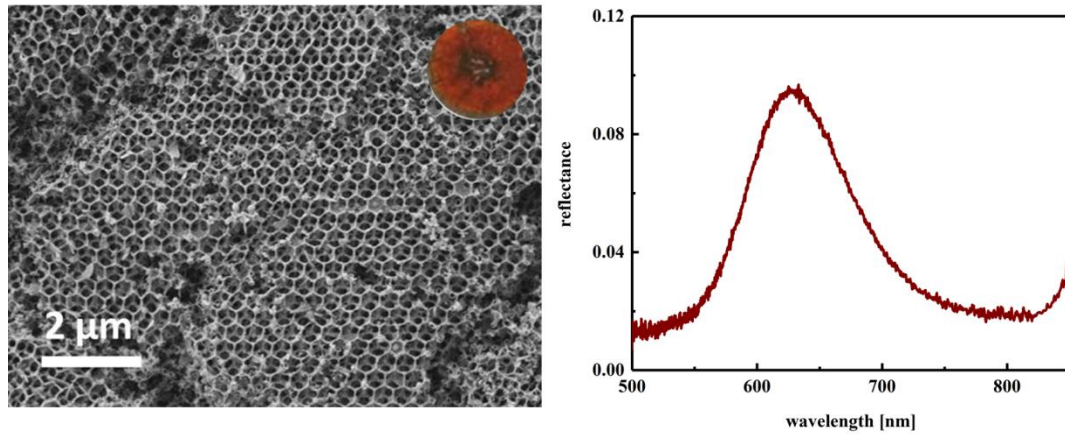


Figure 4.29: SEM image (left) and FTIR spectrum (right) of CuO inverse opal. Insets: photograph of corresponding CuO inverse opal

Figure 4.29 shows the SEM and FTIR results of CuO inverse opal which was fabricated with organic chelating method. The SEM image reveals highly ordered porous structure. The spherical pore size of CuO inverse opal is 355 ± 13 nm, which is 29 % smaller than PMMA spheres used to crystalize opal templates. The CuO inverse opal display red opalescence, which correspond to the measured reflection peaks centered at 627 nm.

ZnO

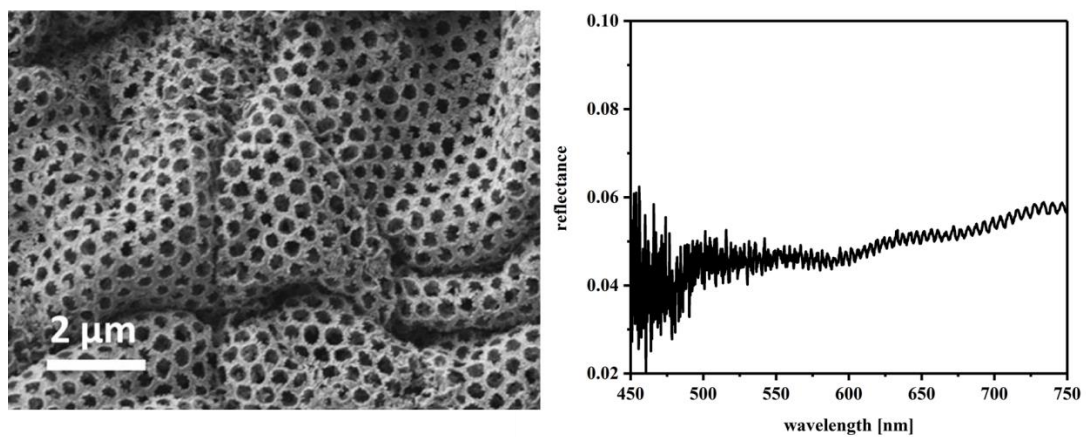


Figure 4.30: SEM image (left) and FTIR spectrum (right) of ZnO film

Compared to CeO₂ and CuO inverse opals, ZnO samples prepared with citric acid only show deformed porous structures (Figure 4.30 left), and consequently, the resulting film does not show optical reflectance in the corresponding FTIR spectrum.

This can be explained by the higher conversion temperature of zinc citrate. Figure 4.31 depicts the three TGA-MS curves of PMMA templates after infiltration of respective metal citrate. In the thermogram CO₂⁺ (m/z = 44) was chosen as characterized signature to investigate the citrate conversion process. It should be mentioned that, in our case the signature of CO₂⁺ is related to both PMMA decomposition and citrate conversion, so the signature of C₄H₅O⁺ (m/z = 69, CH₂=C(CH₃)CO⁺) was also shown as reference of PMMA decomposition [111, 112]. It can be seen that, a strong signature of CO₂⁺ corresponding to the conversion of zinc citrate occurs at around 350 °C for PMMA–zinc citrate-composite (pink line in Figure 4.31 right). Unlike other two composite materials, the conversion temperature of zinc citrate is higher than the decomposition temperature of PMMA (observed by the detection of C₄H₅O⁺, green line in Figure 4.31 right). Zinc citrate was converted into zinc oxide after the decomposition of PMMA, resulting in a conversion without template support and increasing the possibility to form deformed porous structures.

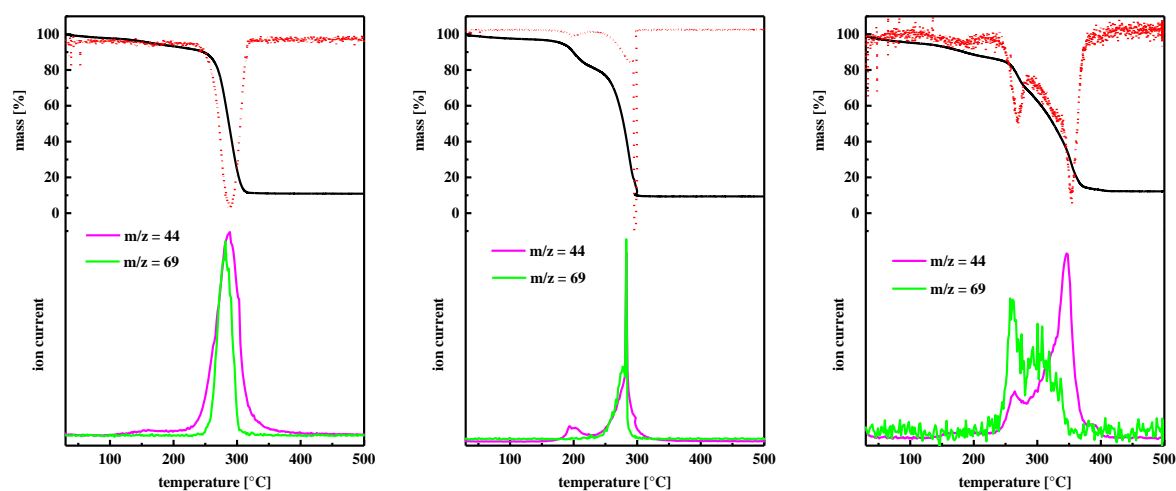


Figure 4.31: Thermogravimetric/derivative thermogravimetry (TG / DTG) and mass spectrometry (MS) results of PMMA-cerium citrate-composite (left), PMMA-cooper citrate-composite (middle) and PMMA-zinc citrate-composite (right)

4.2.2.2 *Polymerization of TEOS*

To synthesize ZnO inverse opals, zinc citrate was strengthened with TEOS to further enhance the mechanical rigidity of the precursor network. The structure of TEOS contains four alkoxy groups, leaving an orthosilicate product after hydrolysis in precursor solution. The orthosilicate then interacts with Zn ions, forming Si-O-Zn bonds (Figure 4.32), which stabilized the precursor network during calcination [113].

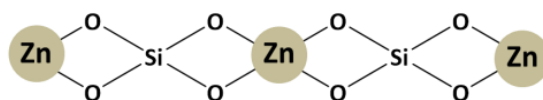


Figure 4.32: Schema of the ZnO-SiO₂ intramolecular network

Additionally, the hydrophobicity of the precursor is enhanced with the presence of TEOS, leading to a more uniform wetting of PMMA during infiltration, and thereby, a better control of precursor loading. If the amount of TEOS reaches 1 vol%, opalescent colors and high optical reflectance are observed (Figure 4.33). In the corresponding SEM image the ZnO-SiO₂ inverse opal exhibits a well-ordered porous structure with pore size around 405±9 nm.

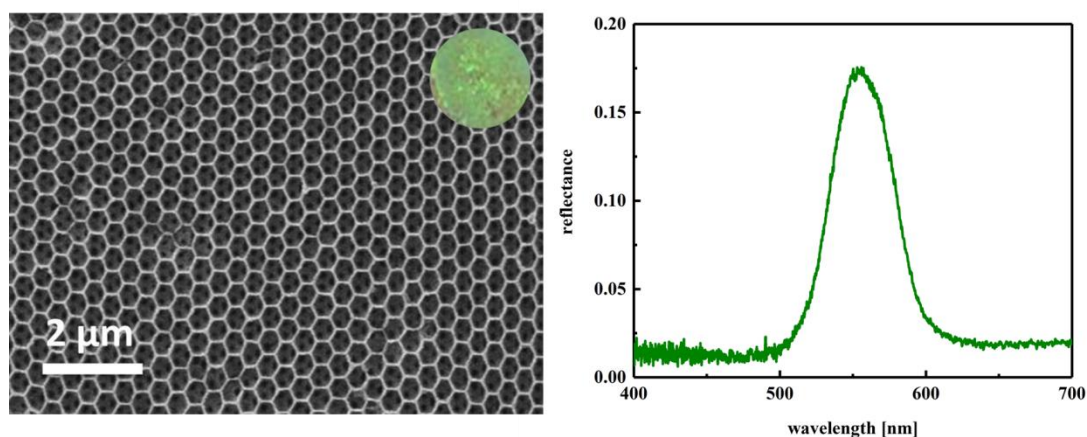


Figure 4.33: SEM image (left) and FTIR spectrum (right) of ZnO-SiO₂ inverse opal. Insets: photograph of corresponding ZnO-SiO₂ inverse opal

Another advantage of this method is that, the SiO₂ originated from TEOS modifies the effective refractive index of the inverse opals, which can be used to adjust its photonic band gap to a desired spectral region.

4.2.2.3 Polyacrylamide gelation method

In addition, polyacrylamide gelation method was also applied to synthesize ZnO inverse opal. Polyacrylamide gelation refers to in-situ formation of a solid polymer resin in PMMA template voids [114]. The PMMA template was infiltrated by a mixture comprising acrylamide (monomer), bis-acrylamide (cross linker) and zinc nitrate. Upon heating, acrylamide polymerization occurs among adjacent PMMA voids, forming a homogeneous solid polymeric network containing evenly dispersed zinc ions [115].

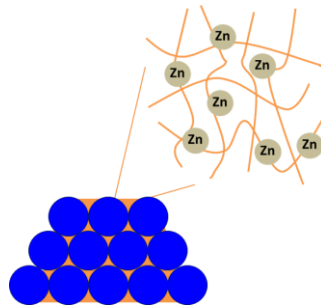


Figure 4.34: Shema of infiltrated PMMA opal after polyacrylamide gelation

Possessing a considerably higher decomposition temperature than that of PMMA glass transition and decomposition [116], polyacrylamide resin acts as a rigid solid support for metal nitrate conversion during PMMA removal, leading to the successful fabrication of ZnO inverse opals with long-range order macropores (Figure 4.35 left). Despite the more irregular shape of individual pores in comparison to the inverse opals formed from TEOS-containing precursors (Figure 4.33), the ZnO inverse opals still display strong structure colors with relatively high reflectance (Figure 4.35 right).

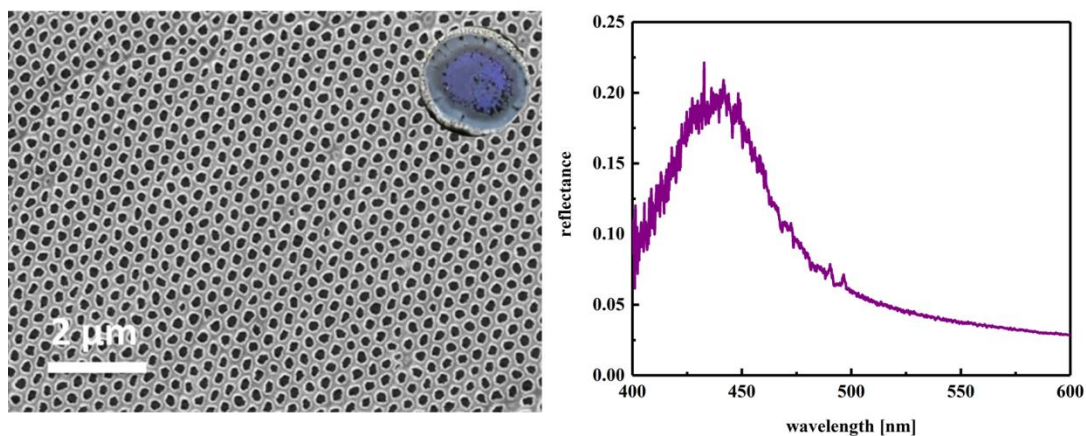


Figure 4.35: SEM image (left) and FTIR spectrum (right) of ZnO-Acrylamide inverse opal. Insets: photograph of corresponding ZnO-Acrylamide inverse opal

In summary, these three modification methods including organic chelating, polymerization of TEOS and polyacrylamide gelation followed the same strategy that improve the mechanical strength of the precursor network to avoid collapse or deformation during glass transition and decomposition process of the polymer templates. As a result, CeO₂, CuO and ZnO inverse opals with long range orders and vivid structural colors were obtained.

4.2.3 *Metal oxide nanoparticles as precursors*

Using metal nitrates as precursors have brought several advantages because of their high solubility and low reactivity. However, the samples prepared with metal nitrates usually exhibit defects and cracks. This can be explained by the volume shrinkage caused by the density change from the nitrate precursor to the respective oxide. For example, in case of the synthesis of Fe₂O₃ inverse opal, the density of iron nitrate (1.68 g·cm⁻³) is substantially lower than that of the resultant Fe₂O₃ (5.24 g·cm⁻³) after the oxide formation [117].

In this present work, apart from metal nitrates, nanoparticles of desired oxide were also applied to fill the voids of PMMA template with the goal to reduce crack formation and fabricate higher quality inverse opals.

4.2.3.1 *SnO₂*

For this purpose, SnO₂ inverse opal was synthesized using aqueous SnCl₄ solution. SnCl₄ is mostly hydrolyzed in water; leading to the formation of colloidal SnO₂ nanoparticles (see Equation 4.2).



In order to increase the penetration through PMMA template small amount ethanol was also added in the precursor solution (see section 3.2.3). The precursor was then applied to fill the voids of PMMA template. After removal of template spheres SnO₂ inverse opal was obtained. The optical property of the corresponding inverse opal was characterized with SEM and FTIR and the results are shown in Figure 4.36.

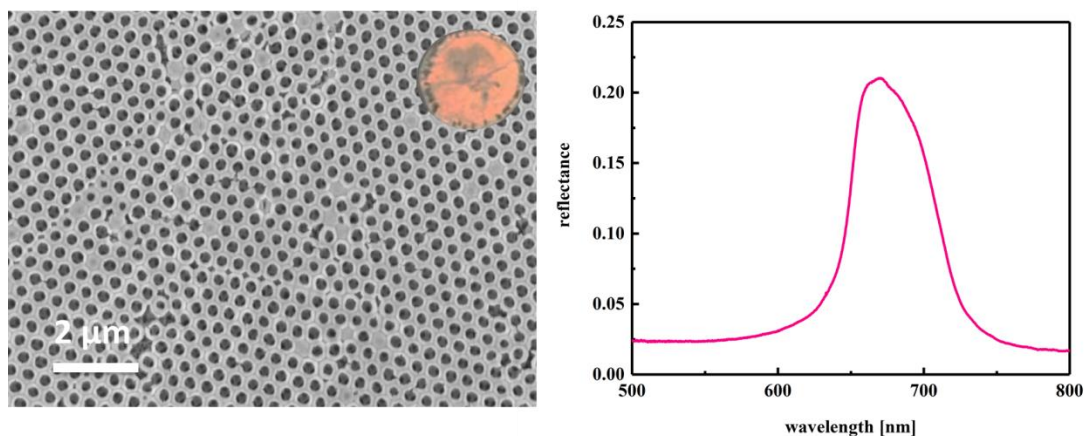
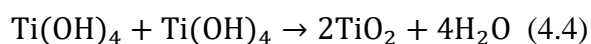
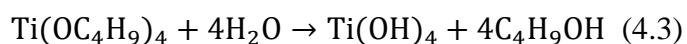


Figure 4.36: SEM image (left) and FTIR spectrum (right) of SnO₂ inverse opal. Insets: photograph of corresponding SnO₂ inverse opal

In the SEM image, well-ordered macroporous structure can be observed and the average pore size was determined to 430±6 nm, which was 15 % smaller than the diameters of the original PMMA spheres. The shrinkage in diameter is smaller than the samples prepared with nitrate precursor (between 19 % and 29 %). In the reflection spectrum, the peak maximum located at 672 nm, which correspond to the red opalescent displayed in its photograph.

4.2.3.2 *TiO₂*

Similar strategy was also applied to fabricate TiO₂ inverse opal. Titanium(IV) butoxide (Ti(OC₄H₉)₄) served as precursor material. Ti(OC₄H₉)₄ undergoes strong hydrolysis and condensation process in aqueous solution, forming colloidal TiO₂ nanoparticles (see Equation 4.3 and 4.4).



The formation of ordered inverse opal structure becomes more difficult, if this alkoxide hydrolyze too rapidly to fill the PMMA template completely. In that case bulk titania is easily formed on the template surface and blocking additional precursor material going into the void spaces [118]. Therefore Ti(OC₄H₉)₄ was dissolved in ethanol to decrease the rates of hydrolysis. Furthermore, the addition of acid (e.g. HCl) was also important to infiltrate PMMA template completely, because Ti(OC₄H₉)₄ are very viscous and its solubility in

ethanol is higher at low pH values. Addition of an acid also decreased the reactivity of the alkoxide, preventing premature TiO_2 nanoparticles aggregate during the infiltration process [119]. Using these controlled conditions, well-ordered TiO_2 inverse opal was obtained (Figure 4.37).

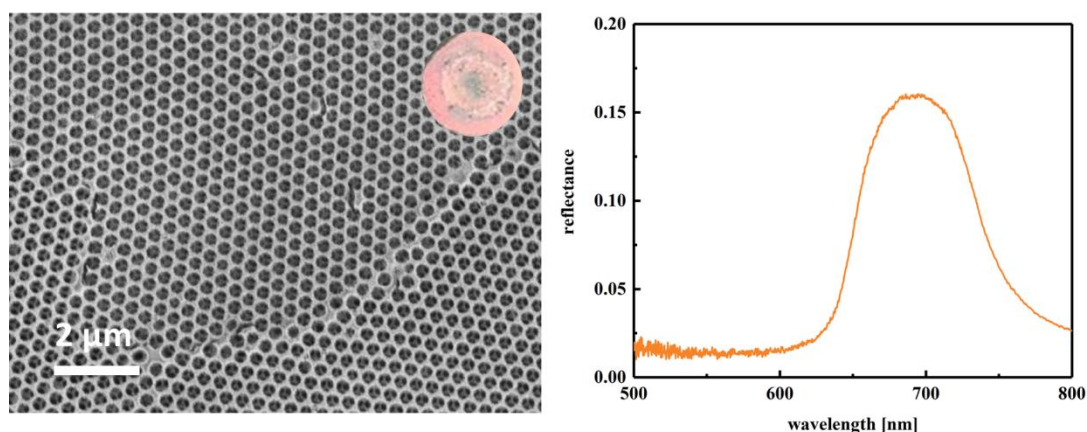


Figure 4.37: SEM image (left) and FTIR spectrum (right) of TiO_2 inverse opal. Insets: photograph of corresponding TiO_2 inverse opal

SEM image reveals highly ordered macroporous structure with pore size about 436 ± 8 nm. The pore size was 14 % smaller compared to the 502 nm template spheres. The measured reflection spectra display well defined peak with the maximum reflectance centered at 690 nm, which is consistent with the red opalescent in the corresponding photograph.

In summary, colloidal SnO_2 and TiO_2 nanoparticles were formed in the precursor solution and then directly infiltrated into the voids of PMMA template. Subsequent removal of the PMMA spheres leads to the ordered macroporous material with the oxide particles forming the walls of the pores. The use of nanoparticles instead of metal nitrates reduces structure shrinkage significantly and allows for forming high quality SnO_2 and TiO_2 inverse opals.

4.3 WO₃ inverse opals and their optical sensing properties

In this present work, tungsten trioxide (WO₃) inverse opals were fabricated according to the literature reported before [120]. Ammonium metatungstate hydrate ((NH₄)₆H₂W₁₂O₄₀·xH₂O) served as precursor. To prepare WO₃ inverse opals with different photonic band gap positions, PMMA spheres of different sizes (298 nm – 644 nm, see section 4.1.1) were used as template materials. The optical properties of resulting WO₃ inverse opals were characterized with SEM and FTIR.

4.3.1 Optical properties of WO₃ inverse opals

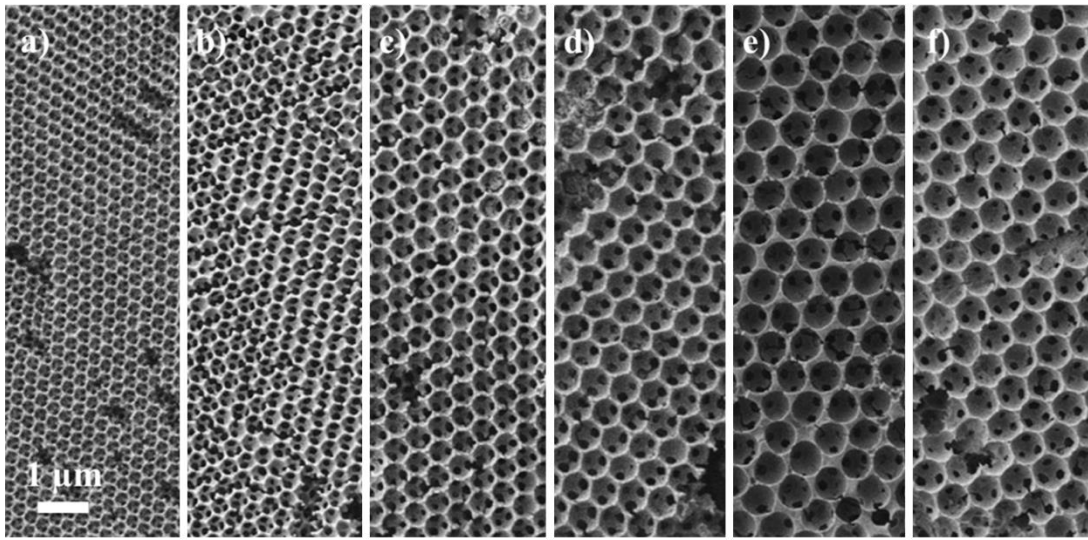


Figure 4.38: SEM images of WO₃ opals with different pore sizes: (a) 277 nm, (b) 355 nm, (c) 452 nm, (d) 553 nm, (e) 583 nm and (f) 619 nm

The synthesized inverse opal films of WO₃ exhibit ordered microporous structures (Figure 4.38). In general, the pore size was found to be correlated with the diameter of PMMA spheres in the parent opal templates. However, varied pore size was also observed for products obtained with PMMA templates of the same diameter in some cases (Figure 4.38 (e) and (f)). This is mainly caused by slight variations in the infiltration or shrinkage process.

The volume fraction of the inverse opal is determined by the shrinkage of entire composite structure and the densification owing to the oxide formation.

The theoretical volume fraction of the solid in an inverse opal structure with a face-centered cubic (fcc) structure without shrinkage is 26 %. The density change caused by the conversion of ammonium metatungstate hydrate to WO₃ results in a volume shrinkage of 46 % (4.07 g·cm⁻³, measured with the method described in [121]) and WO₃ (7.10 g·cm⁻³ [122]).

This results in volume fraction of WO₃ phase in the synthesized WO₃ inverse opal of 14 %. The shrinkage of the whole inverse opal structure leads to an increase of the volume fraction. Assuming a homogenous shrinkage of the inverse opal in all dimensions, the volume increase of the WO₃ was estimated based on the diameter shrinkage in one dimension. Combining the above values, the volume fractions of WO₃ phase were estimated for all the six inverse opals and the results are listed in Table 4.4.

Table 4.4: Summary of the structural parameters of WO₃ inverse opal with different periodicities

	WO ₃ -277	WO ₃ -355	WO ₃ -452	WO ₃ -553	WO ₃ -583	WO ₃ -619
diameters of PMMA particles (nm) ^a	298±5	425±7	502±9	572±8	644±6	644±6
pore sizes of resulting WO ₃ inverse opals (nm) ^a	277±8	355±9	452±5	553±7	583±10	619±5
volume shrinkage of PMMA-WO ₃ composite ^b	-19.67 %	-41.72 %	-27 %	-9.63 %	-25.81 %	-11.20 %
volume fraction ^c	17.43 %	24.02 %	19.18 %	15.49 %	18.87 %	15.77 %

^a Determined by SEM; ^b Calculated with $(\text{WO}_3 \text{ pore size}^3 - \text{PMMA diameter}^3)/\text{PMMA diameter}^3$;

^c Calculated with $0.14/(1 + \text{Volume shrinkage of PMMA-WO}_3 \text{ composite})$.

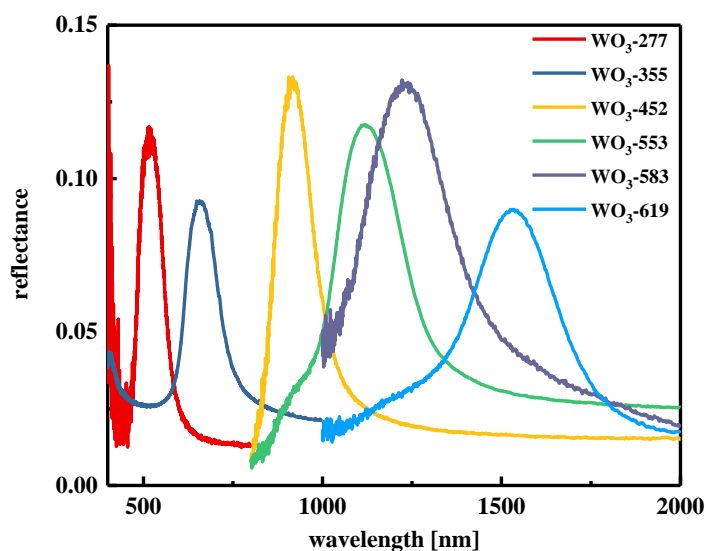


Figure 4.39: FTIR spectra of WO₃ inverse opals with different pore sizes

According to the FTIR spectra, as the pore size of the inverse opal increases, the corresponding reflection peak position shifts to longer wavelength; this is in agreement with the Bragg's law for photonic crystals (see Equation 2.3). However, the Bragg's law predicts a linear variation of the peak position with pore size, which is not the case observed in the current study (Table 4.5 and Figure 4.40). The non-linearity may be resulted by the following reasons: (i) the measurement positions to determine the reflection spectra and the pore diameter are different; (ii) the WO_3 volume fraction varies in different inverse opals; and (iii) the optical dispersion of the refractive index of WO_3 .

Table 4.5: Summary of the pore sizes of resulting WO_3 inverse opals and the corresponding band gap position

	WO_3 -277	WO_3 -355	WO_3 -452	WO_3 -553	WO_3 -583	WO_3 -619
pore sizes of resulting WO_3 inverse opals (nm) ^a	277±8	355±9	452±5	553±7	583±10	619±5
band gap position of WO_3 inverse opals (nm) ^b	515	655	916	1116	1231	1533

^a Determined by SEM ^b Determined by FTIR

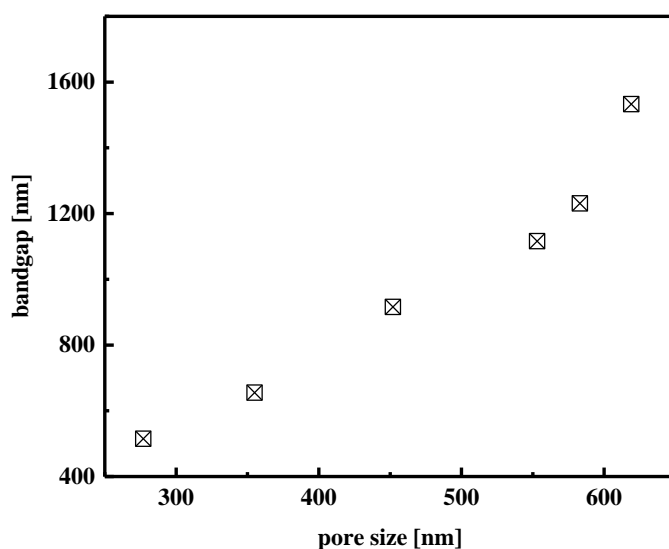


Figure 4.40: Relationship between the band gap position and corresponding pore sizes of WO_3 inverse opal

4.3.2 Crystallite structure of WO_3 inverse opals

The crystallite structures of synthesized WO_3 inverse opal were characterized with Powder X-ray Diffraction (P-XRD). All the fabricated inverse opals have the same orthorhombic WO_3 crystalline structure. One representative X-Ray diffraction of a WO_3 inverse opal (WO_3 -355) is shown in Figure 4.41.

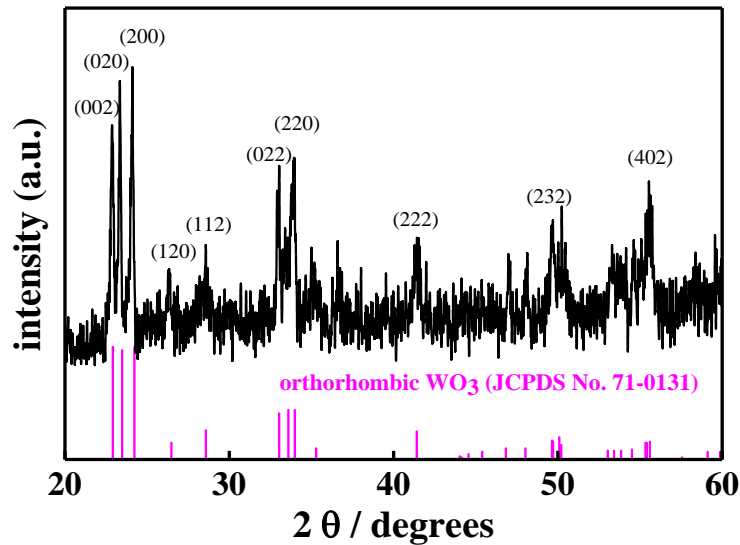


Figure 4.41: X-Ray diffraction patterns of the WO_3 inverse opal (black) and standard diffraction pattern (magenta) of orthorhombic WO_3 (JCPDS No. 71-0131)

The observed XRD patterns show that, WO_3 inverse opal exhibits orthorhombic phase (JCPDS No.71-0131) with the peak maxima at 22.9° , 23.3° and 24.1° corresponding to (002), (020) and (200) planes respectively. The average grain sizes estimated from the full widths at half maximum (FWHM) of the (002), (020) and (200) peaks by using the Scherrer's formula are 67 nm, 86 nm and 73 nm, respectively.

4.3.3 Fluids sensing based on WO_3 inverse opals

With this synthesized WO_3 inverse opals, fluids with different refractive indices were detected. As mentioned in the introduction, introducing fluids in the pores of inverse opals causes increases in the effective refractive index which result in peak shift in the reflection spectra [123]. Here droplets of four different fluids including acetone, ethanol, isopropyl alcohol and water were placed on top of the WO_3 inverse opals and the optical reflections were measured

with FTIR (see 3.3.9). One representative FTIR spectra of WO₃ inverse opal (WO₃-277) before and after introducing different fluids are shown in Figure 4.42.

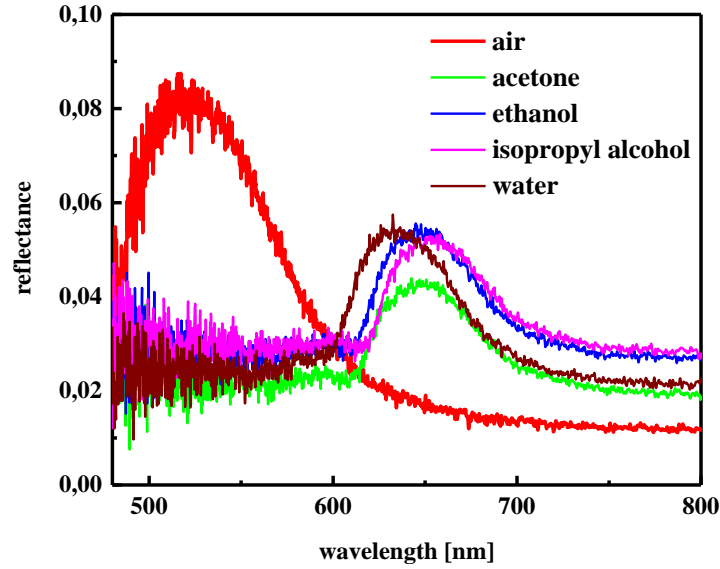


Figure 4.42: FTIR spectra of WO₃ inverse opal (WO₃-277, band gap at 520 nm) before and after introducing different fluids

The infiltration of above-mentioned fluids leads to reversible red shifts in the reflection spectra. All the fluids can be clearly distinguished from the different photonic band gap positions. The corresponding results are summarized in Table 4.6.

The sensitivity (S) is defined by calculating the absolute peak shift per unit change in refractive index from the following equation [124, 125]

$$S = \frac{\Delta\lambda}{\Delta n_{eff}} \quad (4.5)$$

where $\Delta\lambda$ is the reflection peak shift before and after introducing fluids and Δn_{eff} is the corresponding effective refractive index variation of WO₃ inverse opals. The effective refractive index variations can be obtained from the general formula for the effective refractive index of a photonic crystal (Equation 2.4). Here a value of 2.03 was assigned as the refractive index of WO₃ [126].

Table 4.6: Summary of sensitivities of WO₃ inverse opal (WO₃-277, band gap at 520 nm) after introducing different fluids

	water	acetone	ethanol	isopropyl alcohol
refractive index ^a	1.3334	1.3602	1.3628	1.3776
effective refractive index variation	0.2360	0.2571	0.2580	0.2691
peak position after introducing fluids (nm)	634	645	647	652
absolute peak shift (nm)	114	125	127	132
sensitivity (nm·RIU ⁻¹) ^b	483	486	492	491

^a Measured with refractometer ^b RIU: refractive index unit

Table 4.6 shows that, as the refractive index of the pore fluid increases, the reflection peak shifts to longer wavelength region. The calculated sensitivity of the system is about 488 nm·RIU⁻¹, which is comparable to other experimentally realized sensitivities reported in literature [127, 128].

For further investigation same measurements were performed on the WO₃ inverse opals with larger pore sizes. The reflection peak shifts after introducing acetone were chosen to compare the sensitivity of different WO₃ inverse opals. The corresponding FTIR spectra are shown in Figure 4.43 and Figure 4.44.

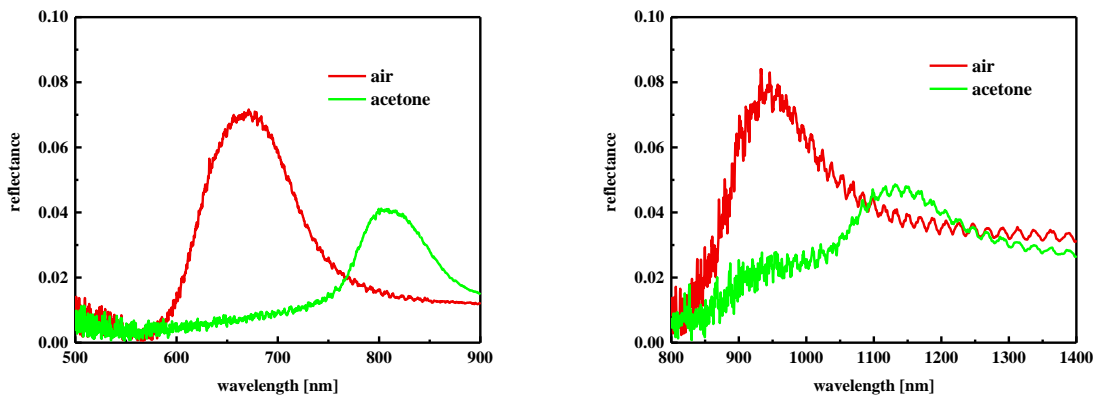


Figure 4.43: FTIR spectra of WO₃ inverse opals (left: WO₃-355, right: WO₃-452) before and after introducing acetone

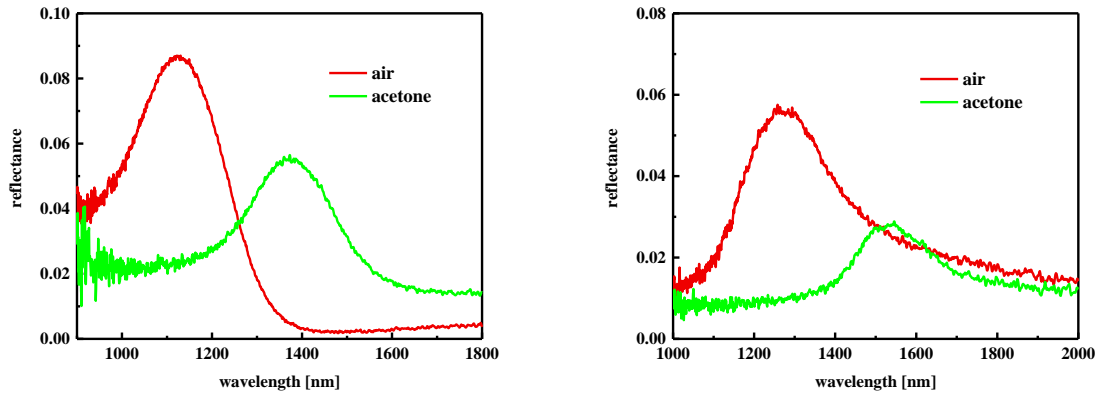


Figure 4.44: FTIR spectra of WO_3 inverse opals (left: WO_3 -553, right: WO_3 -583) before and after introducing acetone

The FTIR spectra reveal different reflection peak shifts to longer wavelength and decreases in reflectance after introducing acetone. The sensitivities of respective WO_3 inverse opals are summarized in Table 4.7 and Figure 4.45.

Table 4.7: Summary of sensitivities of different WO_3 inverse opals

	WO_3 -277	WO_3 -355	WO_3 -452	WO_3 -553	WO_3 -583
pore size (nm)	277 ± 8	355 ± 9	452 ± 5	553 ± 7	583 ± 10
refractive index variation after introducing acetone	0.2571	0.2251	0.2474	0.2659	0.2490
original peak position (nm)	520	670	942	1126	1269
peak position after introducing acetone (nm)	645	808	1129	1372	1531
absolute peak shift (nm)	125	138	187	246	262
sensitivity ($\text{nm} \cdot \text{RIU}^{-1}$)	486	613	756	925	1052

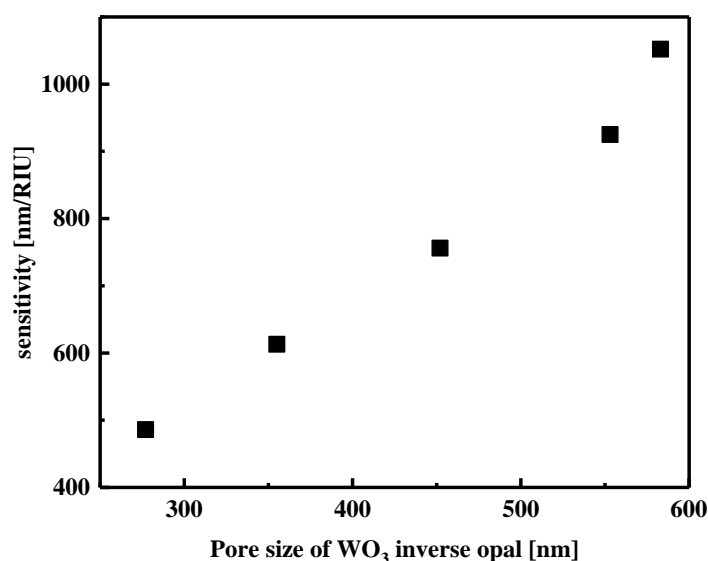


Figure 4.45: Relationship between the pore size of WO₃ inverse opals and the optical sensitivity

From Figure 4.45, it is obvious that the sensitivity increases almost linearly as the pore size of the inverse opal increases. The results indicate that the inverse opals with larger pore sizes are more suitable for distinguishing fluids with small refractive index differences. This is consistent with the previously reported results [129].

In summary, the utilization of WO₃ inverse opals for detecting fluids with different refractive indices is reported. Change of refractive index of the fluid in the pores leads to the shift of the photonic band gap positions. The sensitivity of the system increases with increasing pore sizes of WO₃ inverse opals.

4.3.4 Water temperature sensing based on WO₃ inverse opals

To test the optical sensing possibility towards water temperature a thermo-responsive block copolymer P(DEVBP-b-NIPAAm) was adsorbed into the WO₃ inverse opals (Band gap at 445 nm, synthesized in previous work [120]). The optical properties of WO₃ inverse opals before adsorption, after adsorption and after washing with 20 °C, 40 °C and 60 °C water were characterized using FTIR in a mapping mode. The corresponding results are shown in Figure 4.46 – 4.51. The reported reflection spectra are the average of 12 independent measurements.

Washing with 20 °C water

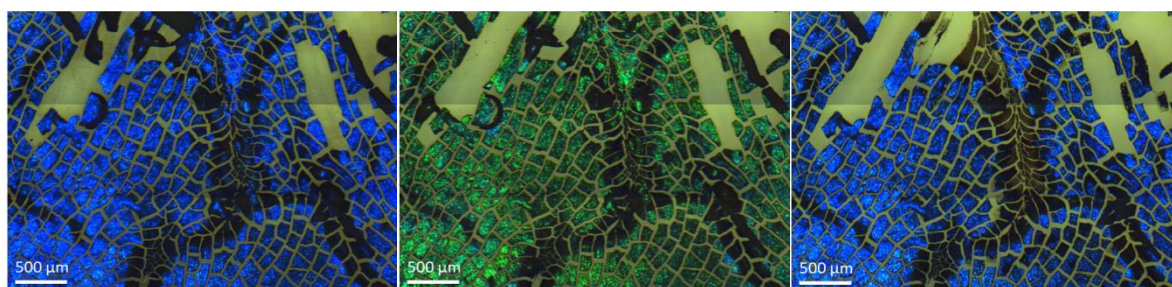


Figure 4.46: Microscope pictures of WO₃ inverse opal before adsorption (left), after adsorption (middle) and after washing with 20 °C water (right)

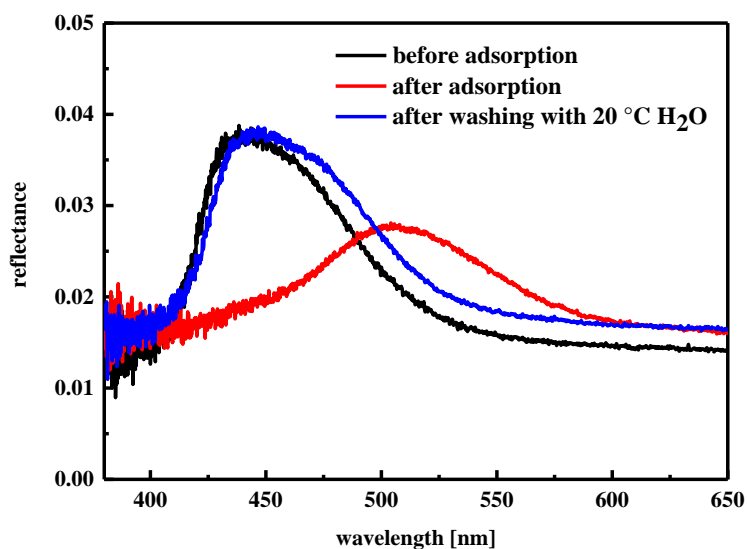


Figure 4.47: FTIR spectra of WO₃ inverse opal before adsorption, after adsorption and after washing with 20 °C water

As shown in Figure 4.47, the infiltration of P(DEVBP-b-NIPAAm) into the void spaces of the WO₃ inverse opal cause a red shift of 68 nm (from 445 nm to 513 nm) in the reflection spectra because the adsorbed polymer induce a strong variation in the effective refractive index of WO₃ inverse opal. After washing with 20 °C water, the maximum reflectance return to its original state owing to the desorption of the block copolymer from the pores. This is consistent with the results from microscope pictures (Figure 4.46), where the color of WO₃ inverse opal changes from blue to green after polymer adsorption and turns back to blue after washing with 20 °C water.

Washing with 40 °C water

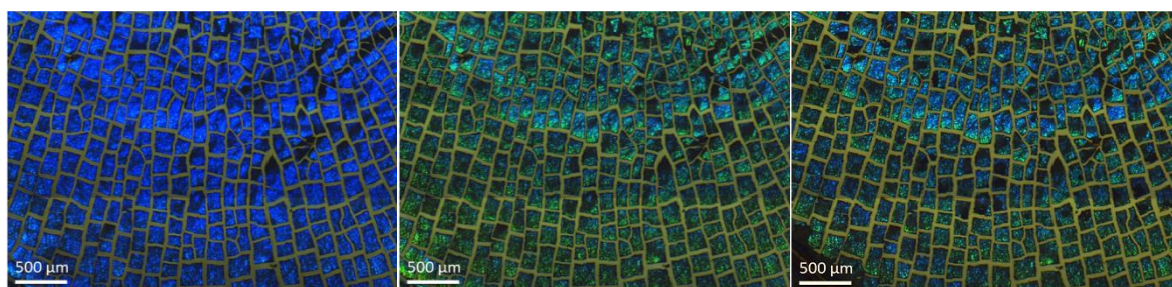


Figure 4.48: Microscope pictures of WO_3 inverse opal before adsorption (left), after adsorption (middle) and after washing with 40 °C water (right)

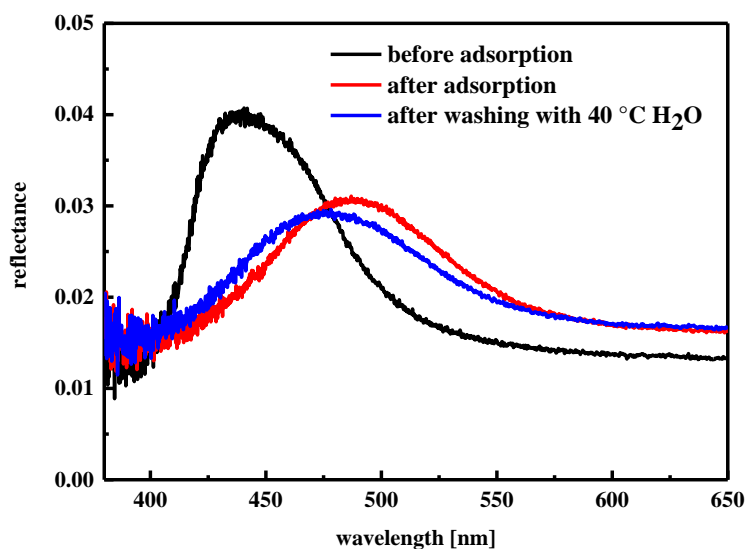


Figure 4.49: FTIR spectra of WO_3 inverse opal before adsorption, after adsorption and after washing with 40 °C water

Figure 4.49 shows the FTIR results of testing with 40 °C water, the band gap position of WO_3 inverse opal shifts to longer wavelength after polymer adsorption, however, does not return to its original state after washing with 40 °C water. In the corresponding microscope pictures (see Figure 4.48), the color of WO_3 changes from blue to green after polymer adsorption and stay green after washing with 40 °C water. The peak shift and color change indicate that the block copolymer adsorbed onto the air-containing pores of the WO_3 inverse opal and remain constant in 40 °C water.

Washing with 60 °C water

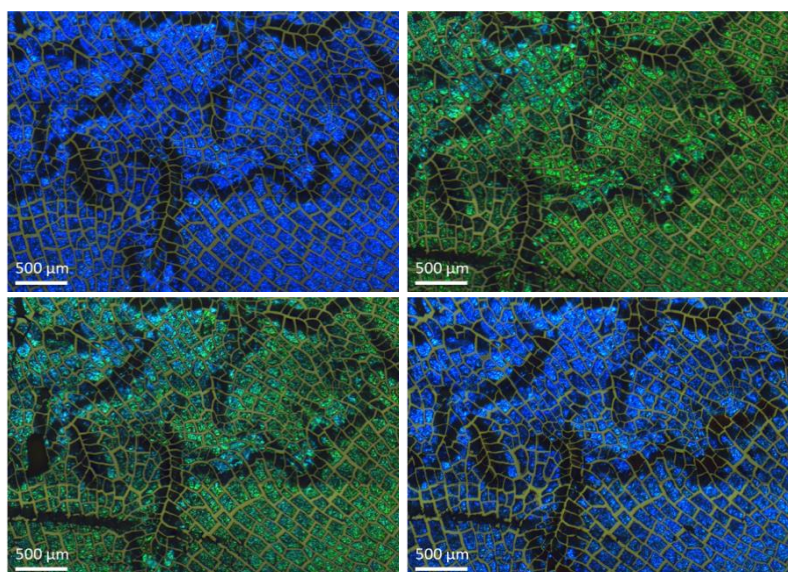


Figure 4.50: Microscope pictures of WO₃ inverse opal before adsorption (top left), after adsorption (top right), after washing with 60 °C (below left) and 20 °C water (below right) successively

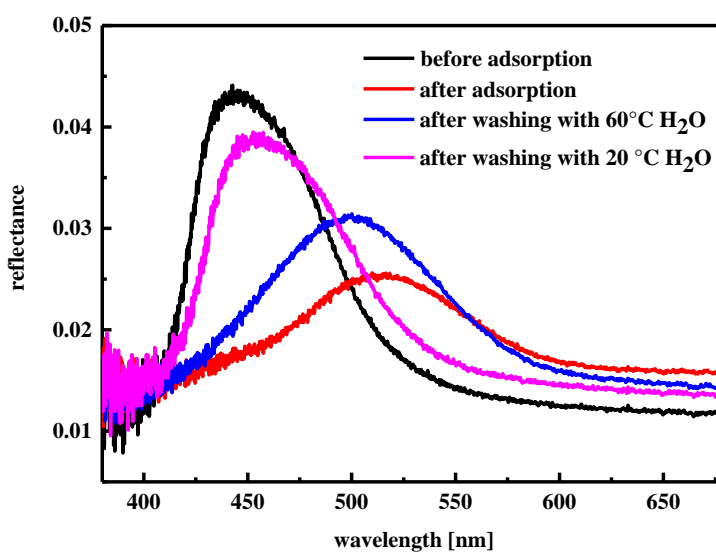


Figure 4.51: FTIR spectra of WO₃ inverse opal before adsorption, after adsorption, and after washing with 60 °C and 20 °C water successively

Similar results can be observed by testing with 60 °C water. The photonic band gap position of WO₃ inverse opal shifts to longer wavelength after polymer adsorption, shifts back for about 10 nm after washing with 60 °C water and almost returns to its original position after washing with 20 °C water.

In summary, an optical water temperature sensor was fabricated based on block copolymer infiltrated WO_3 inverse opal. The desorption behaviors at different water temperature lead to different color changes, which can also be overserved as change in the reflection peak position. Although it can only be used to identify whether the water temperature is below or above $30\text{ }^\circ\text{C}$ (critical solution temperature of the infiltrate polymer), this study demonstrates the potential for optical detection with adsorbable and temperature responsive material, which provides the possibility for using infiltrated metal oxide inverse opals to detect other external stimuli.

4.3.5 H_2 sensing based on WO_3 inverse opals

Previous results have shown that H_2 sensing is possible by monitoring the reflection peak shift of WO_3 inverse opals owing to a H_2 induced change of refractive index [120]. In this study the reflection peak shifts of synthesized WO_3 inverse opals was examined, with the aim to enhance the optical response in hydrogen detection.

The gas sensing measurement was first performed in an open system using two different WO_3 inverse opals (WO_3 -277 and WO_3 -355) to check the possible difference in optical response at different wavelengths. The band gap position of WO_3 -277 is located at 525 nm, while the band gap position of WO_3 -355 is located at 601 nm. Platinum (Pt) catalyst is deposited on the inverse opals before measurement. The corresponding reflection peak position shifts during H_2 sensing measurement are shown in Figure 4.52.

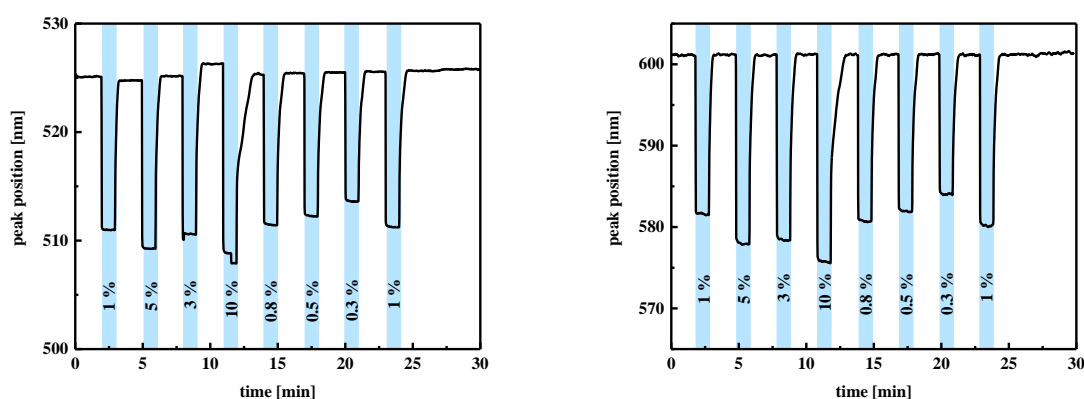


Figure 4.52: Reflection peak position shift of WO_3 inverse opals (left: WO_3 -277, right: WO_3 -355) during H_2 sensing measurement in open system at $200\text{ }^\circ\text{C}$ (blue region: H_2 exposure; white region: flushed by pure N_2)

The results show that the reflection peaks of the two WO₃ inverse opals shift to shorter wavelengths (blue-shift) when it is exposed to H₂. The regeneration of WO₃ is allowed by flushing with pure N₂. The response times both for gas reaction and sensor regeneration are quite rapid. In addition, the reflection peak shifts are correlated with H₂ concentration. In general, the blue shift increases with the H₂ concentration ranging from 0.3 vol% to 10 vol%. However the peak shift and corresponding optical response towards same H₂ concentration are different for the two WO₃ inverse opals. The optical response is defined as $R = \Delta\lambda/\lambda_0$, where $\Delta\lambda$ is the absolute peak shift when expose to H₂ and λ_0 is the original peak position. The results are summarized in Table 4.8 and Figure 4.53.

Table 4.8: Summary of the optical response of WO₃-277 (Band gap: 525 nm) and WO₃-355 (Band gap: 601 nm) at different H₂ concentration

H ₂ concentration	optical response of WO ₃ -277	optical response of WO ₃ -355
1 vol%	-2.72 %	-3.38 %
5 vol%	-2.95 %	-3.89 %
3 vol%	-2.82 %	-3.79 %
10 vol%	-3.68 %	-4.33 %
0.8 vol%	-2.63 %	-3.39 %
0.5 vol%	-2.50 %	-3.26 %
0.3 vol%	-2.29 %	-2.86 %
1 vol%	-2.74 %	-3.54 %

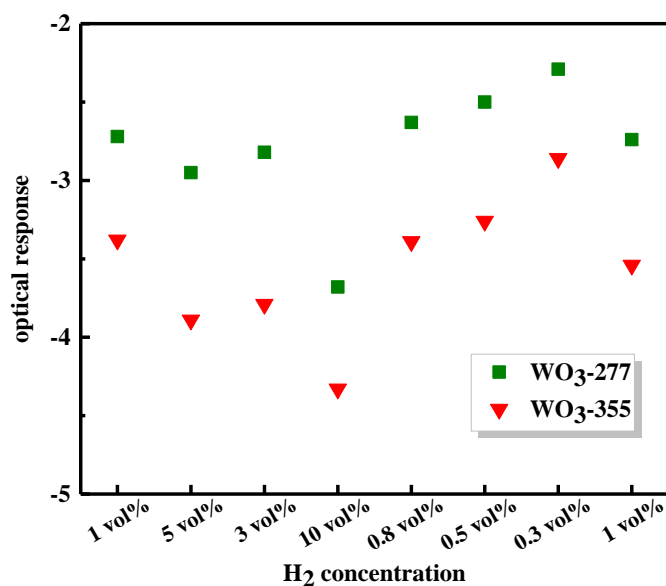


Figure 4.53: Compare the optical response of WO₃-277 and WO₃-355 at different H₂ concentration

It is obvious that, at same H₂ concentration the optical response of WO₃-355 (band gap: 601 nm) is larger than that of WO₃-277 (band gap: 525 nm). The results confirm that the optical responses are different for inverse opals with different band gap position and could be optimized directly by changing the pore sizes of respective inverse opals.

To further verify this idea, H₂ sensing measurements of a series of WO₃ inverse opals were then carried out in a custom-built gas cell at 140 °C (see 3.3.9). The corresponding H₂ sensing curves are shown in Figure 4.54 - 4.56.

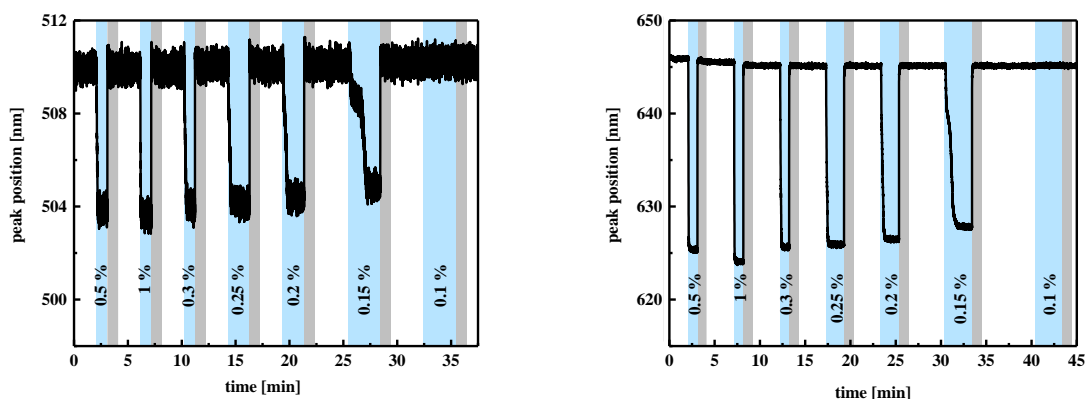


Figure 4.54. Reflection peak position shifts of WO₃ inverse opals (left: WO₃-277, right: WO₃-355) during H₂ sensing measurement at 140 °C. (blue region: H₂ exposure; grey region: regeneration by synthetic air; white region: flushed by pure N₂)

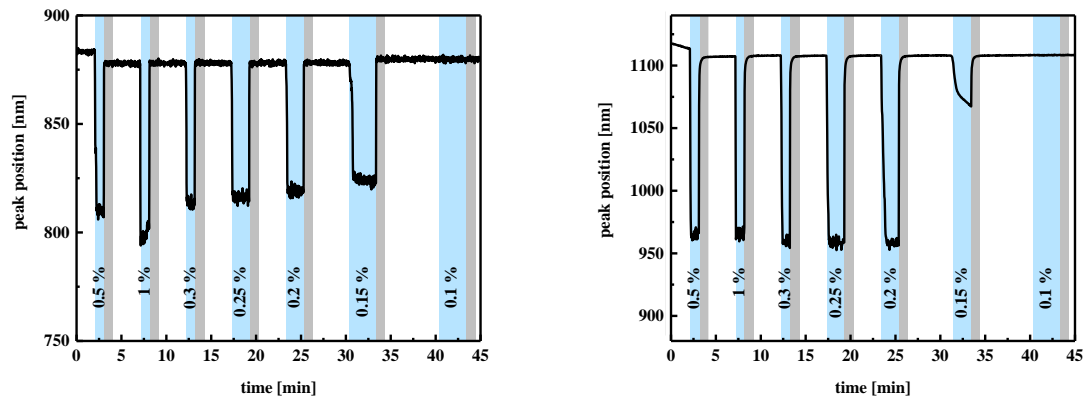


Figure 4.55. Reflection peak position shifts of WO_3 inverse opals (left: WO_3 -452, right: WO_3 -553) during H_2 sensing measurement at $140\text{ }^\circ\text{C}$. (blue region: H_2 exposure; grey region: regeneration by synthetic air; white region: flushed by pure N_2)

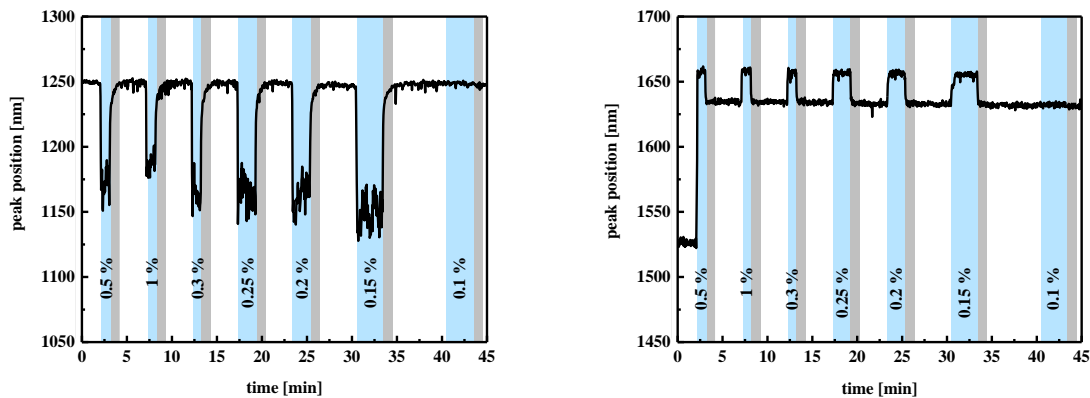


Figure 4.56. Reflection peak position shifts of WO_3 inverse opals (left: WO_3 -583, right: WO_3 -619) during H_2 sensing measurement at $140\text{ }^\circ\text{C}$. (blue region: H_2 exposure; grey region: regeneration by synthetic air; white region: flushed by pure N_2)

It can be seen that, except for the last sample WO_3 -619, the reflection peaks of the WO_3 inverse opals shift to shorter wavelengths as a response to H_2 in the concentration range of $0.15 \sim 1\text{ vol}\%$. Meanwhile, the lowest H_2 concentration ($0.1\text{ vol}\%$) cannot be detected. This detection limit may be caused by H_2 being completely consumed by the sensing materials before hitting the local optical measurement spot. It could also involve the absorption mechanism of WO_3 upon H_2 exposure, which will be discussed latter.

The reflection peaks of WO_3 recover to a stable peak position when the material is subjected to synthetic air for regeneration. The stable position, however, differs from the original peak position (i.e. peak position before the first H_2 exposure) for all the WO_3 inverse opals tested.

The discrepancy indicates an incomplete regeneration after the first H₂ exposure, which is probably caused by WO₃ lattice trapping protons and electrons until a stable state with all the available sites occupied [130].

The WO₃ inverse opals show short response time for both gas reaction and sensor regeneration. However, comparably longer time is required for the response to lower H₂ concentration to reach an equilibrium, indicating the involvement of a diffusion process in the refractive index variation of WO₃.

The optical response of the six inverse opals was then compared based on reflection peak shifts induced by 1 vol% H₂. The original peak positions (λ_0), the peak positions after exposure to 1 vol% H₂ (λ_1), the absolute peak shift ($\Delta\lambda = \lambda_1 - \lambda_0$) and the relative shift (i.e. optical response $R = \Delta\lambda/\lambda_0$) are summarized in Table 4.9 and Figure 4.57.

Table 4.9: Summary of gas response of WO₃ inverse opals with different periodicities

	WO ₃ -277	WO ₃ -355	WO ₃ -452	WO ₃ -553	WO ₃ -583	WO ₃ -619
original peak position (nm)	510	646	883	1117	1250	1526
peak position (1 vol% H ₂) (nm)	504	624	798	965	1182	1658
absolute peak shift (nm)	-6	-22	-85	-152	-68	132
optical response	-1.2%	-3.4%	-9.6%	-13.6%	-5.4%	8.7%

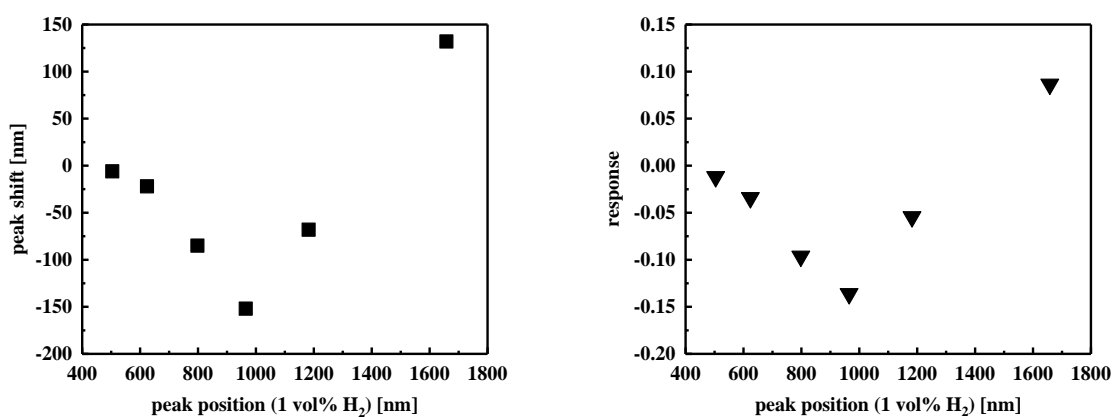


Figure 4.57: Relationship between the peak position when exposed to 1 vol% H₂ and peak shift (left) / optical response (right) of WO₃ inverse opals when exposed to 1 vol% H₂

As indicated by the results, blue shift was observed for inverse opals with λ_0 from 510 nm to 1117 nm and the degree of which ($|\Delta\lambda|$) increased along with λ_0 . Blue shift still occurred for the inverse opal with a further increased λ_0 of 1250 nm (WO₃-583), however, the shift is smaller than the inverse opal of 1117 nm. Moreover, instead of blue shift, a red shift was displayed by the inverse opal with the largest λ_0 (1526 nm, WO₃-619). The observed peak shift trends for the inverse opals indicate that after H₂ exposure, the refractive index of H_xWO₃ decreases in the spectral range of 504 ~ 1182 nm, before increasing at a longer wavelength range.

Subsequently, the determined optical response was applied for the calculation of refractive indices of H_xWO₃ at different wavelengths

$$R = \Delta\lambda/\lambda_0 = \Delta\bar{n}/\bar{n}_0 = (\bar{n}_1 - \bar{n}_0)/\bar{n}_0 \quad (4.6)$$

Here the average refractive index of WO₃ inverse opals (\bar{n}_0) and H_xWO₃ inverse opals (\bar{n}_1) can be calculated according to Equation 2.4. The refractive index of WO₃ (n_{oxide}) is assumed to remain constant in the measured spectral range. Thereby, upon 1 vol% H₂ exposure, the dispersion of the refractive index of H_xWO₃ could be estimated. The values are summarized in Table 4.10 and Figure 4.58.

Table 4.10: Summary of refractive indices of H_xWO₃ when exposed to 1 vol% H₂ with different periodicities

	WO ₃ -277	WO ₃ -355	WO ₃ -452	WO ₃ -553	WO ₃ -583	WO ₃ -619
peak position (1 vol% H ₂) (nm)	504	624	798	965	1182	1658
refractive index of H _x WO ₃	2.00	1.97	1.82	1.68	1.91	2.22

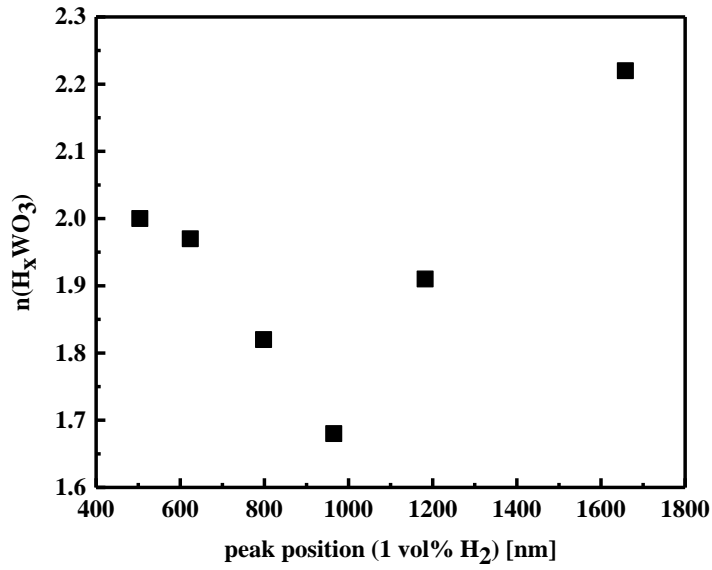


Figure 4.58: Estimated dispersion of the refractive index of H_xWO₃

As shown in Figure 4.58, the dispersion curve was found to be in a similar shape to the curves of absolute peak shift (Figure 4.57 left) and optical response (Figure 4.57 right) at different wavelengths. Based on the assumption of constant refractive index of WO₃, the refractive index change between WO₃ and H_xWO₃ was expected to display the similar dispersion shape. Although the periodicity varies among the inverse opals, the cause of the dispersion of H₂ induced optical response was determined to be the different changes of the refractive index of WO₃ associated with different wavelengths.

The maximum change of refractive index was obtained with the wavelength around 965 nm. Consequently, an optical response, which is one order of magnitude stronger than that at 504 nm, was achieved at 965 nm. The shape of the dispersion curves obtained for the inverse opals is closer to those of crystalline H_xWO₃ thin films referring to literature on amorphous [131, 132] and crystalline [119] H_xWO₃ thin films.

There are very limited data reported on the dispersion of the refractive index of H_xWO₃, thus, the free carrier absorption model was tested based on the estimated data. The fitting of the dispersion curve was attempted by the equations mentioned in the introduction (section 2.3.3, Equation 2.14 - 2.16)

$$\epsilon_1(\omega) = \epsilon_\infty - \frac{\omega_p^2}{\omega^2 + \gamma^2}$$

$$\epsilon_2(\omega) = \frac{\omega_p^2 \gamma}{\omega^3 + \omega \gamma^2}$$

$$\epsilon(\omega) = \epsilon_1(\omega) + i\epsilon_2(\omega) = \epsilon_\infty - \frac{\omega_p^2}{i\omega\gamma + \omega^2}$$

where ω is the light frequency, $\epsilon(\omega)$ is the complex relative permittivity, with $\epsilon_1(\omega)$ and $\epsilon_2(\omega)$ representing the real and imaginary part, respectively. They are related to the refractive index of H_xWO_3 ($n_{\text{bronze}}(\omega)$) as expressed by a modification of Equation 2.12

$$n_{\text{bronze}}^2(\omega) = \frac{1}{2}(\sqrt{\epsilon_1(\omega)^2 + \epsilon_2(\omega)^2} + \epsilon_1(\omega))$$

Here the background permittivity (ϵ_∞) at high light frequency, the plasma frequency (ω_p), and the damping coefficient (γ) are the fitting parameters. The Drude model was verified to provide an ideal fitting of the estimated dispersion curve, as indicated by the value of 0.94 (close to 1) calculated with adjusted R^2 (Figure 4.59). The corresponding fitting parameters are $\epsilon_\infty = 5.49$, $\omega_p = 8.22 \times 10^{14}\text{Hz}$, and $\gamma = 3.41 \times 10^{14}\text{Hz}$. The values of ω_p and γ are in reasonable agreement with literature ($\omega_p = 9.48 \times 10^{14}\text{Hz}$ and $\gamma = 2.70 \times 10^{14}\text{Hz}$ [126]). However, the fitting value for ϵ_∞ (5.49) is considerably larger than the value reported in literature (4.11 [126]), implying a larger fitting value ($n_{\text{oxide}} = \sqrt{\epsilon_\infty} = 2.34$) than the assumed value of n_{oxide} (2.03 [126]). This discrepancy may be caused by various factors, including errors in volume fraction estimation, a possible complex mechanism of optical response, and the assumption of constant ϵ_∞ which is too simple. Despite the discrepancy, it is still of great significance to reveal that the refractive index of H_xWO_3 displays a strong dispersion which matches the Drude model in the spectral range of 500 nm \sim 1.5 μm . Generally, Drude model describes the microscopic interaction between free charge carriers and light. The fact that Drude model provided satisfactory fitting result to the dispersion curve indicates the physical origin of the strong dispersion of the refractive index of H_xWO_3 being predominantly H_2 induced free carrier absorption, which also results in optical response of WO_3 inverse opals upon H_2 exposure.

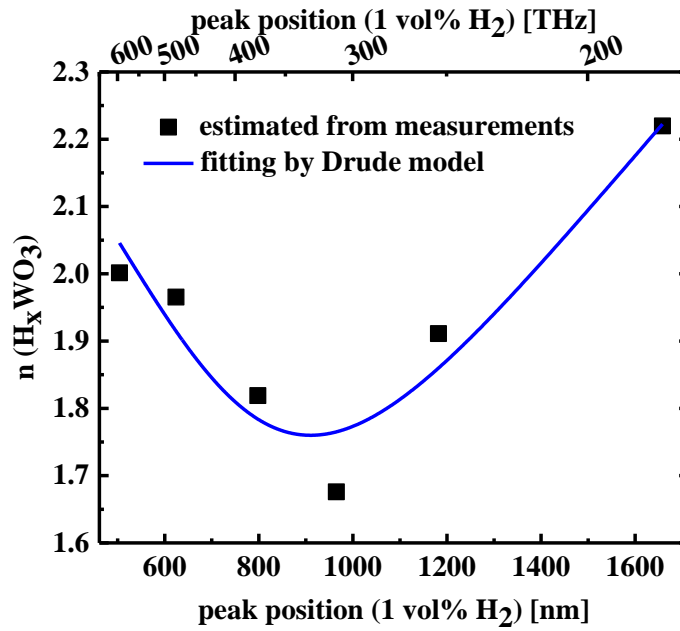


Figure 4.59: Estimated dispersion of the real part of the refractive index of H_xWO_3 (black scatters) and the fitting curve (blue line) based on Drude model

Since free carrier absorption has been verified to be the main physical mechanism, the question left previously on the detection limit of 0.15 vol% H_2 can be explained from this angle. To elaborate on it, H_2 does not provide enough electrons with a lower concentration than the limit (0.15 vol%). Due to the insufficiency of electrons, there is an absence of free electrons in the conduction band as the few electrons donated by H_2 are most likely to be consumed by localized states [130] without contributing to free carrier absorption. As a consequence, the optical response cannot be triggered by low H_2 concentrations. With elevated concentration of H_2 more protons are intercalated and large amount of free electrons are donated close to the conduction band minimum, which not only leads to the free carrier absorption - an intraband transition, but also can potentially modify the apparent electronic band gap related to the interband transitions [131, 133]. As illustrated above, the first effect has the largest influence on the refractive index dispersion in IR range, and the far-reaching tail of this influence leads to a relatively smaller modification in UV-VIS range. The second phenomenon has already been reported for amorphous WO_3 films. It could be a combined result of Burstein-Moss shift, electron-electron and electron-ion scattering, and structural change induced by intercalation [131, 133]. However, the corresponding modification effect on electronic band gap size is insignificant [133], and no measurable modification observed for crystalline WO_3 films [130]. Therefore, H_2 exposure does not affect the background refractive index of WO_3 at high frequency. However, it is non-negligible that both intra- and inter-band transitions can play a

role in the dispersion of optical constants of the metal oxides upon gas exposure, especially with a spectral region of interest close to the electronic band gap energy.

Based on the results and discussion above, guidelines for designing an optical metal oxide gas sensor are concluded:

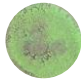







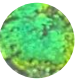
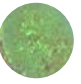
- (i) A suitable metal oxide, mainly among metal oxides with resistive type sensing properties, need to be identified for the target gas.
- (ii) The range of light frequency needs to be determined in terms of the most significant gas-induced modulation of refractive index. The light frequency range for semiconducting metal oxides mainly locates in the NIR to MIR region. Drude model can be employed for the identification of the specific location. In the identification process, the frequency of the minimum reflectance from a smooth, unstructured metal oxide film is firstly determined for the estimation of plasma frequency, which then enables the identification of the metal oxide's dispersion of the refractive index and thereby, the frequency range associated to the maximum modulation of refractive index.
- (iii) Photonic crystals need to be fabricated, targeting a photonic band gap in the light frequency range determined. The frequency for maximum modulation varies depending on free charge carrier amount, hence, the band gap position is dependent on structural factors, e.g. lattice defects.

In addition, aspects, such as the feasibility of employing larger PMMA spheres for the fabrication of photonic crystals with a photonic band gap at longer wavelengths and the expense on more expansive detectors in IR range, also need to be considered for making practical gas sensing devices.

5. Summary

In this present study, ten different metal oxide inverse opals including CeO_2 , CuO , Cr_2O_3 , Fe_2O_3 , Ga_2O_3 , In_2O_3 , SnO_2 , TiO_2 , WO_3 and ZnO were successfully synthesized via colloidal crystal templating method. Monodisperse PMMA spheres were used to grow colloidal opal template. All the fabricated inverse opals exhibit high optical reflectance and iridescent structural colors (Table 5.1).

Table 5.1: Photograph of the as-synthesized metal oxide inverse opals

CeO_2	CuO	Cr_2O_3	Fe_2O_3	Ga_2O_3	In_2O_3	SnO_2	TiO_2	WO_3	ZnO
									

Each of the ten types of inverse opals required different types of precursors and processing conditions to optimize their optical reflectance. Respective metal nitrates were employed as precursor materials to fabricate inverse opals of CeO_2 , CuO , Cr_2O_3 , Fe_2O_3 , Ga_2O_3 , In_2O_3 , and ZnO . Among them, well-ordered Cr_2O_3 , Ga_2O_3 , Fe_2O_3 and In_2O_3 can be fabricated with pure metal nitrates. However, in case of CeO_2 , CuO and ZnO only disordered structures were formed following the same synthesis procedure. Comprehensive analysis of the precursor conversion process and the thermal stability of PMMA templates revealed the effect of the glass transition temperature of PMMA and the onset temperature of nitrate conversion on the structural quality of the inverse opals. In order to fabricate well-ordered metal oxide inverse opals, the presence of a rigid template during precursor conversion is of great importance. More specifically, a rigid precursor network needs to be formed before the mechanical rigidity of the polymer template weakens during glass transition. Furthermore, solidification strategies of precursor networks were also confirmed to be effective for the formation of well-ordered inverse opal structures. Following this idea, three modification strategies including organic chelating, sol-gel polymerization of TEOS and polyacrylamide gelation were attempted to strengthen the precursor networks. Consequently, inverse opals of CeO_2 , CuO and ZnO were fabricated successfully. These design principles and precursor solidification methods are expected to extensively apply to the fabrication of other metal oxide inverse opals.

Besides metal nitrates, nanoparticles of desired oxide were applied to fabricate SnO_2 and TiO_2 inverse opals. By using hydrolysable SnCl_4 and $\text{Ti}(\text{OC}_4\text{H}_9)_4$ as precursor material, colloidal

SnO₂ and TiO₂ nanoparticles were formed in the respective precursor solution and directly infiltrated into the voids of PMMA template. Subsequent removal of PMMA spheres leads to the ordered macroporous material with the oxide particles forming the walls of the pores. With the use of nanoparticles instead of metal nitrates, structure shrinkage was reduced significantly and inverse opals of SnO₂ and TiO₂ with a porous network over a large area were obtained.

In addition to the synthesis and characterization of metal oxides inverse opals, another part of this work is the optical sensing based on WO₃ inverse opals. WO₃ inverse opals were fabricated using PMMA opals with different sphere sizes. The diameters of PMMA spheres were adjusted using different monomer concentrations.

First, fluid sensing was performed on different WO₃ inverse opals. Changes of refractive index of the fluid in the pores of inverse opals lead to different red shifts in the corresponding reflection spectra. All the detecting fluids can be identified from the different photonic band gap positions. A more detailed data analysis reveals that the sensitivity of the system increases as the pore size of the WO₃ inverse opal increases.

In addition, a temperature responsive block copolymer was infiltrated into WO₃ inverse opals. By washing with water with different temperatures and measuring the corresponding change in reflection spectra, the difference in water temperature were transduced into optical signal, which enables a new type of optical sensor to detect water temperature. Further work will focus on finding other adsorbable stimuli-responsive materials to expand applications of metal oxide inverse opals in optical sensing.

Furthermore, the application of WO₃ inverse opals with different photonic band gap positions for optical hydrogen sensing was investigated. The optical responses of these WO₃ inverse opals to H₂ at different concentrations were tested. Based on the responses to 1 vol% H₂ at various wavelengths, the strong refractive index dispersion of WO₃ upon H₂ was reconstructed. A satisfactory fitting of the dispersion shape was provided by Drude model, indicating free carrier absorption being the predominant physical origin of the optical response. The dispersion curve provides a useful tool for the determination of the wavelength associated to the maximum modulation of refractive index, and thereby, the maximum gas induced optical response.

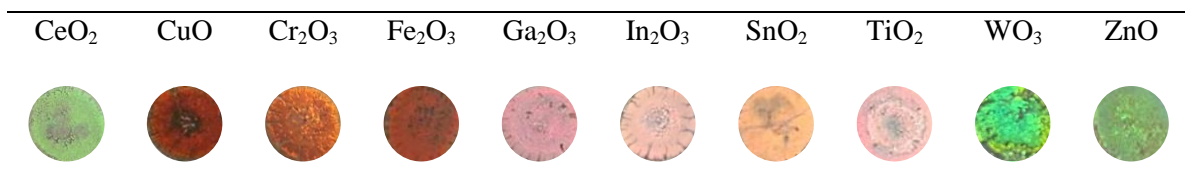
Free carrier density is the key parameter determining the dispersion of free carrier absorption and the conductance of semiconducting metal oxides. As suggested by resistive type sensors,

the conductance of metal oxides is greatly affected by test gases, which indicates a strong gas induced variation of the free carrier density. Therefore, upon exposure to the corresponding test gases, optical responses are expected for most metal oxides. However, in order to achieve a measurable optical response the spectral range for measurement needs to be close to the strong dispersion region of the optical constants of metal oxides. According to the magnitude of free carrier density variation, the spectral range is determined to be in the IR region for most metal oxides as gas sensors. In the following steps, further investigation will be carried out on the fabrication and application of metal oxides inverse opals with larger photonic band gap positions, to broaden the choice of sensing materials for optical gas sensors.

6. Zusammenfassung

In der vorliegenden Arbeit wurden zehn verschiedene Metalloxid-Inversopale wie CeO_2 , CuO , Cr_2O_3 , Fe_2O_3 , Ga_2O_3 , In_2O_3 , SnO_2 , TiO_2 , WO_3 und ZnO mithilfe kolloidaler Kristalltemplate erfolgreich synthetisiert. Dabei wurden PMMA-Opale als Template eingesetzt. Monodisperse PMMA Kugeln wurden hierfür als Baueinheiten verwendet, um eine Selbstorganisation von PMMA-Opalen zu erzielen. Alle hergestellten Metalloxid-Inversopale zeigen schillernde Strukturfarben mit hoher optischer Reflektivität auf (Tabelle 6.1).

Tabelle 6.1: Fotografie der hergestellten Metalloxid-Inversopale



Jede der zehn Typen der Inversopale benötigte unterschiedliche Arten von Präkursoren und Verarbeitungsbedingungen, um die jeweilige Reflektivität zu optimieren. Das jeweilige Metallnitrat wurde als Präkursormaterial verwendet, um die Inversopale aus CeO_2 , CuO , Cr_2O_3 , Fe_2O_3 , Ga_2O_3 , In_2O_3 , und ZnO herzustellen. Aus diesen können die hoch geordneten Cr_2O_3 , Ga_2O_3 , Fe_2O_3 und In_2O_3 mit reinem Metallnitrat hergestellt werden. Jedoch sei darauf hingewiesen: Im Falle von CeO_2 , CuO und ZnO wurden nur ungeordnete Strukturen anhand der gleichen Syntheseschritte gebildet. Eine ausführliche Analyse des Präkursor-Konversionsprozesses und der thermischen Stabilität von PMMA-Opalen ergab, dass Glasübergangstemperatur des PMMA und der Nitratumsetzungstemperaturen der Präkursors auf die strukturelle Qualität der Inversopale beeinflusst werden. Im Allgemeinen muss der Metalloxid-Präkursor ein strenges Netzwerk bilden, bevor die Template während des Glasübergangsprozesses ihre mechanische Stabilität verlieren. Darüber hinaus wurde auch bestätigt, dass eine Verfestigung der Präkursornetzwerke für die Bildung hoch geordneter Inversopalstrukturen wirksam ist. In der vorliegenden Arbeit wurden drei unterschiedliche Modifizierungsmethoden angewendet, einschließlich der organischen Chelatisierung, die Sol-Gel-Polymerisation von TEOS und die Polyacrylamid-Gelierung, um die Präkursornetzwerke zu verfestigen. Nach Modifikationen wurden die geordneten Inversopalen von CeO_2 , CuO und ZnO erfolgreich synthetisiert. Die Prinzipien des Designs und die Methoden der Präkursormodifikation können weitgehend ebenso auf die Synthese anderer Metalloxid-Inversopale angewendet werden.

Neben Metallnitraten wurden Nanopartikel des gewünschten Oxids zur Herstellung der SnO_2 - und TiO_2 -Inversopale verwendet. Unter Verwendung von hydrolysierbarem SnCl_4 und $\text{Ti}(\text{OC}_4\text{H}_9)_4$ wurden kolloidale SnO_2 - und TiO_2 - Nanopartikeln in der jeweiligen Präkursorlösung gebildet und anschließend direkt in die Hohlräume der PMMA-Template infiltriert. Die anschließende Entfernung der PMMA-Kugeln führt zu den geordneten makroporösen Strukturen, wobei die Oxidpartikeln die Wände der Poren bilden. Durch die Verwendung von Nanopartikeln anstelle von Metallnitraten wurde die Strukturschrumpfung signifikant reduziert.

Neben der Synthese und Charakterisierung der Metalloxid-Inversopale liegt ein weiterer Fokus dieser Arbeit in der optischen Sensorik. Dabei wurden Inversopale aus WO_3 verwendet. WO_3 -Inversopale wurden auch mithilfe kolloidaler Kristalltemplate von PMMA-Opalen synthetisiert. Durch Verwendung von PMMA-Kugeln mit unterschiedlichen Partikelgrößen wurden die photonische Bandlücken der WO_3 -Inversopale von sichtbarem Bereich bis zum NIR Bereich variiert. Die Durchmesser der PMMA-Kugeln wurden mit unterschiedlichen Monomer-konzentrationen eingestellt.

WO_3 -Inversopale wurden zunächst in die Flüssigkeits-Sensorik eingesetzt. Die Änderungen des Brechungsindex der Flüssigkeit in den Poren von Inversopalen führen zu unterschiedlichen Peak-Verschiebungen in den entsprechenden Reflexionsspektren. Alle getesteten Flüssigkeiten können anhand der verschiedenen Peak-Positionen identifiziert werden. Eine detailliertere Datenanalyse zeigt, dass die Empfindlichkeit des Systems mit zunehmender Porengröße des WO_3 -Inversopals zunimmt.

Darüber hinaus wurde ein temperaturempfindliches Blockcopolymer in die WO_3 -Inversopale infiltriert. Durch Waschen mit Wasser unter unterschiedlichen Temperaturen und Messen der entsprechenden Änderung der Reflexionsspektren wurde die Differenz der Wassertemperatur ins optische Signal umgewandelt, wobei es einem neuen Typ von optischem Sensor möglich ist, die Wassertemperatur zu prüfen. Weitere Arbeiten werden sich auf die Suche nach anderen adsorbierbaren und stimulierungsempfindlichen Materialien konzentrieren, damit die Anwendungen von Metalloxid-Inversopalen in der optischen Sensorik erweitert werden können.

WO_3 -Inversopale mit unterschiedlichen photonischen Bandlücken wurden auch als optische Wasserstoffsensoren eingesetzt. Die optischen Responses von WO_3 -Inversopale mit verschiedenen H_2 -Konzentrationen wurden getestet. Aus der Response bei 1 vol% H_2 unter

unterschiedlichen Wellenlängen (Bandlücken) wurde die starke Brechungsindexdispersion von WO_3 nach Reaktion mit H_2 (nämlich H_xWO_3) rekonstruiert. Die Form dieser Dispersion kann durch das Drude-Modell angepasst werden, was darauf hindeutet, dass die freie Ladungsträgerabsorption der vorherrschende physikalische Ursprung der optischen Response ist. Die Dispersionskurve ist eine nützliche Richtlinie, um die Wellenlänge für die maximale Änderung des Brechungsindex zu finden, um damit die maximale gasinduzierte optische Response zu ermitteln.

Der Schlüsselparameter für die freie Ladungsträgerabsorption ist die freie Ladungsträgerdichte, die die Dispersion dieser Absorption und die Leitfähigkeit der halbleitenden Metalloxide bestimmt. Von den resistiven Sensoren ist bekannt, dass die Prüfgase die Leitfähigkeit von Metalloxiden effektiv verändern können, was auf eine starke, gasinduzierte Variation der freien Ladungsträgerdichte hinweist. Dementsprechend sollten die optischen Response für die meisten Metalloxide beobachtet werden, wenn sie auch den entsprechenden Testgasen ausgesetzt werden. Jedoch um messbare optische Response zu beobachten, sollte der zu messende Spektralbereich in der Nähe der stark dispersiven Region der optischen Konstanten von Metalloxiden liegen. Für die meisten Metalloxide liegt dieser Bereich während der Gasmessung im IR-Bereich. Dieser wiederum wird durch die Größe der Variation der Ladungsträgerdichte bestimmt. Für weitere Untersuchungen werden die anderen Metalloxid-Inversopale mit größeren photonischen Bandlücken hergestellt und eingesetzt, um die Wahl der Sensormaterialien für optische Gassensoren zu erweitern.

7. Reference

- [1] E. Yablonovitch, *Phys. Rev. Lett.* **1987**, 58, 2059.
- [2] S. John, *Phys. Rev. Lett.* **1987**, 58, 2486.
- [3] J.D. Joannopoulos, S.G. Johnson, J.N. Winn, R.D. Meade, *Photonic Crystals: Molding the Flow of Light, 2nd Edition*, Princeton University Press, Princeton, **2008**.
- [4] P. Yeh, A. Yariv, C. Hong, *J. Opt. Soc. Am.* **1977**, 67, 423.
- [5] P. Jiang, J. Bertone, K. Hwang, V. Colvin, *Chem. Mater.* **1999**, 11, 2132.
- [6] R. Fujikawa, A.V. Baryshev, K. Nishimura, H. Uchida, M. Inoue, *J. Porous Mater.* **2006**, 13, 287.
- [7] V. Baryshev, A. B. Khanikaev, R. Fujikawa, H. Uchida, M. Inoue, *Phys. Rev. B* **2007**, 76, 014305.
- [8] C. Aguirre, E. Reguera, A. Stein, *ACS Appl. Mater. Interfaces* **2010**, 2, 3257.
- [9] Lyon, Z. Meng, N. Singh, C. D. Sorrell, A. St. John, *Chem. Soc. Rev.* **2009**, 38, 865.
- [10] Y.H. Ye, F. LeBlanc, A. Haché, V.V. Truong, *Appl. Phys. Lett.* **2001**, 78, 52.
- [11] R.G. Shimmin, A. J. DiMauro, P.V. Braun, *Langmuir* **2006**, 22, 6507.
- [12] G. Collins, M. Blömker, M. Osiak, J.D. Holmes, M. Bredol, C. O'Dwyer, *Chem. Mater.* **2013**, 25, 4312.
- [13] J. Long, M. Fu, C. Li, C. Sun, D. He, Y. Wang, *Appl. Surf. Sci.* **2018**, 454, 112.
- [14] W. Hong, Y. Chen, X. Feng, Y. Yan, X. Hu, B. Zhao, F. Zhang, D. Zhang, Z. Xu, Y. Lai, *Chem. Comm.* **2013**, 49, 8229.
- [15] S. Kim, A.N. Mitropoulos, J.D. Spitzberg, H. Tao, D.L. Kaplan, F.G. Omenetto, *Nat. Photonics* **2012**, 6, 818.
- [16] Y. Zhang, J. Qiu, M. Gao, P. Li, L. Gao, L. Heng, B.Z. Tang, L. Jiang, *J. Mater. Chem. C* **2014**, 2, 8865.
- [17] X. Xu, A. V. Goponenko, S. A. Asher, *J. Am. Chem. Soc.* **2008**, 130, 3113.

- [18] J. Shin, P. V. Braun, W. Lee, *Sens. Actuators, B* **2010**, 150, 183.
- [19] Y. J. Lee, P. V. Braun, *Adv. Mater.* **2003**, 15, 563.
- [20] Y. Y. Diao, X. Y. Liu, G. W. Toh, L. Shi, J. Zi, *Adv. Funct. Mater.* **2013**, 23, 5373.
- [21] J. Wang, Y. Hu, R. Deng, R. Liang, W. Li, S. Liu, J. Zhu, *Langmuir* **2013**, 29, 8825.
- [22] R.J.W. Scott, S.M. Yang, G. Chabanis, N. Coombs, D.E. Williams, G.A. Ozin, *Adv. Mater.* **2001**, 13, 1468.
- [23] M. D'Arienzo, L. Armelao, A. Cacciamani, C.M. Mari, S. Polizzi, R. Ruffo, R. Scotti, A. Testino, L. Wahba, F. Morazzoni, *Chem. Mater.* **2010**, 22, 4083.
- [24] X. You, J.H. Pikul, W.P. King, J.J. Pak, *Appl. Phys. Lett.* **2013**, 102, 253103.
- [25] T.G. Euser, H. Wei, J. Kalkman, Y. Jun, A. Polman, D. J. Norris, W.L. Vos, *J. Appl. Phys.* **2007**, 102, 053111.
- [26] L. Zhang, E. Reisner, J.J. Baumberg, *Energy Environ. Sci.* **2014**, 7, 1402.
- [27] Z. Li, T. Zhao, X. Zhan, D. Gao, Q. Xiao, G. Lei, *Electrochim. Acta* **2010**, 55, 4594.
- [28] L.J. Diguna, Q. Shen, J. Kobayashi, T. Toyoda, *Appl. Phys. Lett.* **2007**, 91, 023116.
- [29] W. Stöber, A. Fink, *J. Colloid interface Sci.* **1968**, 26, 62.
- [30] B.T. Holland, C.F. Blanford, T. Do, A. Stein, *Chem. Mater.* **1999**, 11, 795.
- [31] C.E. Reese, C.D. Guerrero, J.M. Weissman, K. Lee, S.A. Asher, *J. Colloid Interface Sci.* **2000**, 232, 76.
- [32] A.D. Dinsmore, J.C. Crocker, A.G. Yodh, *Curr. Opin. Colloid In.* **1998**, 3, 5.
- [33] M. Egen, R. Zentel, *Macromol. Chem. Phys.* **2004**, 205, 1479.
- [34] I. Piirma, *Emulsion Polymerization*, Academic Press, New York, **1982**.
- [35] T.P. Chiu, T.M. Don, *J. Appl. Polym. Sci.* **2008**, 109, 3622.
- [36] T. Tanrisever, O. Okay, I.Ç. Sönmezoğlu, *J. Appl. Polym. Sci.* **1996**, 61, 485.
- [37] J.R. Fried, *Polymer Science and Technology*, American Chemical Society, **2003**.

- [38] Y.A. Vlasov, V.N. Astratov, A.V. Baryshev, A.A. Kaplyanskii, O.Z. Karimov, M.F. Limonov, *Phys. Rev. E* **2000**, 61, 5784.
- [39] K.E. Davis, W.B. Russel, W.J. Glantschnig, *J. Chem. Soc., Faraday Trans.* **1991**, 87, 411.
- [40] A.V. Baryshev, A.B. Khanikaev, R. Fujikawa, H. Uchida, M. Inoue, *Phys. Rev. B* **2007**, 76, 014305.
- [41] R. Fujikawa, A.V. Baryshev, K. Nishimura, H. Uchida, M. Inoue, *J. Porous Mater.* **2006**, 13, 287.
- [42] B. Hatton, L. Mishchenko, S. Davis, K.H. Sandhage, J. Aizenberg, *Proc. Natl. Acad. Sci. U. S. A.* **2010**, 107, 10354.
- [43] P. Jiang, T. Prasad, M.J. McFarland, V.L. Colvin, *App. Phys. Lett.* **2006**, 89, 011908.
- [44] P. Jiang, M.J. McFarland, *J. Am. Chem. Soc.* **2004**, 126, 13778.
- [45] M. Pichumani, P. Bagheri, K.M. Poduska, W. Gonzalez-Vinas, A. Yethiraj, *Soft Matter* **2013**, 9, 3220.
- [46] M. Ghosh, F.Q. Fan, K.J. Stebe, *Langmuir* **2007**, 23, 2180.
- [47] Y.N. Fu, Z.G. Jin, Z.F. Liu, Y. Liu, W. Li, *Mater. Lett.* **2008**, 62, 4286.
- [48] Y. Wang, L. Chen, H. Yang, Q. Guo, W. Zhou, M. Tao, *Mater. Sci.-Pol.* **2010**, 28, 467.
- [49] Z.Z. Gu, A. Fijishima, O. Sato, *Chem. Mater.* **2002**, 14, 760.
- [50] C. Deleuze, B. Sarrat, F. Ehrenfeld, S. Perquis, C. Derail, L. Billon, *Phys. Chem. Chem. Phys.* **2011**, 13, 10681.
- [51] S. H. Im, O. O. Park, *Langmuir* **2002**, 18, 9642.
- [52] Q. Yan, Z. Zhou, X. Zhao, *Langmuir* **2005**, 21, 3158.
- [53] Y. Fu, Z. Jin, G. Liu, Y. Yin, *Synth. Met.* **2009**, 159, 1744.
- [54] Y. Li, Q. Yang, M. Li, Y. Song, *Sci. Rep.* **2016**, 6, 24628.
- [55] N. Vogel, M. Retsch, C.A. Fustin, A. del Campo, U. Jonas, *Chem. Rev.* **2015**, 115, 6265.

- [56] O.D. Velev, T.A. Jede, R.F. Lobo, A.M. Lenhoff, *Nature* **1997**, 389, 447.
- [57] O.D. Velev, T.A. Jede, R.F. Lobo, A.M. Lenhoff, *Chem. Mater.* **1998**, 10, 3597.
- [58] B.T. Holland, C.F. Blanford, A. Stein, *Science* **1998**, 281, 538.
- [59] B.T. Holland, L. Abrams, A. Stein, *J. Am. Chem. Soc.* **1999**, 121, 4308.
- [60] J.E.G.J. Wijnhoven, W.L. Vos, *Science* **1998**, 281, 802.
- [61] H. Yan, C.F. Blanford, B.T. Holland, W.H. Smyrl, A. Stein, *Chem. Mater.* **2000**, 12, 1134.
- [62] H. Yan, C. F. Blanford, J.C. Lytle, C.B. Carter, W.H. Smyrl, A. Stein, *Chem. Mater.* **2001**, 13, 4314.
- [63] M. Sadakane, K. Sasaki, H. Nakamura, T. Yamamoto, W. Ninomiya, W. Ueda, *Langmuir* **2012**, 28, 17766.
- [64] M. Sadakane, T. Horiuchi, N. Kato, C. Takahashi, W. Ueda, *Chem. Mater.* **2007**, 19, 5779.
- [65] S. Kuai, S. Badilescu, G. Bader, R. Bruning, X. Hu, V.V. Truong, V. V. *Adv. Mater.* **2003**, 15, 73.
- [66] M.C. Carbajo, C. Lopez, A. Gomez, E. Enciso, M.J. Torralvo, *J. Mater. Chem.* **2003**, 13, 2311.
- [67] R.W.J. Scott, S.M. Yang, G. Chabanis, N. Coombs, D.E. Williams, G.A. Ozin, *Adv. Mater.* **2001**, 13, 1468.
- [68] R.W.J. Scott, S.M. Yang, D.E. Williams, G.A. Ozin, *Chem. Comm.* **2003**, 688.
- [69] J. He, D.M. Weekes, W. Cheng, K.E. Dettelbach, A. Huang, T. Li, C.P. Berlinguette, *J. Am. Chem. Soc.* **2017**, 139, 18174.
- [70] G. Subramanian, V.N. Manoharan, J.D. Thorne, D.J. Pine, *Adv. Mater.* **1999**, 11, 1261.
- [71] E.S. Kwak, W. Lee, N.G. Park, J. Kim, H. Lee, *Adv. Funct. Mater.* **2009**, 19, 1093.
- [72] H. Míguez, C. López, F. Meseguer, A. Blanco, L. Vázquez, R. Mayoral, *Appl. Phys. Lett.* **1997**, 71, 1148.

- [73] A. Reynolds, F. López-Tejeira, D. Cassagne, F. J. García-Vidal, C. Jouanin, J. Sánchez-Dehesa, *Phys. Rev. B* **1999**, 60, 11422.
- [74] E.W. Washburn, *International Critical Tables*, New York, **1928**.
- [75] G. M. Hale, M. R. Querry, *Appl. Opt.* **1973**, 12, 555.
- [76] S. Kedenburg, M. Vieweg, T. Gissibl, H. Giessen, *Opt. Mater. Express* **2012**, 2, 1588.
- [77] Z. Rappoport, *CRC Handbook of Tables for Organic Compound Identification*, CRC Press, Boca Raton, **1967**.
- [78] C.S. Kim, R.J. Lad, C.P. Tripp, *Sens. Actuators B* **2001**, 76, 442.
- [79] D. Kuckling, K. Moosmann, J.E.S. Schier, A. Britze, *Colloid Polym. Sci.* **2013**, 291, 1429.
- [80] M. Fox, *Optical Properties of Solids*, 2. Ed, Oxford University Press, New York, **2010**.
- [81] M. Ando, T. Kobayashi, M. Haruta, *Catal. Today*. **1997**, 36, 135.
- [82] M.I. Baraton, L. Merhari, *Synth. React. Inorg., Met.-Org., Nano-Met. Chem.* **2005**, 35, 733.
- [83] K. Ito, T. Ohgami, *Appl. Phys. Lett.* **1992**, 60, 938.
- [84] A. Georg, W. Graf, R. Neumann, V. Wittwer, *Solid State Ionics* **2000**, 127, 319.
- [85] D. Nau, A. Seidel, R.B. Orzekowsky, S.H. Lee, S. Deb, H. Giessen, *Opt. Lett.* **2010**, 35, 3150.
- [86] Z. Xie, H. Xu, F. Rong, L. Sun, S. Zhang, Z. Gu, *Thin Solid Films* **2012**, 520, 4063.
- [87] P.J. Shaver, *Appl. Phys. Lett.* **1967**, 11, 255.
- [88] H. Chen, N. Xu, S. Deng, D. Lu, Z. Li, J. Zhou, J. Chen, *Nanotechnology* **2007**, 18, 205701.
- [89] S.H. Lee, H.M. Cheong, P. Liu, D. Smith, C.E. Tracy, A. Mascarenhas, J.R. Pitts, S.K. Deb, *J. Appl. Phys.* **2000**, 88, 3076.
- [90] S. Okazaki, H. Nakagawa, S. Asakura, Y. Tomiuchi, N. Tsuji, H. Murayama, M. Washiya, *Sens. Actuators, B* **2003**, 93, 142.

- [91] S.K. Deb, *Sol. Energy Mater. Sol. Cells* **2008**, 92, 245.
- [92] C.G. Granqvist, *Handbook of Inorganic Electrochromic Materials*, Elsevier, Amsterdam, **1995**.
- [93] T. Xian, H. Yang, L. Di, X. Chen, J. Dai, *J. Sol-Gel Sci. Technol.* **2013**, 66, 324.
- [94] B. Cheng, P. Ni, C. Jin, Z. Li, D. Zhang, P. Dong, X. Guo, *Opt. Commun.* **1999**, 170, 41.
- [95] J.M. Hughes, P.M. Budd, A. Grieve, P. Dutta, K. Tiede, J. Lewis, *J. Appl. Polym. Sci.*, **2015**, 1, 42061.
- [96] Z. Song, E.S. Daniels, E.D. Sudol, A. Klein, M.S. El-Aasser, *Colloid. Polym. Sci.* **2014**, 292, 645.
- [97] M. Egen, *Funktionale dreidimensionale Photonische Kristalle aus Polymerlatizes*, Mainz **2003**.
- [98] Q. Ye, Z. Zhang, X. Ge, Y. Ni, M. Wang, *Colloid. Polym. Sci.* **2002**, 280, 1091.
- [99] S.M. Pourmortazavi, S.G. Hosseini, M.Rahimi-Nasrabadi, S.S. Hajimirsadeghi, H. Momenian, *J. Hazard. Mater.* **2009**, 162, 1141.
- [100] S. Amrehn, D. Berghoff, A. Nikitin, M. Reichelt, X. Wu, T. Meier, T. Wagner, *Photonics Nanostructures: Fundam. Appl.* **2016**, 19, 55.
- [101] Z.X. Lin, *Analysis and Identification of Infrared Spectrum of the Polymer*, Sichuan University Press, Chengdu, **1989**.
- [102] C. Weinberger, J. Roggenbuck, J. Hanss, M. Tiemann, *Nanomaterials* **2015**, 5, 1431.
- [103] A. Małecki, B. Małecka, R. Gajerski, S. Łabuś, *J. Therm. Anal. Calorim.* **2003**, 72, 135.
- [104] V. Berbenni, C. Milanese, G. Bruni, A. Marini, *J. Therm. Anal. Calorim.* **2005**, 82, 401.
- [105] K. Wiczorek-Ciurowa, A.J. Kozak, *J. Therm. Anal. Calorim.* **1999**, 58, 647.
- [106] M.C. Nguyen, M. Jang, D.H. Lee, H.J. Bang, M. Lee, J.K. Jeong, H. Yang, R. Choi, *Sci. Rep.* **2016**, 6, 25079.

- [107] M. Sadakane, T. Horiuchi, N. Kato, C. Takahashi, W. Ueda, *Chem. Mater.* **2007**, 19, 5779.
- [108] L. Xia, L. Xu, J. Song, R. Xu, D. Liu, B. Dong, H. Song, *Sci. Rep.* **2015**, 5, 10838.
- [109] Q.Z. Wu, Y. Shen, J.F. Liao, Y.G. Li, *Mater. Lett.* **2004**, 58, 2688.
- [110] M. Sadakane, R. Kato, T. Murayama, W. Ueda, *J. Solid State Chem.* **2011**, 184, 2299.
- [111] I. R. Wilding, C. D. Melia, R. D. Short, M. C. Davies, A. Brown, *J. Appl. Polym. Sci.* **1990**, 39, 1287.
- [112] J. S. Brinen, S. Greenhouse, L. Pinatti, *Surf. Interface Anal.* **1991**, 17, 63.
- [113] R.M. Mohamed, E.S. Baeissa, I.A. Mkhaliid, M.A. Al-Rayyani, *Appl. Nanosci.* **2013**, 3, 57.
- [114] T. Xian, H. Yang, L.J. Di, X.F. Chen, J.F. Dai, *J. Sol-Gel Sci. Technol.* **2013**, 66, 324.
- [115] X. Wang, R. Wang, C. Peng, T. Li, B. Liu, *J. Sol-Gel Sci. Technol.* **2011**, 57, 115.
- [116] Y. Kitahara, K. Okuyama, K. Ozawa, T. Suga, S. Takahashi, T. Fujii, *J. Therm. Anal. Calorim.* **2012**, 110, 423.
- [117] D.R. Lide, *CRC Handbook of Chemistry and Physics*, CRC Press, Boca Raton, **2005**.
- [118] J.W. Galusha, C.K. Tsung, G.D. Stucky, M.H. Bartl, *Chem. Mater.* **2008**, 20, 4925.
- [119] R.C. Schroden, M. Al-Daous, C.F. Blanford, A. Stein, *Chem. Mater.* **2002**, 14, 3305.
- [120] S. Amrehn, X. Wu, T. Wagner, *ACS Sens.* **2018**, 3, 191.
- [121] C. Weinberger, S. Vetter, M. Tiemann, T. Wagner, *Microporous Mesoporous Mater.* **2016**, 223, 53.
- [122] P.G. Wilkinson, *J. Appl. Phys.* **1951**, 22, 226.
- [123] S. Amrehn, X. Wu, C. Schumacher, T. Wagner, *Phys. Status Solidi A* **2015**, 212, 1266.
- [124] A. Di Falco, L. O'Faolain, T.F. Krauss, *Appl. Phys. Lett.* **2009**, 94, 063503.
- [125] N. Cennamo, D. Massarotti, L. Conte, L. Zeni, *Sensors* **2011**, 11, 11752.

- [126] R. B. Goldner, P. Norton, K. Wong, G. Foley, E. L. Goldner, G. Seward, R. Chapman, *Appl. Phys. Lett.* **1985**, 47, 536.
- [127] J. Wu, D. Day, M. Gu, *Appl. Phys. Lett.* **2008**, 92, 071108.
- [128] B. Wang, M.A. DüNDAR, R. Nötzel, F. Karouta, S. He, R.W. van der Heijden, *Appl. Phys. Lett.* **2010**, 97, 151105.
- [129] W.K. Kuo, H.P. Weng, J.J. Hsu, H.H. Yu, *Appl. Sci.* **2016**, 6, 67.
- [130] Y. Villachon-Renard, G. Leveque, A. Abdellaoui, A. Donnadieu, *Thin Solid Films* **1991**, 203, 33.
- [131] C.G. Granqvist, *Handbook of Inorganic Electrochromic Materials*, Elsevier, Amsterdam, **1995**.
- [132] Y. Yamada, K. Tajima, S. Bao, M. Okada, K. Yoshimura, A. Roos, *J. Appl. Phys.* **2008**, 103, 063508.
- [133] A. Nakamura, S. Yamada, *Appl. Phys.* **1981**, 24, 55.

8. Appendix

List of Abbreviations

1D	one-dimensional
2D	two-dimensional
3D	three-dimensional
d	interplanar spacing
D	particle diameter
DLS	dynamic light scattering
DSC	differential scanning calorimetry
DTG	derivative thermogravimetry
e	electronic charge
EGDMA	ethylene glycol dimethacrylate
f	volume fraction
fcc	face-centered cubic
FTIR	fourier-transform infrared spectroscopy
FWHM	full widths at half maximum
IR	infrared
JCPDS	Joint Committee on Powder Diffraction Standards
k	extinction coefficient
m	effective conduction-band mass
MMA	methyl-methacrylate
MS	mass spectrometry
n_{eff}	effective refractive index
N_{free}	free electron density
NIR	near-infrared
P(DEVBP-b-NIPAAm)	poly(diethyl-4-vinyl-benzyl phosphonate-b-N-isopropylacrylamide)
PDI	polydispersity index
PMMA	poly methyl-methacrylate
PS	polystyrene
P-XRD	powder X-ray diffraction
R	optical response
RIU	refractive index unit

S	sensitivity
SEM	scanning electron micrographs
SFEP	surfactant-free emulsion polymerization
T_c	critical solution temperature
T_g	glass transition temperature
TGA	thermogravimetric analysis
TEOS	tetraethyl orthosilicate
UV-VIS	ultraviolet–visible
λ	reflection peak position
α	absorption coefficient
γ	damping coefficient
ϵ	relative permittivity
σ	standard deviation
ω_p	plasma frequency

List of Tables

Table 3.1: Reaction conditions for variation of PMMA particle size	17
Table 3.2: Inverse opal synthesis conditions with pure metal nitrates as precursors.....	19
Table 3.3: Concentration of citric acid and metal nitrate for preparation of the modified metal nitrate precursors	19
Table 4.1: Effect of MMA concentration on the diameters and polydispersity of PMMA spheres.....	25
Table 4.2: Summary of the band gap position of PMMA opals and the diameters of corresponding PMMA particles	29
Table 4.3: Onset temperature of nitrate conversion and PMMA decomposition in the composite material	45
Table 4.4: Summary of the structural parameters of WO ₃ inverse opal with different periodicities	56
Table 4.5: Summary of the pore sizes of resulting WO ₃ inverse opals and the corresponding band gap position	57
Table 4.6: Summary of sensitivities of WO ₃ inverse opal (WO ₃ -277, band gap at 520 nm) after introducing different fluids	60
Table 4.7: Summary of sensitivities of different WO ₃ inverse opals.....	61
Table 4.8: Summary of the optical response of WO ₃ -277 (Band gap: 525 nm) and WO ₃ -355 (Band gap: 601 nm) at different H ₂ concentration	67
Table 4.9: Summary of gas response of WO ₃ inverse opals with different periodicities	70
Table 4.10: Summary of refractive indices of H _x WO ₃ when exposed to 1 vol% H ₂ with different periodicities	71
Table 5.1: Photograph of the as-synthesized metal oxide inverse opals.....	76
Tabelle 6.1: Fotografie der hergestellten Metalloxid-Inversopale	79

List of Figures

Figure 2.1: Schema of one-dimensional (1D), two-dimensional (2D) and three-dimensional (3D) photonic crystals. The black and white colors represent materials with different refractive indices. Modified from reference [3]	3
Figure 2.2: iridescent blue color of a butterfly (left, image from animalshine.com) and strong opalescence of a gem stone opal (right, image from minerals.net).....	4
Figure 2.3: The diffraction of light from closed-packed {111} crystal planes in a colloidal photonic crystal	5
Figure 2.4: SEM images of a PMMA opal structure (left) and a ZnO inverse opal structure (right).....	6
Figure 2.5: Reaction mechanisms of surfactant free emulsion polymerization	8
Figure 2.6: Schematic view of the crystallization process by drop-casting	9
Figure 2.7: Schematic procedure used to fabricate metal oxide inverse opals.....	9
Figure 2.8: Solidification of precursors in low ordered template matrix (a) and in disordered template matrix (b).....	10
Figure 2.9: Schematic procedure of fabricating metal oxide inverse opals by nanoparticles infiltration (black points indicate metal oxide nanoparticles)	11
Figure 2.10: Temperature responsive block copolymer (blue) adsorbed on the inner surfaces of inverse opal pores	12
Figure 2.11: Sensing mechanism of WO_3/H_2 system.....	14
Figure 2.12: Relationship between refractive index n and extinction coefficient k of WO_3 after exposed to H_2 (Estimated based on Drude model).....	16
Figure 3.1: Photograph of the mobile gas sensing setup.....	23
Figure 4.1 The relationship between the MMA concentration and the diameters of PMMA particles (from DLS)	26
Figure 4.2: SEM images of PMMA opals with different pore sizes: (a) 298 nm, (b) 425 nm, (c) 502 nm, (d) 572 nm and (e) 644 nm; The diameters were obtained by measuring 100 particles in each sample	28
Figure 4.3: FTIR spectra of PMMA opals with different sizes of template particles	28
Figure 4.4: Relationship between the band gap position of PMMA opals and the diameters of corresponding PMMA particles	29
Figure 4.5: Contact angle Θ of a drop of PMMA dispersion on a glass substrate (left), and on a nitrocellulose substrate (right).....	30

Figure 4.6: Photo of a nitrocellulose substrate (left) and a PMMA opal deposited on the nitrocellulose substrate (right, PMMA size: 315 nm)	30
Figure 4.7: Microscope pictures of PMMA opal deposited on a glass substrate (left) and on a nitrocellulose substrate (right).....	31
Figure 4.8: FTIR spectra of PMMA opal deposited on different substrates	31
Figure 4.9: Microscope pictures of Ga ₂ O ₃ inverse opal: precursor prepared with 30 wt% gallium nitrate (a), 40 wt% gallium nitrate (b) and 50 wt% gallium nitrate (c).....	32
Figure 4.10: FTIR spectra of Ga ₂ O ₃ inverse opal: precursor prepared with different gallium nitrate concentration	33
Figure 4.11: Microscope pictures of Ga ₂ O ₃ inverse opal: after infiltration sample dried at room temperature (a), 40 °C (b), 60 °C (c) and 80 °C (d).....	34
Figure 4.12: FTIR spectra of Ga ₂ O ₃ inverse opal: precursor prepared with different drying temperature	34
Figure 4.13: Microscope pictures of Ga ₂ O ₃ inverse opal: calcined at 350 °C (left), 450 °C (middle) and 550 °C (right).....	35
Figure 4.14: FTIR spectra of Ga ₂ O ₃ inverse opal: calcined at different temperature	35
Figure 4.15: SEM image (left) and FTIR spectrum (right) of Ga ₂ O ₃ inverse opal. Insets: photograph of corresponding Ga ₂ O ₃ inverse opal.....	36
Figure 4.16: SEM image (left) and FTIR spectrum (right) of Cr ₂ O ₃ inverse opal. Insets: photograph of corresponding Cr ₂ O ₃ inverse opal	37
Figure 4.17: SEM image (left) and FTIR spectrum (right) of Fe ₂ O ₃ inverse opal. Insets: photograph of corresponding Fe ₂ O ₃ inverse opal	37
Figure 4.18: SEM image (left) and FTIR spectrum (right) of In ₂ O ₃ inverse opal. Insets: photograph of corresponding In ₂ O ₃ inverse opal	38
Figure 4.19: SEM images of CeO ₂ (left), CuO (middle), and ZnO (right) films which are prepared with repective metal nitrate precursors	39
Figure 4.20: Differential scanning calorimetry (DSC) results of PMMA spheres (left) and pure metal nitrate salts (right)	40
Figure 4.21: Thermogravimetric/derivative thermogravimetry (TG/DTG, top) and mass spectrometry (MS, bottom) results of PMMA templates	40
Figure 4.22: Transmittance spectrum of synthesized PMMA particles	41
Figure 4.23: Thermogravimetric/derivative thermogravimetry (TG/DTG) and mass spectrometry (MS) results of PMMA-Cr(NO ₃) ₃ ·9H ₂ O-composite (left) and PMMA-Fe(NO ₃) ₃ ·6H ₂ O-composite (right)	42

Figure 4.24: Thermogravimetric/derivative thermogravimetry (TG/DTG) and mass spectrometry (MS) results of PMMA-Ga(NO ₃) ₃ ·xH ₂ O-composite (left) and PMMA-In(NO ₃) ₃ ·xH ₂ O-composite (right)	43
Figure 4.25: Thermogravimetric/derivative thermogravimetry (TG/DTG) and mass spectrometry (MS) results of PMMA-Ce(NO ₃) ₂ ·6H ₂ O-composite (left), PMMA-Cu(NO ₃) ₂ ·2.5H ₂ O-composite (right).....	43
Figure 4.26: Thermogravimetric/derivative thermogravimetry (TG/DTG) and mass spectrometry (MS) results of PMMA-Zn(NO ₃) ₂ ·6H ₂ O-composite.....	44
Figure 4.27: Reaction of metal cation with citric acid	46
Figure 4.28: SEM image (left) and FTIR spectrum (right) of CeO ₂ inverse opal. Insets: photograph of corresponding CeO ₂ inverse opal	47
Figure 4.29: SEM image (left) and FTIR spectrum (right) of CuO inverse opal. Insets: photograph of corresponding CuO inverse opal	48
Figure 4.30: SEM image (left) and FTIR spectrum (right) of ZnO film.....	48
Figure 4.31: Thermogravimetric/derivative thermogravimetry (TG / DTG) and mass spectrometry (MS) results of PMMA-cerium citrate-composite (left), PMMA-cooper citrate-composite (middle) and PMMA-zinc citrate-composite (right).....	49
Figure 4.32: Schema of the ZnO-SiO ₂ intramolecular network.....	50
Figure 4.33: SEM image (left) and FTIR spectrum (right) of ZnO-SiO ₂ inverse opal. Insets: photograph of corresponding ZnO-SiO ₂ inverse opal.....	50
Figure 4.34: Shema of infiltrated PMMA opal after polyacrylamide gelation	51
Figure 4.35: SEM image (left) and FTIR spectrum (right) of ZnO-Acrylamide inverse opal. Insets: photograph of corresponding ZnO-Arcylamide inverse opal	51
Figure 4.36: SEM image (left) and FTIR spectrum (right) of SnO ₂ inverse opal. Insets: photograph of corresponding SnO ₂ inverse opal.....	53
Figure 4.37: SEM image (left) and FTIR spectrum (right) of TiO ₂ inverse opal. Insets: photograph of corresponding TiO ₂ inverse opal	54
Figure 4.38: SEM images of WO ₃ opals with different pore sizes: (a) 277 nm, (b) 355 nm, (c) 452 nm, (d) 553 nm, (e) 583 nm and (f) 619 nm.....	55
Figure 4.39: FTIR spectra of WO ₃ inverse opals with different pore sizes	56
Figure 4.40: Relationship between the band gap position and corresponding pore sizes of WO ₃ inverse opal	57
Figure 4.41: X-Ray diffraction patterns of the WO ₃ inverse opal (black) and standard diffraction pattern (magenta) of orthorhombic WO ₃ (JCPDS No. 71-0131).....	58

Figure 4.42: FTIR spectra of WO ₃ inverse opal (WO ₃ -277, band gap at 520 nm) before and after introducing different fluids	59
Figure 4.43: FTIR spectra of WO ₃ inverse opals (left: WO ₃ -355, right: WO ₃ -452) before and after introducing acetone	60
Figure 4.44: FTIR spectra of WO ₃ inverse opals (left: WO ₃ -553, right: WO ₃ -583) before and after introducing acetone	61
Figure 4.45: Relationship between the pore size of WO ₃ inverse opals and the optical sensitivity	62
Figure 4.46: Microscope pictures of WO ₃ inverse opal before adsorption (left), after adsorption (middle) and after washing with 20 °C water (right)	63
Figure 4.47: FTIR spectra of WO ₃ inverse opal before adsorption, after adsorption and after washing with 20 °C water	63
Figure 4.48: Microscope pictures of WO ₃ inverse opal before adsorption (left), after adsorption (middle) and after washing with 40 °C water (right)	64
Figure 4.49: FTIR spectra of WO ₃ inverse opal before adsorption, after adsorption and after washing with 40 °C water	64
Figure 4.50: Microscope pictures of WO ₃ inverse opal before adsorption (top left), after adsorption (top right), after washing with 60 °C (below left) and 20 °C water (below right) successively	65
Figure 4.51: FTIR spectra of WO ₃ inverse opal before adsorption, after adsorption, and after washing with 60 °C and 20 °C water successively	65
Figure 4.52: Reflection peak position shift of WO ₃ inverse opals (left: WO ₃ -277, right: WO ₃ -355) during H ₂ sensing measurement in open system at 200 °C (blue region: H ₂ exposure; white region: flushed by pure N ₂)	66
Figure 4.53: Compare the optical response of WO ₃ -277 and WO ₃ -355 at different H ₂ concentration	68
Figure 4.54. Reflection peak position shifts of WO ₃ inverse opals (left: WO ₃ -277, right: WO ₃ -355) during H ₂ sensing measurement at 140 °C. (blue region: H ₂ exposure; grey region: regeneration by synthetic air; white region: flushed by pure N ₂)	68
Figure 4.55. Reflection peak position shifts of WO ₃ inverse opals (left: WO ₃ -452, right: WO ₃ -553) during H ₂ sensing measurement at 140 °C. (blue region: H ₂ exposure; grey region: regeneration by synthetic air; white region: flushed by pure N ₂)	69

Figure 4.56. Reflection peak position shifts of WO_3 inverse opals (left: WO_3 -583, right: WO_3 -619) during H_2 sensing measurement at 140 °C. (blue region: H_2 exposure; grey region: regeneration by synthetic air; white region: flushed by pure N_2) 69

Figure 4.57: Relationship between the peak position when exposed to 1 vol% H_2 and peak shift (left) / optical response (right) of WO_3 inverse opals when exposed to 1 vol% H_2 70

Figure 4.58: Estimated dispersion of the refractive index of H_xWO_3 72

Figure 4.59: Estimated dispersion of the real part of the refractive index of H_xWO_3 (black scatters) and the fitting curve (blue line) based on Drude model..... 74

List of Publications

Peer-reviewed Papers

- **Refractive Index Modulation in Metal Oxides Arising from Chemically Induced Free Carriers and Its Application in Gas Sensing**
X. Zhang, X. Wu, S. Amrehn, T. Wagner
J. Mater. Chem. C, 2019, 7, 6752
- **Synthesis of High Quality Metal Oxide Inverse Opals: Metal Nitrate-based Precursors for Colloidal Crystal Templating**
X. Zhang, S. Amrehn, X. Wu, M. Tiemann, T. Wagner
Eur. J. Inorg. Chem. under review

Conference Proceedings

- **Gas Sensor Based on Metal Oxide Photonic Crystals: The Role of Free Carrier Absorption**
D. Rengel, X. Wu, L. Kothe, X. Zhang, S. Amrehn, T. Wagner
SPIE Nanoscience + Engineering, 2019, San Diego, California, United States
- **Lichtabsorption durch freie Ladungsträger in Metalloxiden: Anwendung der Brechungsindex-Modulation in der Gassensorik**
X. Wu, X. Zhang, S. Amrehn, T. Wagner
20. GMA/ITG-Fachtagung Sensoren und Messsystem, 2019, Nürnberg, Germany
- **Optische Wasserstoffdetektion mit WO₃ Inversopalen als neuartige Gas-Transducer**
S. Amrehn, D. Klawinski, S. Vetter, X. Zhang, X. Wu, T. Wagner
12. Dresdner Sensor-Symposium, 2015, Dresden, Germany
- **Artificial Inverse Opal Structures for Sensing Applications**
X. Wu, S. Amrehn, X. Zhang, C. Schumacher, T. Wagner
AMA Conferences Sensor and IRS², 2015, Nürnberg, Germany

Oral Presentations

- **Precursor Design Rules for Metal Oxide Inverse Opals**
X. Zhang, S. Amrehn, X. Wu, T. Wagner
31. Deutsche Zeolith-Tagung, 2019, Dresden, Germany
- **Optical Impact of Precursor Modifications on Metal Oxide Inverse Opals**
X. Zhang, S. Amrehn, X. Wu, T. Wagner
Materials Science and Engineering, 2018, Darmstadt, Germany

Poster Presentations

- **Gas Sensor Based on Metal Oxide Photonic Crystals: The Role of Free Carrier Absorption**
X. Wu, X. Zhang, S. Amrehn, D. Rengel, L. Kothe, T. Wagner
SPIE Nanoscience + Engineering, 2019, San Diego, California, United States
- **Optical Gas Sensing Based on Free Carrier Absorption in Metal Oxides**
X. Wu, X. Zhang, S. Amrehn, B. Schwind, T. Wagner
Conference on Lasers and Electro-Optics, 2019, München, Germany
- **Functional Nanoparticles for Responsive Photonic Crystals**
X. Zhang, D. Rengel, X. Wu, T. Wagner
Particle-Based Materials Symposium, 2017, Saarbrücken, Germany
- **Core-Shell Particles for Opal Synthesis**
X. Zhang, S. Amrehn, X. Wu, M. Tiemann, T. Wagner
28. Deutsche Zeolith-Tagung, 2016, Gießen, Germany
- **Optische Wasserstoffdetektion mit WO₃ Inversopalen als neuartige Gas-Transducer**
S. Amrehn, D. Klawinski, S. Vetter, X. Zhang, X. Wu, T. Wagner
12. Dresdner Sensor-Symposium, 2015, Dresden, Germany

Danksagung

Zum Schluss möchte ich mich bei allen Menschen bedanken, die mich während meiner gesamten Studienzeit in Deutschland so freundlich unterstützt haben.

Mein Dank gilt insbesondere Dr. Thorsten Wagner für die Möglichkeit, meine Doktorarbeit in seiner Nachwuchsgruppe durchführen zu können. Ich möchte mich bei dir für die vielfältige Unterstützung, die wertvollen Diskussionen und Ideen bedanken.

Bei Prof. Dr. Michael Tiemann möchte ich mich für die Übernahme des Zweitgutachtens bedanken.

Mein Dank gilt auch Prof. Dr. Sabine Fechner und Prof. Dr. Klaus Huber für die Unterstützung in der Prüfungskommission.

Herrn Dr. Xia Wu danke ich besonders für die hervorragende Betreuung und seine ständige Diskussions- und Hilfsbereitschaft.

Frau Dr. Sabrina Amrehn und Herrn Dr. Christian Weinberger möchte ich mich herzlich bedanken für die sorgfältige Korrektur dieser Arbeit.

Für die Hilfe bei der Charakterisierung der vorgestellten Materialien danke ich:

- REM-Analyse: Nadine Buitkamp
- TGA-Analyse: Manuel Traut
- XRD-Analyse: Andrej Paul
- DSC-Analyse: Susanna Keuker-Baumann

Vielen Dank an die gesamten Arbeitsgruppen Wagner und Tiemann für die freundschaftliche Arbeitsatmosphäre und alle Hilfe im Labor. Des Weiteren bedanke ich mich bei den Freunden und Kollegen, die mich während meiner Zeit in Paderborn begleitet haben und diese unvergesslich machen. Ich möchte mich darüber hinaus bei meiner Eltern bedanken. Sie haben stets größtes Vertrauen in mich gehabt und mich während der gesamten Studienzeit unterstützt.